

Development and Application of a Hypersonic Flow Solver

Louis Walpot



3861

220-704

220-704

TR 3861

Development and Application of a Hypersonic Flow Solver

Proefschrift

ter verkrijging van de graad van doctor
aan de Technische Universiteit Delft,
op gezag van de Rector Magnificus Prof. dr. ir. J.T. Fokkema,
voorzitter van het College voor Promoties,
in het openbaar te verdedigen
op maandag 6 mei 2002 om 13:30 uur

door

Lowie Marcel Gerard Frans Maria WALPOT

ingenieur luchtvaart en ruimtevaart
geboren te Tongeren, België



Dit proefschrift is goedgekeurd door de promotor:
Prof. dr. ir. P.G. Bakker

Samenstelling promotiecommissie:

Rector Magnificus,	voorzitter
Prof. dr. ir. P.G. Bakker,	Technische Universiteit Delft, promotor
Prof. M. Ivanov,	Novosibirsk State Technical University
Prof. dr-ing. H. Olivier,	University Aachen
Prof. dr. ir. D. Roekaerts,	Technische Universiteit Delft
Prof. D. Zeitoun,	Université de Provence
Dr. ir. M.I. Gerritsma,	Technische Universiteit Delft
Ir. J. Muylaert,	ESA/ESTEC, Noordwijk

Dr. ir. M.I. Gerritsma heeft als begeleider in belangrijke mate aan de totstandkoming van het proefschrift bijgedragen.

Copyright ©2002 by L. Walpot, Delft, The Netherlands

All rights reserved. No part of this material protected by this copyright notice may be reproduced, or utilized in any form or by any means, electronic or mechanical, including photocopying, recording or by any information storage and retrieval system, without prior written permission by the author.

Druk: Duineveld Drukkerij Lisse, tel. 0252-213302, e-mail info@duineveld.nl

ISBN 90-9015821-9

Contents

1	Introduction	1
1.1	Historical perspective of hypersonic research	1
1.2	Relevant physics of hypersonic flows	4
1.3	Numerical techniques	5
1.4	Objective and scope of present work	6
2	Governing equations for high temperature gas flows	9
2.1	The flow equations in conservative form	9
2.2	The numerical formulation	14
2.3	Governing equations in generalized coordinates	14
2.4	Finite volume discretization	17
2.5	Spatial discretization of inviscid fluxes	18
2.6	Higher order spatial discretization	21
2.6.1	MUSCL extrapolation	21
2.7	Implicit time integration	22
2.8	Boundary conditions	25
2.8.1	Supersonic inflow	25
2.8.2	Subsonic inflow	26
2.8.3	Slip boundary or plane of symmetry	26
2.8.4	Viscous (no slip) condition, with non- or catalytic wall, isothermal or adiabatic	27
2.8.4.1	Partial catalytic wall condition	27
2.9	Selection of a numerical flux function	30
2.9.1	Flat plate	31
2.9.2	Hakkinen experiment	33
2.9.3	Holden ramp experiment	33
2.10	Conclusions	34
3	Verification and validation	37
3.1	Hollow cylinder flare test case	39
3.1.1	Introduction	39

3.1.2	Experimental test case	39
3.1.3	Numerical results	40
3.1.4	Conclusion	42
3.2	Hyperboloid-flare in F4	47
3.2.1	Introduction	47
3.2.2	Experimental test cases	47
3.2.3	Results of numerical simulations	48
3.2.4	Conclusion	50
3.3	RAM C-II flight experiment.	55
3.3.1	Introduction	55
3.3.2	Test case description	55
3.3.3	Results of numerical simulation	56
3.3.4	Conclusion	58
3.4	Conclusions	62
4	Hot hypersonic nozzle flow	63
4.1	Introduction	63
4.2	Nozzle Flow	65
4.2.1	Nozzle exit flow sensitivity	68
4.2.2	Nozzle wall distributions	72
4.3	Standard model Electre	76
4.3.1	Electre in the F4 facility	77
4.3.2	Electre in the HEG facility	78
4.3.3	Stagnation point heating	79
4.4	Conclusions	82
5	Application to three-dimensional re-entry flows	83
5.1	Atmospheric Re-entry Demonstrator	83
5.1.1	Background	84
5.1.2	Comparison of results in S4 Modane	85
5.1.3	Comparison of results with flight data	90
5.1.4	Conclusion	91
5.2	X-38 flight predictions	95
5.2.1	Background	95
5.2.2	Windward surface heating validation	100
5.2.3	Nose heating along trajectory	105
5.2.4	Prediction of free-flight hypersonic pitching moments	110
5.3	Conclusions	113
6	Conclusions	115
A	Physical modeling	117
A.1	Mass production rate due to chemical reactions	117

A.2	Vibration-Dissociation coupling	121
A.2.1	Park model	121
A.2.2	Treanor and Marrone model	122
A.3	Electronic energy reactive source term	123
A.4	Energy exchange mechanisms	125
A.4.1	Translational-Vibrational energy exchange	125
A.4.2	Vibrational-Vibrational energy exchange	127
A.4.3	Translational-Electronic energy exchange	128
A.4.4	Vibrational-Electronic energy exchange	129
A.5	Energy, enthalpy and specific heat	131
A.5.1	Translational mode	133
A.5.2	Electronic mode	133
A.5.3	Rotational- and vibrational mode	134
A.5.3.1	Hooke potential energy function	134
A.5.3.2	The Hulbert-Hirschfelder potential energy function	135
A.5.4	Comparison of different models for specific heats	139
A.6	Transport properties	140
A.6.1	Viscosity	140
A.6.2	Diffusion	140
A.6.3	Conductivities	141
B	Partial catalytic wall condition	143
C	Description of F4 and HEG wind tunnel	147
C.1	Description of hot-shot tunnel F4	147
C.2	Description of free piston driven shock tunnel HEG	148
List of Symbols		149
References		153
Summary		163
Samenvatting		165
Acknowledgments		167

1

Introduction

This thesis deals with the numerical simulation of hypersonic flows in experimental facilities and in flight conditions. Hypersonic flows are generally defined as flows with a Mach number exceeding 5. A brief historical review of hypersonic flow research is given in section 1.1. The physical phenomena which become more dominant with increasing Mach number are described in section 1.2. An overview of some common numerical techniques for these flow simulations is presented in section 1.3. Finally, the scope and objective of this thesis are given in section 1.4.

1.1 Historical perspective of hypersonic research

The first practical application of hypersonic flow theory occurred in the early 1940s, when researchers in Peenemünde were working on long distance ballistic missiles. For this purpose, the first hypersonic wind tunnel was built, capable of reaching a Mach number of 8, see Wegener [1997].

After World War II, the interest in hypersonic research for ballistic missiles was mainly driven by the competition between the United States and the former Soviet-Union. The technology in terms of knowledge and personnel transfer originated in both countries from the Germans. As an example, the knowledge about the German V-2 missile design was the basis for the development of Inter Continental Ballistic Missiles (ICBM's).

On October 14, 1947, in the United States, the Bell X-1 project resulted in the first sustained manned supersonic flight. The concept of this vehicle - also based upon research performed in Germany - was a thin winged vehicle with sharp leading edges. In the early 1950's plans were conceived for vehicles of sustained hypersonic flight. The aerodynamic design principles of such vehicles were initially the same as for the supersonic vehicles.

In that period, a large number of hypersonic ground test facilities became operational in both the U.S. and the former Soviet Union. At NASA Ames, H. Allen introduced the concept of blunt hypersonic vehicles to reduce heat loads, which was adopted as the basic aerodynamic design. This resulted in the Boeing X20A Dynasoar orbital hypersonic aircraft around 1960.

This project was canceled in favor of the Mercury capsule project to keep up with the Soviet-Union, which focused on capsule technology derived from nuclear warheads of ICBM's. As a result, the former Soviet-Union launched on October 4, 1957 *Sputnik*, the first satellite into earth orbit. The next step was to bring a manned vehicle into space. Again the former Soviet Union was the first to achieve this. The Soviet Union proved to be able to put a payload in orbit, which triggered large investments in the U.S. to catch up in the race for supremacy.

During the same period in the United States substantial experience was gained with winged hypersonic vehicles from the X-15 project, resulting in sustained Mach 7 flights. For space exploration the United States relied on rocket technology, which resulted in the Apollo program.

In 1960, NASA and the US AIR FORCE began to explore manned maneuverable lifting body spacecrafts, as an alternative to the ballistic re-entry concepts. This resulted in the PRIME project (Precision Recovery Including Maneuvering Entry). The PRIME vehicles (X-23A) demonstrated successfully that a maneuvering re-entry was feasible. After PRIME, the Air force derived the PILOT program (Piloted Low speed Tests) to test the supersonic, transonic, subsonic and landing behavior. This vehicle was designated X-24A.

Due to the changing economical situation and a decrease in public support after the Apollo Program, funds were reduced and more economical ways of getting payloads into earth orbit were considered. This led to studies into a fully reusable launcher in the late 1960's. The development costs of this type of launcher were, however, too high and a redirection to less ambitious designs was made. This resulted in the Space Shuttle program in the 1970's with its reusable Orbiter and expendable cryogenic external tank, as well as reusable solid boosters. The Shuttle design challenged research in hypersonics and triggered new experimental and numerical tool developments.

In the meantime progress had been made in the field of numerical simulations of flows. Moretti and Abbet [1966] were the first to publish two-dimensional Euler results for a blunt body, achieved by a time-marching finite-difference technique. However, this kind of numerical simulations were not used in the design process of the Space Shuttle in the early 1970's. The aerodynamic design of this vehicle was based on results of local inclination methods and boundary layer solvers, together with data from the experimental, cold hypersonic wind tunnels that were operational. High temperature effects could not be modeled properly and these were estimated with simplified mathematical models. As a consequence, experimental data from cold hypersonic wind tunnels were extrapolated to flight conditions with these simplified models.

An illustrative example is the first flight of the Space Shuttle, STS-1. This flight exhibited on the hypersonic entry phase a nose-up pitching moment increment relative to pre-flight predictions. This caused the body flap to deflect twice the amount thought necessary to achieve a trimmed flight. Although ample control power was available to overcome the under prediction of body flap deflection, the magnitude of the required deflection raised concerns about the structural and thermal integrity. The primary cause of this 'pitching moment anomaly' of

the Orbiter is contributed to high temperature effects, lowering the specific heat ratio, γ , in the flow field [Weilmuenster et al. 1993]. These effects were not duplicated in ground based facilities before the STS-1 flight. Lower specific heat ratios in the nose region and in the expansion region upstream of the body flap, which coincides with the largest planform, yield a nose-up pitching moment increment. On the other hand, as a consequence of local higher Mach numbers and lower γ upstream of the body flap and the reduced separated flow field, compared with the situation in a cold wind tunnel, a pressure increase on the flap reduces the pitching moment. However, the increase of the body flap effectiveness in flight is too small to compensate the nose-up pitching moment increment.

During the 1970's, the Apollo missions were abandoned, the design of the Space Shuttle was 'frozen' and the re-entry vehicle design for ballistic missiles was somewhat standardized. As a result, research in hypersonic flow fields decreased substantially and the available research capacity focused on the field of transonic aerodynamics, an important field for aviation development. This became a stimulus for the new area of Computational Fluid Dynamics (CFD).

In the second half of the 1980's, improvements in numerical techniques and the increase of computer power made it easier to embark on more advanced programs for reusable launchers or so-called space-planes: in the United States the Aero-Assisted Orbital Transfer Vehicle (AOTV), the National Aero Space Plane (NASP) and in Europe HERMES. As a consequence, the necessity to accurately predict the aerothermodynamic environment around the vehicles triggered the development of more sophisticated computational models, as well as experimental high enthalpy facilities with their associated measurement techniques, classical, as well as nonintrusive. From that period onwards, the development of advanced viscous flow solvers including high temperature nonequilibrium effects started. The thermo-chemical models in these flow solvers are usually based on quantum and statistical mechanics supplemented with semi-empirical data. Most of these models were derived prior and during the 1960's and have to be validated against wind tunnel and flight experiments.

Therefore, data from hypersonic ground test facilities are still necessary for the design of space vehicles, although their capabilities to simulate re-entry conditions are limited. Experimental facilities capable to simulate hypersonic flows have become operational again in the U.S., e.g. the LENS shock-tube (Buffalo). In Europe during the HERMES program and the subsequent Manned Space Transportation Program (MSTP), two major high enthalpy facilities were developed: in France the Arc jet F4 wind tunnel at ONERA (Le Fauga) and in Germany the piston driven shock-tube HEG at DLR (Göttingen).

Ground based facilities, however, cannot realize the combination of freestream velocity, density and model geometry of many flight conditions and therefore they only simulate partially the flow characteristics occurring in flight. Let this be made clear by the following example: The time required for dissociation to occur is proportional to the density times a reference length, ρL , whereas for a recombination it is proportional to the square of the density times a reference length $\rho^2 L$. [Vincenti and Kruger 1965] This implies that if a wind tunnel test is developed in order to study the forebody, which is dominated by dissociation, and scaled with

ρL , the base flow will be closer to equilibrium than in flight because $\rho^2 L$ cannot be realized at the same time. In addition to this approximate simulation, there are several reasons why a wind tunnel cannot reproduce all hypersonic re-entry conditions:

- The thermal and chemical state of the flow in the test section does not match free flight conditions,
- the off-design operation conditions of a given wind tunnel nozzle cause a nonuniform freestream over the model,
- the high temperature reservoir conditions lead to erosion of the internal facility surfaces which, in turn, contaminate the freestream,
- and the test facilities, such as shock tubes, have very limited test times (order of milliseconds), such that stationary flow establishment has to be verified.

In total, it is impossible to simulate hypersonic flight conditions completely. Although the high enthalpy facilities have serious limitations, they allow certain aspects to be examined, which are expected to be important in flight. We return to these considerations in Chapter 4.

1.2 Relevant physics of hypersonic flows

The hypersonic flow regime is defined as the regime where the freestream Mach number becomes high enough, typically at a Mach number exceeding 5; in this regime a number of phenomena become progressively more important with increasing Mach number, such as viscous interaction -, high temperature - and low density effects.

One of these phenomena is the presence of strong shock waves close to the surface of the body at high Mach numbers. The relatively small part of the flow field between the bow shock and the surface in hypersonic flow is called the shock layer. For increasing Mach numbers the shock angle decreases, making the shock layer smaller. At the same time the boundary layer thickness grows proportional to $\frac{M^2}{\sqrt{Re_x}}$, causing the boundary layer thickness to be relatively large with respect to the shock layer thickness. Therefore in hypersonic flows viscous and inviscid effects interact strongly. The classical concept of a boundary layer fails and only a fully viscous approach should be used to model the hypersonic flow properly.

While increasing the freestream Mach number from supersonic to hypersonic values, the temperature behind the bow shock will become so high that internal energy modes (vibration, electron excitation) of the molecules become significant, leading ultimately to dissociation of the diatomic gas molecules and to ionization. The gas may then emit or absorb radiation. This causes the flow properties to deviate from perfect gas values. In expanding regions of the flow field, the gas cools. The constituents may recombine and the internal energy states may relax to lower energy levels. The thermo-chemical excitation of vibration, dissociation, ionization, and radiation are commonly referred to as high-temperature effects.

At low temperature ($< 800\text{K}$) a mixture of gases, such as air for example, can be modeled as a mixture of calorically perfect gases having constant specific heats since only the translational and rotational modes are fully excited. When the temperature of the air is increased above 800 K, vibrational excitation of the molecules may occur, and this causes the specific heats to become a function of temperature; the gas is said to be thermally perfect. As the air temperature is increased above 2500 K, chemical reactions occur and air becomes a chemically reacting mixture of thermally perfect gases, leading to dissociation in the gas. Although the individual constituents of the mixture behave as a thermally perfect gas, this is not the case for the mixture itself. The specific heats, for example, of the mixture are functions of both temperature and pressure. The chemical reactions and the storage of energy in the internal modes tend to regulate the temperature in the flow. Above 9000 K, ions are formed and the gas becomes a partially ionized plasma.

The high temperature phenomena described above are triggered by collisions between the molecules. To reach a full excitation of e.g. the vibrational energy mode, a molecule needs to collide a number of times with other molecules. The same holds for a chemical reacting media to reach its equilibrium composition. In general these processes have characteristic time scales. If the characteristic time scale to reach thermal equilibrium is small compared to the characteristic time of the flow, the flow is in thermal equilibrium. Similarly, if the characteristic time scale of the chemical processes is small compared to the characteristic time of the flow, the flow is in chemical equilibrium. In all other cases the flow is said to be in nonequilibrium. A special case of nonequilibrium flow is the so-called 'frozen flow', in which the characteristic time scales of both thermal and chemical processes are orders of magnitude larger than the characteristic time scale of the flow.

All the phenomena described above occur when a space vehicle, after deorbiting, re-enters the atmosphere.

1.3 Numerical techniques

In section 1.1 it was mentioned that Moretti and Abbet [1966] used a time-marching finite-difference technique. Time-marching methods to calculate steady flow fields are used in most flow solvers. In these methods the calculation starts from an initial solution, usually the freestream conditions applied to the whole flow field, and the time rate of change of the flow field quantities is computed at every point. Taking a small time-step, at every point, quantities can now be updated. This process is repeated until the updates become smaller than a certain tolerance, which is defined as convergence. Moretti and Abbott used the so-called Lax-Wendroff finite-difference technique. The Lax-Wendroff method is second order accurate, explicit in time and uses central differences in space. A characteristic of this method is the combined space and time discretization. A simpler variant is the method of MacCormack [1969] which is a explicit, predictor-corrector method widely used throughout the 1970's and 1980's.

Methods originally developed for the Euler equations can also be applied to the Navier-Stokes equations, where the viscous terms are discretized centrally.

Other space-centered discretization methods were developed with multi-stage time integration. An explicit scheme, applying fourth-order Runge-Kutta time-integration method was introduced by Jameson et al. [1981]. All space-centered methods suffer to some extent from oscillations in the solution. To solve this problem, in Jameson's method, an additional diffusion term is added that introduces numerical diffusion in regions with sharp gradients.

Alternative discretization methods were developed which introduce some physical properties of the flow into the discretized formulation. These methods are called *upwind* schemes, which relate the differencing to the characteristic propagation properties of the Euler equations. Usually these schemes are applied to finite volume discretization methods in which the Navier-Stokes or Euler equations are discretized in conservative form.

1.4 Objective and scope of present work

As mentioned in section 1.1, it is hardly possible to simulate free flight conditions, in all its aspects, in a wind tunnel. On the other hand wind tunnel experiments are indispensable in getting insight into the physics and provide valuable data for specific flow phenomena. Therefore, the numerical simulation is of crucial importance to bridge the gap between wind tunnel experiments and free flight conditions. In addition it provides a better understanding of the facility performance, and it supports the interpretation of experimentally measured data. A reliable extrapolation to flight conditions of a space vehicle can be achieved by a well validated CFD tool and well understood experimental data.

The objective of this thesis is to present numerical simulations of hypersonic flows in both experimental facilities and flight conditions. In this way a contribution is provided to the understanding of high temperature effects in high enthalpy flows. For this purpose, an efficient, robust thermo-chemical nonequilibrium Navier-Stokes solver, called LORE, has been developed and validated. It is built on previous work in hypersonics through the combination of modern computational techniques, and various up-to-date thermo-chemical models. An assessment of the thermo-chemical models is made through comparison with available experimental data.

Since the time scales of the flow and the chemistry can be orders of magnitude apart in a nonequilibrium flow field, a fully coupled system of equations is solved implicitly using a first order time accurate, line Gauss-Seidel method. Numerical Jacobians have been constructed in order to treat the thermo-chemical formulations implicitly in time. The work is novel, in that, general shapes can be computed on any vector as well as distributed memory parallel machine. General multi-block structured grids can be used to analyze complex geometries.

The underlying mathematical and numerical formulation of the governing equations including thermo-chemical models is presented in Chapter 2. The implementation, validation and

comparison of different discretization techniques for viscous hypersonic flows is examined.

In Chapter 3, the performance of the chosen numerical scheme is investigated by comparing CFD predictions with available experimental data in cold hypersonic conditions. In the same way, the suitable hot hypersonic conditions are chosen for evaluation of the performance of the physical model employed in the CFD code. The main objective of this chapter is to assess the accuracy in the numerical scheme as well as the physical models employed. The test cases selected cover the complete hypersonic flow regime. They range from perfect gas to thermo-chemical nonequilibrium ionized gas in the hypersonic flow regime. Moreover, all test cases are in laminar flow conditions to avoid the uncertainty from turbulence modeling in this validation exercise.

In Chapter 4 the objective is to perform a sensitivity analysis of the influence of different thermo-chemical models on the F4 (ONERA) and HEG (DLR) hypersonic nozzle flows as well as on the flow past the Electre blunt cone standard test model. The solutions are compared to experimental data and computational results obtained from ONERA, DLR and CIRA. In these computations a number of assumptions are made concerning the calculation of the nozzle expansion flow. The analysis focuses on the sensitivity of the results upon these assumptions. The adequacy of the nozzle wall and model measurements for the validation of the computational models are addressed.

In Chapter 5 the ARD capsule and the X-38 demonstrator are computed for both wind tunnel and flight measurements showing the capability to assess general three-dimensional configurations. Global aerodynamic characteristics as well as detailed pressure and heat flux assessments are presented.

In Chapter 6 the conclusions are drawn in which the lessons learned of the ability to predict and understand hypersonic flow fields are discussed.



2

Governing equations for high temperature gas flows

In this chapter the governing equations are presented for a viscous flow comprising a multi-species gas that is thermally excited and chemically reacting. These equations are based on the well-known Navier-Stokes equations for a perfect gas which are mathematical expressions of the principle of conservation of mass, momentum and energy. They are supplemented with conservation equations of the different species and equations modeling different types of energies of the thermally excited molecules.

It is assumed that each of the species of the mixture behaves as a perfect gas. Furthermore the equations derived from the Navier-Stokes equations, limit the validity of the model to a continuum. This means that they are valid if the transport terms can be expressed as lower order macroscopic quantities.

The models used for the transfer of mass, momentum and energy are summarized in section 2.1 and explained into details in Appendix A. The assumptions and limitations imposed on these models will be discussed. Hereafter, the numerical implementation of the aforementioned partial differential equations will be addressed.

2.1 The flow equations in conservative form

Assuming a mixture of thermally perfect gases, each species obeys the perfect gas equation. The mixture density ρ and mixture pressure p can be found by summing over the partial densities and partial pressures of all species, respectively:

$$\rho = \sum_s \rho_s = \rho \sum_s c_s , \quad (2.1a)$$

$$p = \sum_{s \neq e} p_s + p_e = T \sum_{s \neq e} \left(\rho_s \frac{\mathcal{R}}{M_s} \right) + T_e \rho_e \frac{\mathcal{R}}{M_e} , \quad (2.1b)$$

where \mathcal{R} denotes the universal gas constant, M_s the molecular weight, $c_s = \frac{\rho_s}{\rho}$ is the mass-fraction of species s . p_e, T_e, ρ_e, M_e are the electron pressure, temperature, density and molecular weight, respectively. It is assumed that all species have the same translational temperature T , except for electrons, which have a translational electron temperature T_e . The pressure is only a function of the translational temperatures, since only the translational part of the energy effects the pressure [Vincenti and Kruger 1965].

The total energy E per unit mass, being the sum of the internal and kinetic energies, is defined as:

$$E = \frac{1}{2} (u^2 + v^2 + w^2) + \sum_s \frac{\rho_s e_s}{\rho} , \quad (2.2)$$

where e_s is the internal energy of species s per unit mass, and u, v, w are the velocity components in x, y, z -directions respectively. The energy e_s consists of the translational, rotational, vibrational and electronic mode and its zero point energy:

$$e_s = e_{tr_s} + e_{rot_s} + e_{v_s} + e_{e_s} + e_{0_s} . \quad (2.3)$$

The total enthalpy H per unit mass is defined by:

$$H = E + \frac{p}{\rho} . \quad (2.4)$$

The conservation equations, for a k -dimensional viscous flow in thermal and chemical nonequilibrium comprising s species of which m are diatomic ($m \leq s$), can be written as follows [Gnoffo et al. 1989]:

$$\frac{\partial \vec{Q}}{\partial t} + \frac{\partial \vec{F}^k}{\partial x^k} = \vec{\Omega} . \quad (2.5)$$

Equation (2.5) represents a system modeling s species continuity equations for each species separately, k mixture momentum equations, m vibrational energy equations, the electron excitation energy equation, and the total energy equation. The structure of the system of equation (2.5) is given by the vectors (2.6) till (2.9). The variables to be conserved per unit volume are the components of the state vector \vec{Q} :

$$\vec{Q} = (\rho_s, \rho u^i, \rho_m e_{v_m}, \rho_e e_e, \rho E)^T . \quad (2.6)$$

Subscript e denotes the variables related to the electron. The flux vector \vec{F}^k is split into an inviscid \vec{F}_{inv}^k and viscous part \vec{F}_{vis}^k :

$$\vec{F}_{inv}^k = \begin{bmatrix} \rho_s u^k \\ \rho u^i u^k + p \delta^{ik} \\ \rho_m e_{v_m} u^k \\ \rho e_e u^k \\ \rho H u^k \end{bmatrix} , \quad (2.7)$$

$$\vec{F}_{vis}^k = \left[\begin{array}{c} -\rho D \underbrace{\frac{\partial c_s}{\partial x^k}}_1 \\ -\mu \underbrace{\left(\frac{\partial u^i}{\partial x^k} + \frac{\partial u^k}{\partial x^i} - \frac{2}{3} \frac{\partial u^j}{\partial x^j} \delta^{ik} \right)}_3 \\ -c_m k_{v_m} \underbrace{\frac{\partial T_{v_m}}{\partial x^k}}_4 - \rho \sum_m h_{v_m} D \underbrace{\frac{\partial c_m}{\partial x^k}}_5 \\ -c_e k_e \underbrace{\frac{\partial T_e}{\partial x^k}}_{10} - \rho \sum_s h_{e_s} D \underbrace{\frac{\partial c_s}{\partial x^k}}_{11} \\ -\underbrace{\vec{q}_T}_{17} - \underbrace{\left[\rho \sum_s h_s D \frac{\partial c_s}{\partial x^k} \right]}_{18} - u^i \mu \underbrace{\left[\left(\frac{\partial u^i}{\partial x^k} + \frac{\partial u^k}{\partial x^i} \right) - \frac{2}{3} \frac{\partial u^j}{\partial x^j} \delta^{ik} \right]}_{19} \end{array} \right], \quad (2.8)$$

$$\text{where } \vec{q}_T = \left[k_{tr} \frac{\partial T}{\partial x^k} + c_m k_{v_m} \frac{\partial T_{v_m}}{\partial x^k} + c_e k_e \frac{\partial T_e}{\partial x^k} \right].$$

The thermal-chemical source term $\vec{\Omega}$ takes into account the modeling of the chemical reactions and the thermal energy transfer over the different energy modes:

$$\vec{\Omega} = \left[\begin{array}{c} \omega_s \underbrace{2}_0 \\ Q_{T-V} + Q_{V-E} + Q_{V-D} + Q_{V-V} \underbrace{6}_7 \underbrace{8}_9 \\ u^k \frac{\partial p_e}{\partial x^k} - \frac{\partial p_e u^k}{\partial x^k} + Q_{T-E} - \sum_m Q_{V-E} - Q_{ERS} \underbrace{12}_{13} \underbrace{14}_{15} \underbrace{0}_{16} \end{array} \right]. \quad (2.9)$$

In the *species conservation equation* the first two terms represent the rate of change of mass of species s per unit volume and the flux of mass of species s convected with the mixture's velocity u^k . Term (1) accounts for the diffusion of species s . In a gas mixture the mass diffusion of the separate species can be described in terms of diffusion velocities. Assuming that the diffusive fluxes due to temperature gradients are negligible, the diffusion velocity of each component of the gas mixture is proportional to the gradient of the mass fraction. D denotes the diffusion coefficient for all the species and is explained in Appendix A.6.

Term (2) accounts for the mass production rate ω_s of species s due to chemical reactions. The composition of ω_s is the subject of Appendix A.1.

In the *momentum conservation equation* the first three terms represent the rate of change of the i th momentum component per unit volume and the flux of the i th momentum component convected with the mixture's velocity u^k and the pressure gradient acting in the i th direction. The mixture's dynamic viscosity μ is used to determine the shear stresses in term (3), assuming zero bulk viscosity.

In the set of *vibrational energy equations*, the first two terms represent the rate of change of the vibrational energy of species m per unit volume and the flux of vibrational energy e_{v_m} convected with mixture's velocity u^k . Term (4) represents the conduction of vibrational energy of species m due to vibrational energy gradients in which k_{v_m} denotes the thermal conductivity of the vibrational energy of species m . The expression for thermal conductivities is given in Appendix A.6. Term (5) represents the diffusion of vibrational energy due to molecular species mass fraction gradients in which h_{v_m} is the vibrational enthalpy per unit mass, D denotes the diffusion coefficient. The quantities h_{v_m} and D are discussed in Appendix A.5 and A.6 respectively. In a mixture of thermally excited gases, there exists an energy exchange (relaxation) between translational and vibrational modes (T-V) due to molecular collisions, represented by term (6). Similarly, term (7) accounts for the energy exchange (relaxation) between vibrational and electronic modes (V-E). The expressions for the T-V and V-E exchange are given in Appendix A.4.1 and A.4.4. Term (8) is due to the energy exchange between vibration and dissociation (V-D). Two models are used: the Park and the Treanor-Marrone model. They are explained in Appendix A.2. This coupling describes also the effect of vibrational relaxation on the dissociation reaction rate.

If one vibrational temperature T_v is used to characterize the vibrational energy of all the diatomic molecules, one average vibrational energy conservation equation for all diatomic species is solved. The average vibrational equation for all diatomic species will have the form of a summation over all vibrational energy equations for species m . The average vibrational energy per unit mass yields:

$$e_v = \sum_m \frac{\rho_m e_{v_m}}{\rho} \quad T_{v_m} = T_v \neq T_e \quad , \quad (2.10a)$$

$$e_v = \sum_m \frac{\rho_m e_{v_m}}{\rho} + \sum_s \frac{\rho_m e_{e_m}}{\rho} \quad T_{v_m} = T_v = T_e \quad . \quad (2.10b)$$

Note that the last term of equation (2.10b) denotes the electron excitation energy of the species. If for each diatomic molecule a different vibrational temperature is chosen, a vibrational energy conservation equation for each diatomic species m is solved. Similarly, if the electron and electronic excitation energy equation is not included in the average vibrational energy, the corresponding electronic excitation energy is added separately as vibrational energy equation.

In a multiple vibrational temperature model, term (9) accounts for the exchange between the different vibrational energies of each diatomic species m . This term is explained in Appendix A.4.2.

In the *electron and electronic excitation energy equation*, it is assumed that all electronic states of all molecules and the translational energy of free electrons can be characterized by a Maxwell distribution at T_e . The average electronic energy per unit mass e_e , representing the energy from the electronic energy levels of all the species, is the sum of the electronic energy per unit mass of species s :

$$e_e = \sum_s \frac{\rho_s e_{e_s}}{\rho}. \quad (2.11)$$

Term (10) represents the conduction of electronic energy and term (11) the diffusion of electronic energy due to mass fraction gradients. In these terms k_e is the thermal conductivity for the electrons and h_{e_s} is the electronic excitation enthalpy of species s . The quantities k_e and h_{e_s} are discussed in Appendix A.5 and A.6, respectively.

The electron velocity is assumed to be equal to the ion velocity. No conduction current in the flow field is assumed. Since the electron mass is small, the electron momentum and viscous stress contributions are neglected. This leads to the assumption that the electric field is proportional to the electron pressure gradient, yielding to term (12) for the work done on electrons by an electrical field induced by the electron pressure gradient. Term (13) accounts for the electron pressure part of the flux convected with the mixture's velocity u^k . Term (14) represents the energy exchange (T-E) due to elastic collisions between heavy particles and electrons. This T-E energy exchange term is discussed in Appendix A.4.3. Term (15), corresponding to term (7), represents the energy exchange (relaxation) due to inelastic collisions between electrons and heavy particles. Term (16), Q_{ERS} , represents the energy loss due to electron impact ionization, when a free electron strikes a neutral particle and ionizes it (see Appendix A.3).

The first two terms of the *total energy conservation equation* represent the rate of change of total energy per unit volume ρe and the flux of total enthalpy ρh convected with the mixture's velocity u^k . Term (17) represents the conduction and term (18) the diffusion of enthalpy due to mass fraction gradients, term (19) accounts for the work done by the shear forces.

2.2 The numerical formulation

Since analytical solutions of the Navier-Stokes equations are only available for a few very simple geometries, one approximates the continuous system of equations by a system of discrete algebraic equations. Various discretizing techniques may be used, for instance: the finite-difference technique, the finite-volume technique and the finite-element technique. In this thesis, the finite-volume technique has been selected by which the integral formulation of the conservation equations is discretized. The integral formulation ensures that mass, momentum and energy will be conserved at the discrete level.

A certain class of numerical schemes designed to stably discretize the fluxes arising from these hyperbolic equations is termed *upwind schemes*, Hirsch [1988]. Two types of upwind schemes exist. One family is based on a directional discretization of the flux derivatives, the so-called Flux-Vector-Splitting (FVS) methods. Examples of this type are the schemes of Steger and Warming [1981] and Van Leer [1983]. The second family, Flux-Difference-Splitting (FDS), is based on an idea originally introduced by Godunov [1959]. This method solves for every mesh interval the one-dimensional Riemann problem for discontinuous neighboring states (the states at both sides of the cell face). This method results in a complex, time consuming solution procedure. Therefore, methods have been developed which give an approximate solution of this Riemann problem. Examples of these approximate Riemann solvers are introduced by Osher [1982] and Roe [1983].

It has been shown by numerous investigations that upwind schemes can be developed which allow for a high resolution of discontinuities, such as shocks and contact discontinuities without spurious oscillations. This is important since hypersonic viscous flows may exhibit strong shocks and strong expansions near to vacuum. To obtain a numerical solution without oscillations, a large numerical dissipation is required in the proximity of shocks. The interaction of embedded shocks in boundary layers, on the other hand, needs rather less dissipation.

The discretization procedure of the governing partial differential equations and the solution technique are presented and discussed in this chapter. The spatial discretization uses the AUSM-Van Leer scheme [Wada and Liou 1994] for the inviscid fluxes and a central difference scheme for the viscous fluxes. The solution technique is based on an implicit time integration towards the steady state. The system of equations is discretized first order accurate in time, by linearization of the fluxes, which leads to an algebraic system of equations. This algebraic system is then solved using a line-Gauss-Seidel relaxation method.

2.3 Governing equations in generalized coordinates

In a Cartesian coordinate system the governing equations for a three-dimensional flow, comprising an s species mixture of thermally perfect gases, in thermal and chemical nonequilibrium may be written as:

$$\vec{Q}_t + \vec{E}_x + \vec{F}_y + \vec{G}_z = \vec{\Omega} , \quad (2.12)$$

where \vec{Q} is the vector of the conservative variables and $\vec{\Omega}$ contains the thermo-chemical source terms:

$$\begin{aligned}\vec{Q} &= (\rho_s, \rho u, \rho v, \rho w, \rho_m e_{v_m}, \rho e_e, \rho E)^T, \\ \vec{\Omega} &= (\omega_s, 0, 0, 0, \omega_{v_m}, \omega_e, 0)^T.\end{aligned}\quad (2.13)$$

The flux vectors \vec{E} , \vec{F} and \vec{G} in x -, y - and z -direction, respectively, are defined as:

$$\begin{aligned}\vec{E} &= \begin{bmatrix} \rho_s u - \rho_s D_s c_{s_x} \\ \rho u u - \sigma_{xx} \\ \rho v u - \sigma_{xy} \\ \rho w u - \sigma_{xz} \\ \rho_m e_{v_m} u - q_{t_{v_m x}} \\ \rho_m e_e u - q_{t_e x} \\ (e - \sigma_{xx}) u - \sigma_{xy} v - \sigma_{xz} w - q_{T_x} - q_{d_x} \end{bmatrix}, \\ \vec{F} &= \begin{bmatrix} \rho_s v - \rho_s D_s c_{s_y} \\ \rho u v - \sigma_{yx} \\ \rho v v - \sigma_{yy} \\ \rho w v - \sigma_{yz} \\ \rho_m e_{v_m} v - q_{t_{v_m y}} \\ \rho_m e_e v - q_{t_e y} \\ (e - \sigma_{yy}) v - \sigma_{yx} u - \sigma_{yz} w - q_{T_y} - q_{d_y} \end{bmatrix}, \\ \vec{G} &= \begin{bmatrix} \rho_s w - \rho_s D_s c_{s_z} \\ \rho u w - \sigma_{zx} \\ \rho v w - \sigma_{zy} \\ \rho w w - \sigma_{zz} \\ \rho_m e_{v_m} w - q_{t_{v_m z}} \\ \rho_m e_e w - q_{t_e z} \\ (e - \sigma_{zz}) w - \sigma_{zx} u - \sigma_{zy} v - q_{T_z} - q_{d_z} \end{bmatrix}.\end{aligned}\quad (2.14)$$

in which the stress components are given by:

$$\begin{aligned}\sigma_{xx} &= -p - \frac{2}{3}\mu(-2u_x + v_y + w_z), \\ \sigma_{yy} &= -p - \frac{2}{3}\mu(u_x - 2v_y + w_z), \\ \sigma_{zz} &= -p - \frac{2}{3}\mu(u_x + v_y - 2w_z), \\ \sigma_{xy} &= \sigma_{yx} = \mu(u_y + v_x), \\ \sigma_{xz} &= \sigma_{zx} = \mu(w_x + u_z), \\ \sigma_{yz} &= \sigma_{zy} = \mu(w_z + v_y).\end{aligned}\quad (2.15)$$

Since one is interested in the application of the numerical method to an arbitrary configuration, a general transformation of the coordinates (x, y, z) from the physical domain to the generalized coordinates (ξ, η, ζ) in the computational domain will be used

$$x = x(\xi, \eta, \zeta), \quad y = y(\xi, \eta, \zeta), \quad z = z(\xi, \eta, \zeta). \quad (2.16)$$

Using the chain rule of partial differentiation the metric terms can be derived

$$\begin{aligned}\xi_x &= (y_\eta z_\zeta - y_\zeta z_\eta) ; \quad \eta_x = (z_\xi y_\zeta - y_\xi z_\zeta) ; \quad \zeta_x = (y_\xi z_\eta - z_\xi y_\eta) , \\ \xi_y &= (z_\eta x_\zeta - z_\zeta x_\eta) ; \quad \eta_y = (x_\xi z_\zeta - z_\xi x_\zeta) ; \quad \zeta_y = (z_\xi x_\eta - x_\xi z_\eta) , \\ \xi_z &= (x_\eta y_\zeta - y_\eta x_\zeta) ; \quad \eta_z = (y_\xi x_\zeta - x_\xi y_\zeta) ; \quad \zeta_z = (x_\xi y_\eta - y_\xi x_\eta) .\end{aligned}\quad (2.17)$$

(ξ_x, ξ_y, ξ_z) , (η_x, η_y, η_z) and $(\zeta_x, \zeta_y, \zeta_z)$ can be considered as Cartesian components of the surface normal of a cell face $\xi = \text{constant}$, $\eta = \text{constant}$ and $\zeta = \text{constant}$, respectively. The Jacobian determinant of the transformation or the volume of the cell J is given as

$$J = \frac{\partial(x, y, z)}{\partial(\xi, \eta, \zeta)} = \begin{vmatrix} x_\xi & x_\eta & x_\zeta \\ y_\xi & y_\eta & y_\zeta \\ z_\xi & z_\eta & z_\zeta \end{vmatrix}. \quad (2.18)$$

Using this transformation, the Navier-Stokes equations in generalized coordinates are

$$\hat{Q}_t + \hat{E}_\xi + \hat{F}_\eta + \hat{G}_\zeta = \hat{\Omega}, \quad (2.19)$$

where \hat{Q} , \hat{E} , \hat{F} , \hat{G} and $\hat{\Omega}$ have the form:

$$\begin{aligned}\hat{Q} &= J \vec{Q}, \\ \hat{E} &= (\vec{E}\xi_x + \vec{F}\xi_y + \vec{G}\xi_z), \\ \hat{F} &= (\vec{E}\eta_x + \vec{F}\eta_y + \vec{G}\eta_z), \\ \hat{G} &= (\vec{E}\zeta_x + \vec{F}\zeta_y + \vec{G}\zeta_z), \\ \hat{\Omega} &= J \vec{\Omega}.\end{aligned}\quad (2.20)$$

2.4 Finite volume discretization

The Navier-Stokes equations (2.19) can be written in integral form, which is the basis for a finite volume formulation. For an arbitrary control volume V with boundary ∂V equation (2.19) becomes: (using the Gauss theorem)

$$\iiint_V \frac{\partial \hat{Q}}{\partial t} dV + \iint_{\partial V} (\hat{E}n_\xi + \hat{F}n_\eta + \hat{G}n_\zeta) d\partial V = \iiint_V \hat{\Omega} dV , \quad (2.21)$$

where $\vec{n} = (n_\xi, n_\eta, n_\zeta)^T$ is the outward unit normal vector at ∂V in ξ, η, ζ space. A straightforward discretization of equation (2.21) is given by the finite volume method. For a Cartesian grid in ξ, η, ζ space with disjunct cells $V_{i,j,k}$, in which i, j and k denote the indices of the cell center, the finite volume discretization becomes:

$$\begin{aligned} & \iint_{V_{i,j,k}} \frac{\partial \hat{Q}}{\partial t} d\xi d\eta d\zeta + \\ & \int_{S_{i+\frac{1}{2},j,k}} \hat{E} d\eta d\zeta - \int_{S_{i-\frac{1}{2},j,k}} \hat{E} d\eta d\zeta + \int_{S_{i,j+\frac{1}{2},k}} \hat{F} d\xi d\zeta - \int_{S_{i,j-\frac{1}{2},k}} \hat{F} d\xi d\zeta \\ & + \int_{S_{i,j,k+\frac{1}{2}}} \hat{G} d\xi d\eta - \int_{S_{i,j,k-\frac{1}{2}}} \hat{G} d\xi d\eta = \iint_{V_{i,j,k}} \hat{\Omega} d\xi d\eta d\zeta . \end{aligned} \quad (2.22)$$

The cell faces of $V_{i,j,k}$ are $S_{i+\frac{1}{2},j,k} \dots S_{i,j,k-\frac{1}{2}}$. The mean values of \hat{Q} and $\hat{\Omega}$ are located at the cell centers. The flux vectors \hat{E}, \hat{F} and \hat{G} are assumed to be constant over the cell face.

So we arrive at a system of ordinary differential equations with respect to time

$$\frac{d \hat{Q}_{i,j,k}}{d t} + \frac{\hat{E}_{i+\frac{1}{2},j,k} - \hat{E}_{i-\frac{1}{2},j,k}}{\Delta \xi} + \frac{\hat{F}_{i,j+\frac{1}{2},k} - \hat{F}_{i,j-\frac{1}{2},k}}{\Delta \eta} + \frac{\hat{G}_{i,j,k+\frac{1}{2}} - \hat{G}_{i,j,k-\frac{1}{2}}}{\Delta \zeta} = \hat{\Omega}_{i,j,k} , \quad (2.23)$$

where $\Delta \xi, \Delta \eta$ and $\Delta \zeta$ denote the cell spacings in the computational domain and the integrated fluxes on the faces are defined as for example for:

$$\hat{E}_{i+\frac{1}{2},j,k} = \frac{1}{\Delta \eta \Delta \zeta} \iint_{S_{i+\frac{1}{2},j,k}} \hat{E} d\eta d\zeta . \quad (2.24)$$

Note that although all variables are defined at the centers of the cells, (2.24) requires the knowledge of the fluxes at intermediate points. In the next section 2.5 the procedure for the computation of the integrated flux vectors $\hat{E}_{i+\frac{1}{2},j,k} \dots \hat{G}_{i,j,k-\frac{1}{2}}$ functions will be described.

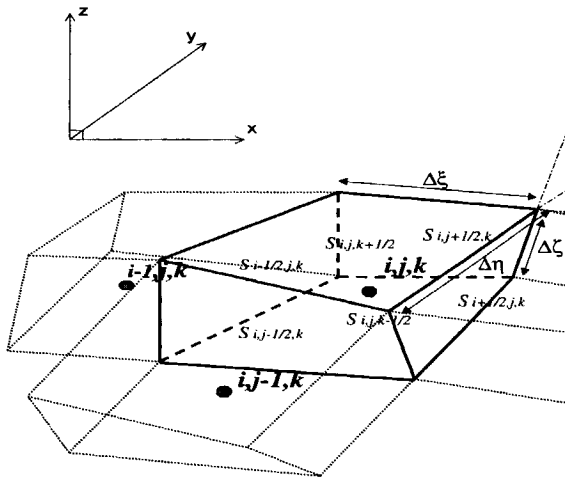


Figure 2.1: Control volume for flux calculation

2.5 Spatial discretization of inviscid fluxes

The flux vectors \hat{E} , \hat{F} and \hat{G} on the cell faces have to be calculated by numerical flux functions. The calculation of these numerical flux functions is based on the Godunov principle. This means that the flux on the cell faces is computed by means of an (approximate) solution of the one-dimensional Riemann problem at the cell faces. Since the exact solution of the local one-dimensional Riemann problem is very expensive, schemes have been developed which solve the local one dimensional Riemann problem approximately. They are commonly referred to as flux vector-splitting schemes (FVS)[Van Leer 1983] and flux difference splittings schemes (FDS)[Roe 1983]. In the flux vector splitting method the flux terms are split according to the sign of the associated characteristic propagation speeds. In the flux difference splittings schemes the solution is based on a characteristic decomposition of the flux differences. In this thesis the flux vector splitting method (FVS) will be used.

For the cell interface $i + \frac{1}{2}, j, k$, the numerical flux function may be written as

$$\hat{E}_{i+\frac{1}{2},j,k} = \hat{E}_{i+\frac{1}{2},j,k}(\hat{Q}_{i+\frac{1}{2},j,k}^L, \hat{Q}_{i+\frac{1}{2},j,k}^R), \quad (2.25)$$

where $\hat{Q}_{i+\frac{1}{2},j,k}^L$ and $\hat{Q}_{i+\frac{1}{2},j,k}^R$ represent an approximation to the states on either side of the cell interface, obtained from an inter- or extrapolation of the centers of the neighboring finite volumes. A plausible choice would be to take $\hat{Q}_{i+\frac{1}{2},j,k}^L = \hat{Q}_{i,j,k}$ and $\hat{Q}_{i+\frac{1}{2},j,k}^R = \hat{Q}_{i+1,j,k}$ which leads to a first order accurate scheme. The development of higher order scheme will be deferred to the next section. In the following the states \hat{Q}^L and \hat{Q}^R are assumed to be given.

The main drawback is the numerical dissipation created in shear- and boundary layers. Numerous attempts have been undertaken to improve the accuracy of the original Van Leer FVS concept, by reducing the dissipation in the convective part of momentum flux [Schwane and Hänel 1987; Kroll and Radespiel 1993]. The Advection Upwind Splitting Method (AUSM) can be considered as an generalization of these modifications [Liou and Steffen 1993; Wada and Liou 1994; Walpot and Schwane 1994].

Before defining various flux approximations, some concepts need to be introduced.

The convective velocity \tilde{u} normal to the face $i + \frac{1}{2}$ is defined as:

$$\tilde{u} = \frac{u\xi_x + v\xi_y + w\xi_z}{S_{i+\frac{1}{2}}} , \quad (2.26)$$

in which u, v and w are the velocity components, taken left or right from the cell face. The left or right decision will be made a few steps later. How these values are obtained will be explained in section 2.6. $S_{i+\frac{1}{2}}$ denotes the area of cell face $i + \frac{1}{2}$ is given by:

$$S_{i+\frac{1}{2}} = \sqrt{\xi_x^2 + \xi_y^2 + \xi_z^2} . \quad (2.27)$$

The normal velocity component to a side can be decomposed into the two splitted velocities u_{\pm} defined by

$$u_{\pm} = \begin{cases} \pm \frac{1}{4a} (\tilde{u} \pm a)^2 , & \text{if } |\tilde{u}| \leq a , \\ \frac{1}{2} (\tilde{u} \pm |\tilde{u}|) , & \text{otherwise ,} \end{cases} \quad (2.28)$$

in which a denotes the speed of sound and the subscripts \pm respectively denote the “non-negative” and “non-positive” portions of \tilde{u} . Similarly, the pressure can be decomposed into the split pressures p_{\pm} as follows:

$$p_{\pm} = \begin{cases} p(\tilde{u}/a \pm 1)^2 (2 \mp \tilde{u}/a)/4 , & \text{if } |u| \leq a , \\ p(\tilde{u} \pm |\tilde{u}|)/2\tilde{u} , & \text{otherwise .} \end{cases} \quad (2.29)$$

With the definition of the split normal velocity and the split pressure, one can define the Mach number and the pressure at the cell interface by:

$$\begin{aligned} M_{i+\frac{1}{2}} &= M_+^L + M_-^R = \frac{\tilde{u}_+^L}{a^L} + \frac{\tilde{u}_-^R}{a^R} , \\ p_{i+\frac{1}{2}} &= p_+^L + p_-^R . \end{aligned} \quad (2.30)$$

With these definitions one can form the following vectors

$$\begin{aligned} R &= a \cdot (\rho_s, \rho u, \rho v, \rho w, \rho e_v, \rho e_e, \rho h)^T , \\ P_{i+\frac{1}{2}} &= (0, \dots, p_{i+\frac{1}{2}} \xi_x, p_{i+\frac{1}{2}} \xi_y, p_{i+\frac{1}{2}} \xi_z, \dots, 0)^T , \end{aligned} \quad (2.31)$$

Omitting for simplicity the j and k indices, the inviscid integrated flux $\hat{E}_{i+\frac{1}{2}}$ at the cell face $i + \frac{1}{2}$ according to the AUSM formulation may be written as:

$$\hat{E}_{i+\frac{1}{2}}^{inv;AUSM} = \left[\frac{1}{2} M_{i+\frac{1}{2}} (R^L + R^R) - \frac{1}{2} |M_{i+\frac{1}{2}}| (-R^L + R^R) \right] S_{i+\frac{1}{2}} + P_{i+\frac{1}{2}} . \quad (2.32)$$

The AUSM numerical inviscid flux can be interpreted as a sum of Mach number weighted average of the left (L) and right (R) state at cell face $i + \frac{1}{2}$ (first term of equation (2.32)) and a scalar dissipative term (second term of equation (2.32)). The dissipative term is a scalar term requiring only $O(n)$ operations compared to $O(n^2)$ operations for a matrix dissipation used by for example the Roe flux difference splitting, since the Roe dissipation term is based on the characteristic decomposition through the eigenvalues of the system.

The Van Leer scheme and the AUSM scheme use the same velocity and pressure splitting, but differ in the convective flux treatment. The Van Leer scheme reads:

$$\hat{E}_{i+\frac{1}{2}}^{inv;VL} = S_{i+\frac{1}{2}} [M_+^L R^L + M_-^R R^R] + P_{i+\frac{1}{2}}, \quad (2.33)$$

and can be recast in a central plus a dissipative part as follows:

$$\hat{E}_{i+\frac{1}{2}}^{inv;VL} = S_{i+\frac{1}{2}} \left[\frac{1}{2} M_{i+\frac{1}{2}} (R^L + R^R) - \frac{1}{2} \phi_{i+\frac{1}{2}}^{VL} (-R^L + R^R) \right] + P_{i+\frac{1}{2}}, \quad (2.34)$$

with

$$\phi_{i+\frac{1}{2}}^{VL} = \begin{cases} |M_{i+\frac{1}{2}}| - 2M_-^R & \text{if } |M_{i+\frac{1}{2}}| \geq 0, \\ |M_{i+\frac{1}{2}}| + 2M_+^L & \text{if } |M_{i+\frac{1}{2}}| < 0. \end{cases} \quad (2.35)$$

The Van Leer and AUSM flux formulations for supersonic flow conditions are identical, but differ in the subsonic flow regime. It can be seen that the Van Leer's flux can be written as the AUSM flux plus a Mach number scaled first order difference of the right and left state:

$$\begin{aligned} \hat{E}_{i+\frac{1}{2}}^{VL} &= \hat{E}_{i+\frac{1}{2}}^{AUSM} - \frac{1}{4} S_{i+\frac{1}{2}} (M^R - 1)^2 [R^R - R^L] \quad 0 \leq M_{i+\frac{1}{2}} < 1, \\ \hat{E}_{i+\frac{1}{2}}^{VL} &= \hat{E}_{i+\frac{1}{2}}^{AUSM} - \frac{1}{4} S_{i+\frac{1}{2}} (M^L + 1)^2 [R^R - R^L] \quad -1 < M_{i+\frac{1}{2}} \leq 0. \end{aligned} \quad (2.36)$$

Since the coefficient of the difference has always the same sign, the second term acts like a dissipative term, and therefore AUSM will be less dissipative than Van Leer's scheme. As can be seen from equation (2.32) the dissipative term tends to zero for vanishing Mach number ($M^L = M^R = M_{i+\frac{1}{2}} \rightarrow 0$). To prevent an undamped scheme the following is done:

$$\hat{E}_{i+\frac{1}{2}}^{inv;AUSM} = S_{i+\frac{1}{2}} \left[\frac{1}{2} M_{i+\frac{1}{2}} (R^L + R^R) - \frac{1}{2} \phi_{i+\frac{1}{2}}^{AUSM} (-R^L + R^R) \right] + P_{i+\frac{1}{2}}, \quad (2.37)$$

with

$$\phi_{i+\frac{1}{2}}^{AUSM} = \begin{cases} \frac{\delta}{2} + \frac{M_{i+\frac{1}{2}}^2}{2\delta} & \text{if } |M_{i+\frac{1}{2}}| \leq \delta \leq 1, \\ |M_{i+\frac{1}{2}}| & \delta < |M_{i+\frac{1}{2}}| \leq 1, \\ |M_+^L| - |M_-^R| & |M_{i+\frac{1}{2}}| \geq 1, \end{cases} \quad (2.38)$$

where δ can be varied between 0 and 1, corresponding to a full Van Leer or full AUSM scheme. In the presented test cases, δ is chosen to be equal to 0.05.

In order to improve another deficiency of AUSM, which creates pressure oscillations around shocks, a hybrid method is constructed where AUSM will be switched to the Van Leer's scheme in regions around shocks through a parameter s , between 0 and 1, to detect shocks. The final flux will be a hybrid of AUSM and Van Leer.

$$\begin{aligned}\hat{E}_{i+\frac{1}{2}}^{hybrid} &= (1-s)\hat{E}_{i+\frac{1}{2}}^{VL} + s\hat{E}_{i+\frac{1}{2}}^{AUSM}, \\ s &= \min \left\{ 1, \max \left\{ \frac{2\Delta_i \nabla_i + \epsilon}{\Delta_i^2 + \nabla_i^2 + \epsilon}, 0 \right\} \right\},\end{aligned}\quad (2.39)$$

in which $\Delta_i = p_{i+1} - p_{i,j,k}$ and $\nabla_i = p_{i,j,k} - p_{i-1,j,k}$. The small parameter ϵ is chosen to be of order 10^{-8} to prevent division by zero in case both Δ_i and ∇_i vanish somewhere in the flowfield.

2.6 Higher order spatial discretization

We now return to the issue of the approximation of the states on either side of the cell interface, i.e. how to develop an improved approximation of Q^L and Q^R . Two methods will be described.

2.6.1 MUSCL extrapolation

The order of accuracy of the spatial discretization is determined by the way the states at the left and the right side of the cell face are calculated. As mentioned previously, a first order accurate scheme is achieved by assuming constant state vectors in each volume:

$$\begin{aligned}\vec{Q}_{i+\frac{1}{2},j,k}^L &= \vec{Q}_{i,j,k}, \\ \vec{Q}_{i+\frac{1}{2},j,k}^R &= \vec{Q}_{i+1,j,k}.\end{aligned}\quad (2.40)$$

First order accuracy is insufficient for practical applications and therefore a higher order interpolation of the states is used according to the Monotone Upwind Schemes for Conservation Laws (MUSCL). The higher order interpolation schemes use a limiter function (Van Albada et al. [1982]), which provides second order accuracy in the smooth part of the flow field and steepens discontinuities without the introduction of non-monotonicity. Instead of the conservative variables Q , the primitive variables W are used in the higher order formulation.

$$\vec{W} = (\rho_s, u, v, w, T_{v_m}, T_e, T)^T. \quad (2.41)$$

The use of primitive variables is computationally less expensive. Some numerical experiments by Dadone and Grossmann [1991] indicate that the use of conservative variables leads to poor convergence behavior and to oscillations in the flow variables near discontinuities.

The interpolation functions in the i -direction read:

$$\begin{aligned} W_{i+\frac{1}{2},j,k}^L &= W_{i,j,k} + \frac{r_{i,j,k}}{4} \{ \Delta_i + \nabla_i \} , \\ W_{i-\frac{1}{2},j,k}^R &= W_{i,j,k} - \frac{r_{i,j,k}}{4} \{ \Delta_i + \nabla_i \} . \end{aligned} \quad (2.42)$$

where $\Delta_i = W_{i+1,j,k} - W_{i,j,k}$ and $\nabla_i = W_{i,j,k} - W_{i-1,j,k}$. The limiter function $r_{i,j,k}$ in i -direction is defined as

$$r_{i,j,k} = \frac{2\Delta_i \nabla_i + \epsilon}{\Delta_i^2 + \nabla_i^2 + \epsilon} , \quad (2.43)$$

in which ϵ is again a small constant ($\epsilon \approx 10^{-8}$), which prevents division by zero and switches off the limiting in regions of near constant flow. Similar functions are applied in the j - and k -directions.

In smooth parts of the flow where $r_{i,j,k} \approx 1$ the MUSCL interpolation reduces to a second order scheme, whereas in regions where $r_{i,j,k} \approx 0$ the scheme reduces to the first order scheme.

2.7 Implicit time integration

To reach the steady state solution, a line-implicit relaxation procedure allowing for large time steps is used. A first order accurate backward time integration of equation (2.13) is given by:

$$\frac{\hat{Q}^{n+1} - \hat{Q}^n}{\Delta t} + \hat{E}_\xi^{n+1} + \hat{F}_\eta^{n+1} + \hat{G}_\zeta^{n+1} = \hat{\Omega}^{n+1} . \quad (2.44)$$

If one assumes that the solution is known at time level n the fluxes of equation (2.44) are approximated by linearization at time level n :

$$\begin{aligned} \hat{E}^{n+1} &\approx \hat{E}^n + \hat{A}^n \Delta \hat{Q} , \\ \hat{F}^{n+1} &\approx \hat{F}^n + \hat{B}^n \Delta \hat{Q} , \\ \hat{G}^{n+1} &\approx \hat{G}^n + \hat{C}^n \Delta \hat{Q} , \\ \hat{\Omega}^{n+1} &\approx \hat{\Omega}^n + \hat{H}^n \Delta \hat{Q} , \end{aligned} \quad (2.45)$$

where \hat{A} , \hat{B} , \hat{C} are the Jacobians of the flux vectors \hat{E} , \hat{F} , \hat{G} , respectively. \hat{H} is the Jacobian of the thermo-chemical source terms Ω , and ΔQ^n is the time variation of the solution:

$$\begin{aligned} \hat{A} &= \frac{\partial \hat{E}}{\partial \hat{Q}} ; \hat{B} = \frac{\partial \hat{F}}{\partial \hat{Q}} ; \hat{C} = \frac{\partial \hat{G}}{\partial \hat{Q}} ; \hat{H} = \frac{\partial \hat{\Omega}}{\partial \hat{Q}} ; \\ \Delta \hat{Q} &= \hat{Q}^{n+1} - \hat{Q}^n . \end{aligned} \quad (2.46)$$

It is preferred to work with primitive variables W , given in the previous section, instead of conservative variables Q . The reason for the linearization with respect to W instead of the

conservative variables is twofold. In hypersonic flows very small densities approaching zero can occur (due to strong expansion), which lead to stiff Jacobians because the reciprocal value of density occurs if Jacobians are derived with respect to \vec{Q} . In addition, since the energies are nonlinear functions of the various temperatures, it is much easier to compute the energies out of the different temperatures.

W and \vec{Q} are related through a transformation matrix:

$$\delta \vec{Q} = \frac{\partial \vec{Q}}{\partial \vec{W}} \delta \vec{W}. \quad (2.47)$$

Therefore the Jacobians derived with respect to the primitive variables are:

$$A = \frac{\partial \hat{E}}{\partial \vec{W}}; B = \frac{\partial \hat{F}}{\partial \vec{W}}; C = \frac{\partial \hat{G}}{\partial \vec{W}}; H = \frac{\partial \hat{\Omega}}{\partial \vec{W}}; \quad (2.48)$$

Combining equations (2.44), (2.45) and (2.47) results in:

$$\left[\frac{\partial \hat{Q}^n}{\partial \vec{W}} \frac{1}{\Delta t} + A^n + B^n + C^n - H^n \right] \Delta \vec{W}^n = -\hat{E}_\xi^n + \hat{F}_\eta^n + \hat{G}_\zeta^n + \hat{\Omega}^n. \quad (2.49)$$

The transformation matrix $\frac{\partial \vec{Q}}{\partial \vec{W}}$ has the form:

$$\begin{bmatrix} 1 & & & & & \\ & \ddots & & & & \\ & & 1 & & & \\ u & \cdots & u & \rho & & \\ v & \cdots & v & & \rho & \\ w & \cdots & w & & & \rho \\ \frac{\partial \rho e_{v_1}}{\partial \rho_1} & \cdots & \frac{\partial \rho e_{v_1}}{\partial \rho_s} & & \frac{\partial \rho e_{v_1}}{\partial T_{v_1}} & \\ \vdots & \vdots & \vdots & & \ddots & \\ \frac{\partial \rho e_{v_m}}{\partial \rho_1} & \cdots & \frac{\partial \rho e_{v_m}}{\partial \rho_s} & & \frac{\partial \rho e_{v_m}}{\partial T_{v_m}} & \\ \frac{\partial \rho e_e}{\partial \rho_1} & \cdots & \frac{\partial \rho e_e}{\partial \rho_s} & \frac{\partial \rho e_e}{\partial T_{v_1}} & \cdots & \frac{\partial \rho e_e}{\partial T_{v_m}} & \frac{\partial \rho e_e}{\partial T_e} & \frac{\partial \rho e_e}{\partial T} \\ \frac{\partial \rho e}{\partial \rho_1} & \cdots & \frac{\partial \rho e}{\partial \rho_s} & \rho u & \rho v & \rho w & \frac{\partial \rho e}{\partial T_{v_1}} & \cdots & \frac{\partial \rho e}{\partial T_{v_m}} & \frac{\partial \rho e}{\partial T_e} & \frac{\partial \rho e}{\partial T} \end{bmatrix} \quad (2.50)$$

The system (2.49) of equations results in a large banded block matrix which needs to be inverted. The band width will depend on the order of the spatial accuracy, the dimensions

of the number of equations and on the dimensions of the grid. Especially for higher order discretizations and three-dimensional flows, the construction of the matrix and the solution of this system of equations requires an enormous amount of CPU time and memory which goes far beyond the capabilities of present computers.

Therefore two simplifications are introduced:

1. the left hand side (LHS) of equation (2.49) is based on first order spatial discretization
2. an iterative line-Gauss-Seidel relaxation is used to solve the system of equations

The line Gauss-Seidel relaxation method will be used, since it will have a faster convergence rate compared to a point Gauss-Seidel or Jacobi method. Since the code deals with highly nonlinear problems, it provides a more stable algorithm. The line Gauss-Seidel relaxation method results in a block tridiagonal system. It can be applied in the i, j or k direction. Application of the line Gauss-Seidel to an i -line and sweeping along diagonal planes in the positive $j-$ and $k-$ direction yields:

$$\begin{aligned} & \left\{ -A_{i-\frac{1}{2},j,k}^+ \right\} \Delta W_{i-1,j,k}^l + \left\{ A_{i+\frac{1}{2},j,k}^- \right\} \Delta W_{i+1,j,k}^l + \\ & \quad \left\{ \left(\frac{1}{\Delta t_{i,j,k}} \frac{\partial \hat{Q}_{i,j,k}}{\partial W_{i,j,k}^l} \right) \right\} \\ & - A_{i-\frac{1}{2},j,k}^- + A_{i+\frac{1}{2},j,k}^+ - B_{i,j-\frac{1}{2},k}^- + B_{i,j+\frac{1}{2},k}^+ - C_{i,j,k-\frac{1}{2}}^- + C_{i,j,k-\frac{1}{2}}^+ - H_{i,j,k} \} \Delta W_{i,j,k}^l = \\ & - \left\{ E_{i+\frac{1}{2},j,k} - E_{i-\frac{1}{2},j,k} + F_{i,j+\frac{1}{2},k} - F_{i,j-\frac{1}{2},k} + G_{i,j,k+\frac{1}{2}} - G_{i,j,k-\frac{1}{2}} \right\} \\ & + \hat{\Omega}_{i,j,k} + \left\{ B_{i,j-\frac{1}{2},k}^+ \right\} \Delta W_{i,j-1,k}^l - \left\{ B_{i,j+\frac{1}{2},k}^- \right\} \Delta W_{i,j+1,k}^{l-1} \\ & + \left\{ C_{i,j,k-\frac{1}{2}}^+ \right\} \Delta W_{i,j,k-1}^l - \left\{ C_{i,j,k-\frac{1}{2}}^- \right\} \Delta W_{i,j,k+1}^{l-1}. \end{aligned} \tag{2.51}$$

The superscript l is a sub-iteration index in the range of $l = 0 \dots m$, with $\Delta \vec{W}^0 = 0$ and $\Delta \vec{W}^n = \Delta \vec{W}^m$.

The Jacobians A, B, C and H are calculated numerically by using one sided differences. The (p, r) component of a Jacobian is:

$$\frac{\partial f_p}{\partial w_r} = \frac{f_p(\vec{W} + \epsilon \vec{e}^r w_r) - f_p(\vec{W})}{\epsilon w_r}, \tag{2.52}$$

where f_p is the p -th component of a flux vector and w_r is the r -th component of the state vector W . Also, ϵ is a small number of order 10^{-8} and \vec{e}^r is the vector:

$$\vec{e}^r = (\delta_{1r}, \dots, \delta_{nr})^T, \tag{2.53}$$

in which δ_{ij} is the Kronecker delta.

The time step is determined as follows:

$$\Delta t_{i,j,k} \leq \frac{\text{CFL} \cdot J^{-1}}{(|\max(u_{i,j,k}, v_{i,j,k}, w_{i,j,k})| + a_{i,j,k}) S_{i,j,k}},$$

where a denotes the speed of sound, CFL is the Courant-Friedrich-Lewis number, J the volume of the cell given by (2.18) and $S_{i,j,k}$ is the maximum of the cell face areas of the control volume i, j, k . Since a fully implicit scheme is unconditionally stable for linear problems, the CFL number could be infinite. However, due to the nonlinearity of the system of equations to be solved, the CFL number is in the range 1-10, in order to provide enough damping in the Newton iteration.

2.8 Boundary conditions

The computational domain is extended with two ghost cells on all boundaries to determine the flux at the cell face. The numerical flux, which is a function of the left and right state vector Q^L and Q^R at the boundary of the domain, is determined by the type of boundary conditions and by the information from the flow field (see Figure 2.2). Depending on the number of characteristics entering the domain, information from the flow field has to be specified in the two ghost cells.

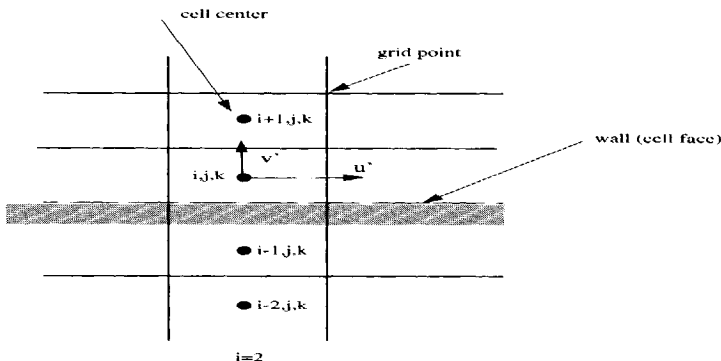


Figure 2.2: Cells near outer bounds of the physical domain.

2.8.1 Supersonic inflow

In case of supersonic inflow, which means that there are no outgoing characteristics, all the primitive variables are specified in the two ghost cells $(i - 1, j, k)$ and $(i - 2, j, k)$

(see Figure 2.2):

$$T, T_{v_m}, \rho_s, u, v, w . \quad (2.54)$$

2.8.2 Subsonic inflow

For subsonic inflow there is one outgoing characteristic. This means that the information of one variable has to come from the flow field. In case for a subsonic nozzle inflow, it is assumed that the flow at the reservoir is in thermal-chemical equilibrium and the pressure and density are specified at the inlet. The mass fractions are determined according to the equilibrium values. The velocity is taken from the flow field. Assuming an equilibrium isentropic inlet flow, a prescribed total temperature T_0 , total pressure P_0 and the flow direction such that $v = w = 0$, the static variables can be derived:

$$\begin{aligned} T &= T_0 \left(1 + \frac{\gamma-1}{2} M^2\right)^{-1} , \\ p &= P_0 \left(1 + \frac{\gamma-1}{2} M^2\right)^{\frac{-\gamma}{\gamma-1}} , \\ \rho &= \frac{p}{\sum_s c_s R_s T} , \end{aligned} \quad (2.55)$$

where M is the Mach number of the interior point. The first ghost cell is now prescribed and the second is copied.

2.8.3 Slip boundary or plane of symmetry

At solid boundaries, a condition of zero mass flux through the boundary is obtained by setting the appropriate values in the two ghost cells. The tangential velocities are set to equal values, and the normal velocities are equal with an opposite sign. The temperatures and the densities in the ghost cells are set to have a zero pressure gradient at the wall. Omitting the indices j, k for simplicity, one gets:

$$\begin{aligned} \rho_{s;i-1} &= \rho_{s;i} , \\ u'_{i-1} &= -u'_i , \\ v'_{i-1} &= v'_i , \\ w'_{i-1} &= w'_i , \\ T_{i-1} &= T , \\ T_{v_m;i-1} &= T_{v_m;i} , \\ T_{e;i-1} &= T_{e;i} , \end{aligned} \quad (2.56)$$

where u', v', w' denote the velocities normal and tangential to the relevant surface, respectively. The values in the second ghost cell $i - 2$ are similarly prescribed as in equation (2.56), but the information comes from the point $i + 1$.

2.8.4 Viscous (no slip) condition, with non- or catalytic wall, isothermal or adiabatic

For viscous flows no-slip conditions are applied to the wall by imposing appropriate values in the ghost cells. The tangential and normal velocities in the ghost cells are mirrored with respect to the wall. For a non-catalytic wall a zero gradient is applied for the species mass fraction. For a catalytic wall the mass fractions are specified in equilibrium at the given wall temperature. The wall temperature can be adiabatic (zero gradient of temperature) or in case of an isothermal wall, the translational, vibrational and electrical temperatures are fixed at the same wall temperature. The density is calculated in the ghost cells in such a way that the pressure gradient normal to the wall is zero.

$$\begin{aligned} u_{i-1} &= -u_i, \\ v_{i-1} &= -v_i, \\ w_{i-1} &= -w_i, \\ c_{s;i-1} &= \begin{cases} c_{s;i} & \text{non-catalytic wall conditions;} \\ 2c_{s:wall} - c_{s;i} & \text{catalytic wall conditions;} \end{cases} \\ T_{i-1} &= \begin{cases} T_i & \text{adiabatic conditions;} \\ 2T_{wall} - T_i & \text{fixed-wall conditions;} \end{cases} \\ T_{v_m;i-1} &= \begin{cases} T_{v_m;i} & \text{adiabatic conditions;} \\ 2T_{wall} - T_{v_m;i} & \text{fixed-wall conditions;} \end{cases} \\ T_{e;i-1} &= \begin{cases} T_{e;i} & \text{adiabatic conditions;} \\ 2T_{wall} - T_{e;i} & \text{fixed-wall conditions;} \end{cases} \end{aligned} \quad (2.57)$$

The values in the second ghost cell ($i - 2$) are linearly extrapolated and the velocities are mirrored from the wall.

2.8.4.1 Partial catalytic wall condition

The physical model is outlined in Appendix B. Implementation of this boundary condition starts from writing the equations in terms of node-variables. The points in the computational grid are indicated for a two-dimensional grid by two indices i and j (see Figure 2.3). The boundary condition is then applied between the wall points and the first points in the gas phase. We will mark the former with the subscript w and the latter with the subscript g , see Figure 2.3. Δn represents the distance between wall and first row of points in the gas.

The discretized form of the catalytic boundary condition (B.6) for each species s of the total species ns yields:

$$\dot{w}_{s,w} = \rho_w D_{s,w} \left(\frac{c_{s,g} - c_{s,w}}{\Delta n} \right), \quad (2.58)$$

where the quantity between brackets is an approximation to the wall gradient for the mass

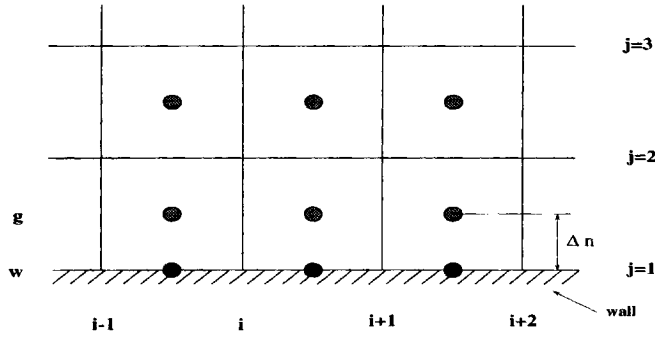


Figure 2.3: Example of discretization near a boundary surface.

fraction of the species s .

If we label the new time step with the superscript $n + 1$, equation (2.58) reads:

$$\dot{w}_{s,w}^{n+1} = \left[\rho_w D_{s,w} \left(\frac{c_{s,g} - c_{s,w}}{\Delta n} \right) \right]^{n+1}. \quad (2.59)$$

From this last equation we can obtain the species mass fractions on the wall:

$$c_{s,w}^{n+1} = c_{s,g}^{n+1} - \dot{w}_{s,w}^{n+1} \cdot \left(\frac{\Delta n}{\rho_w D_{s,w}} \right)^{n+1}. \quad (2.60)$$

Relation (2.60) is implicit because $\dot{w}_{s,w}^{n+1}$ is also a function of $c_{s,w}^{n+1}$. To overcome this, the term $\dot{w}_{s,w}$ is linearized as follows:

$$\dot{w}_{s,w}^{n+1} = \dot{w}_{s,w}^n + \sum_{j=1}^{ns} \left(\frac{\partial \dot{w}_{s,w}}{\partial c_{j,w}} \right)^n (c_{j,w}^{n+1} - c_{j,w}^n), \quad (2.61)$$

Using equation (2.61) and (2.60) this reads:

$$\begin{aligned} c_{s,w}^{n+1} &+ \frac{\Delta n}{(\rho_w D_{s,w})^{n+1}} \sum_{j=1}^{ns} \left(\frac{\partial \dot{w}_{s,w}}{\partial c_{j,w}} \right)^n \cdot c_{j,w}^{n+1} = \\ &= c_{s,g}^{n+1} - \frac{\Delta n}{(\rho_w D_{s,w})^{n+1}} \cdot \left[\dot{w}_{s,w}^n - \sum_{j=1}^{ns} \left(\frac{\partial \dot{w}_{s,w}}{\partial c_{j,w}} \right)^n \cdot c_{j,w}^n \right]. \end{aligned} \quad (2.62)$$

Now extracting $c_{s,w}^{n+1}$, the previous equation reads:

$$\begin{aligned} c_{s,w}^{n+1} = & \left\{ c_{s,g}^{n+1} - \frac{\Delta n}{(\rho_w D_{s,w})^{n+1}} \right. \\ & \cdot \left[\dot{w}_{s,w}^n - \sum_{j=1}^{ns} \left(\frac{\partial \dot{w}_{s,w}}{\partial c_{j,w}} \right)^n \cdot c_{j,w}^n + \sum_{j \neq s, j=1}^{ns} \left(\frac{\partial \dot{w}_{s,w}}{\partial c_{j,w}} \right)^n \cdot c_{j,w}^{n+1} \right] \Bigg\} \\ & \cdot \left[1 + \frac{\Delta n}{(\rho_w D_{s,w})^{n+1}} \left(\frac{\partial \dot{w}_{s,w}}{\partial c_{s,w}} \right)^n \right]^{-1} \end{aligned} \quad (2.63)$$

The next step is the insertion of the source terms in equation (2.63). The most general approach should consider the presence of 2 different recombination coefficients:

- γ_{OO} : probability for O atoms which recombine as O_2
- γ_{NN} : probability for N atoms which recombine as N_2

We shall treat in detail only the case for atomic oxygen. For atomic nitrogen similar expressions can be derived. The O source term $\dot{w}_{O,w}$ reads:

$$\dot{w}_{O,w} = \rho_w c_{O,w} \gamma_{OO} \sqrt{\frac{kT_w}{2\pi m_O}} . \quad (2.64)$$

Writing equation (2.63) for O and using the last two expressions, we obtain the final expression for the mass fraction of atomic oxygen on the wall:

$$c_{O,w}^{n+1} = c_{O,g}^{n+1} \cdot \left\{ 1 + \frac{\left[\rho_w \gamma_{OO} \sqrt{\frac{kT_w}{2\pi m_O}} \right]^n}{(\rho_w D_{O,w})^{n+1}} \cdot \Delta n \right\}^{-1} . \quad (2.65)$$

For atomic nitrogen the expression is similar:

$$c_{N,w}^{n+1} = c_{N,g}^{n+1} \cdot \left\{ 1 + \frac{\left[\rho_w \gamma_{NN} \sqrt{\frac{kT_w}{2\pi m_N}} \right]^n}{(\rho_w D_{N,w})^{n+1}} \cdot \Delta n \right\}^{-1} . \quad (2.66)$$

For O_2 and N_2 we have:

$$c_{O_2,w}^{n+1} = c_{O_2,g}^{n+1} + c_{O,w}^{n+1} \cdot \frac{\left[\rho_w \gamma_{OO} \sqrt{\frac{kT_w}{2\pi m_O}} \right]^n}{(\rho_w D_{O_2,w})^{n+1}} \cdot \Delta n , \quad (2.67)$$

$$c_{N_2,w}^{n+1} = c_{N_2,g}^{n+1} + c_{N,w}^{n+1} \cdot \frac{\left[\rho_w \gamma_{NN} \sqrt{\frac{k T_w}{2\pi m_N}} \right]^n}{(\rho_w D_{N_2,w})^{n+1}} \cdot \Delta n . \quad (2.68)$$

Since no catalycity coefficient for NO is given by the Stewart model, NO is assumed to be non-catalytic.

2.9 Selection of a numerical flux function

Depending on the number of species incorporated in the description of the reacting gas mixture, the governing system to be solved may be quite large. The selection of a proper flux function will therefore be a trade-off between accuracy and efficiency in terms of speed and memory requirements. As has already been noted in the preceding section, Roe's method requires $O(n^2)$ operations to stabilize the scheme compared to $O(n)$ for the Van Leer and the AUSM scheme. Furthermore it has been demonstrated that the Van Leer scheme will be more diffusive than AUSM.

In order to demonstrate the difference in dissipation of the various schemes and the influence on grid alignment, an inviscid flow with a shear layer (Mach 0.1 below and 0.5 above) has been computed. The computations have been performed on two grids: one with a shear layer parallel to the horizontal grid lines and one with a shear layer with an angle of 45° to the grid lines (see Figure 2.4).

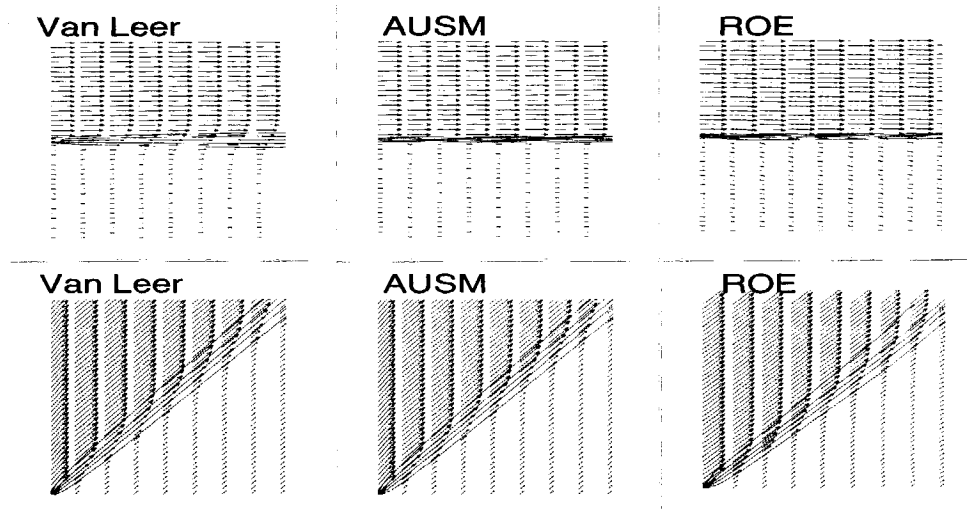


Figure 2.4: Subsonic slip line spreading for different schemes.

In the aligned shear layer it is clear that the Van Leer's dissipation broadens the shear layer compared to Roe and AUSM as is to be expected from (2.35) and (2.36), since both flow regimes are subsonic. Therefore Roe and AUSM should behave very accurately in aligned boundary layers in comparison to Van Leer's. However, if the grid is not aligned with the shear layer, all schemes exhibit a similar behavior. Thus if the complexity of the flow is increased, only a certain accuracy can be achieved, which is very similar for all schemes.

The AUSM and the Roe schemes have a similar behavior, but as mentioned earlier AUSM uses a scalar dissipation which is quite cheap in terms of computational costs compared to the matrix dissipation of the Roe scheme. In addition, for nonequilibrium flows the computation of the eigenvalues and eigenvectors becomes expensive. Therefore AUSM is preferred because of its simplicity and adaptability to nonequilibrium phenomena.

Since this shear layer test case is still far from a realistic test case, the numerical flux functions previously proposed are compared computationally using three selected test cases characterized by two-dimensional flow fields:

1. a subsonic flat plate;
2. a supersonic flat plate with an oblique shock-boundary layer interaction, as described by Hakkinen et al. [1959];
3. a cold hypersonic ramp, as described by Abgrall et al. [1991].

In order to highlight the influence of the numerical approaches on the prediction of the flow features for each test case, the comparison of the solutions obtained on a predefined computational mesh is shown. In the following cases we will also look at the effect of increasing the order of the interpolated values at the cell faces by comparing ENO (Essentially Non Oscillatory) interpolation and MUSCL extrapolation. Whereas the selection of the numerical flux function achieves better accuracy of especially viscous multidimensional flows, ENO reduces the numerical dissipation by the increase of the spatial discretization order, higher than the MUSCL extrapolation. This can only be realized if the stencil consists of points located in a smooth region of the local flow field. Therefore the idea of ENO is to adapt the stencil to the current flow field solution, trying to keep it in a smooth area, without reducing the order of interpolation. [Osher and Charkravarthy 1984; Shu and Osher 1988]. In this investigation only the Van Leer scheme is used together with ENO, because of its robustness and favorable convergence properties. Interpolation has been performed using primitive variables.

2.9.1 Flat plate

A more realistic test case than the shear layer test case in Section 2.9 to compare the different flux functions is a subsonic flow over an one meter long flat plate. The mesh, with a distribution of 100 points along the flat plate and 60 points perpendicular to the wall, has been selected for the comparison of the solutions. To achieve an accurate resolution of the flow a clustering of points in the stagnation region of the plate has been considered necessary. Furthermore, for an acceptable prediction of the boundary layer features, a normal cell spacing

of 10^{-5} m at the wall has been chosen. Table 2.1 shows the freestream and wall conditions considered for the test case.

Gas	γ	$Re_{L=1m}$	M	Wall
ambient air	1.4	$19 \cdot 10^3$	0.34	adiabatic

Table 2.1: Flat plate test case conditions.

Figure 2.5 shows the comparison of the skin friction distributions over the flat plate obtained by applying the different numerical flux functions. Since in this figure the differences are difficult to judge, the differences of the numerically obtained skin frictions with the Blasius solution are shown in Figure 2.6, and defined as $\text{error} = \left| \frac{C_f, \text{scheme} - C_f, \text{Bl}}{C_f, \text{Bl}} \right|$.

It is clear from the figure that the AUSM scheme provides better solutions than the Van Leer scheme, consistently with what was found in the shear layer test case previously shown. In addition, the ENO approach slightly improves the Van Leer solution, but does not provide a better solution compared to AUSM. Furthermore, increasing the ENO discretization order from second to third order results in the formation of oscillations, leading to a deteriorated solution. As a consequence, the ENO solution shows a decrease of convergence rate by increasing the discretization order.

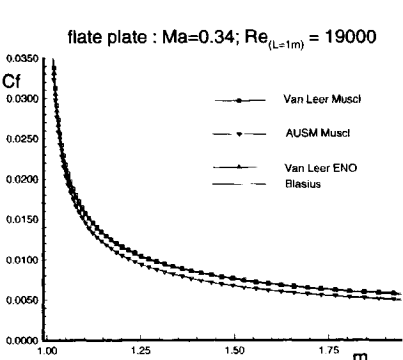


Figure 2.5: Skin friction on a flat plate.

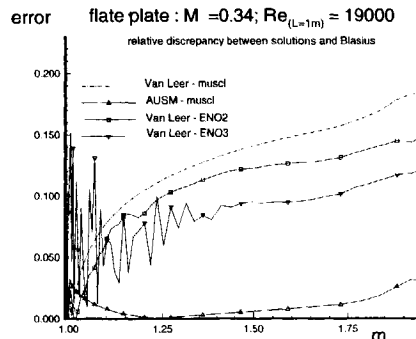


Figure 2.6: Discrepancy of the schemes with Blasius.

2.9.2 Hakkinen experiment

To increase the complexity of the test case, an experiment of Hakkinen et al. [1959] is simulated. An oblique shock wave is impinging on a laminar boundary layer which locally separates. The freestream and wall conditions are listed in Table 2.2.

Gas	γ	Re_L	M	Wall
ambient air	1.4	$2.96 \cdot 10^5$	2.0	adiabatic

Table 2.2: Hakkinen test case conditions.

Re_L is the Reynolds number at the position of the flat plate, where inviscid theory predicts impingement of the oblique shock. The experiment was performed in a continuous running wind tunnel and the wall is assumed to be adiabatic.

The grid, shown in Figure 2.7, contains 100 points in streamwise direction and 80 points normal to the wall. It is strongly refined in the boundary layer and perpendicular to the boundary layer in vicinity of the stagnation region of the plate and in the interaction region, leading to rather poor resolution in the inviscid parts of the flow field. In Figure 2.8 the computed and the measured skin friction are plotted. A Blasius solution, corrected for compressibility due to the Mach 2 flow, is also plotted. The separation bubble is smallest for Van Leer followed by ENO and then AUSM, demonstrating the dissipative behavior of the schemes. Second order ENO oscillates in the re-attachment region. AUSM produces a bubble bigger than the measured one. However, if three-dimensional effects are present in a two-dimensional experiment, this usually results in a reduced measured separation length. For all computations, the skin friction at the reattachment is $\pm 15\%$ lower than the experimental data, probably due to a non-laminar reattachment.

This leads to the conclusion that if one increases the complexity of an experiment, the experiment is more difficult to judge and secondly consistent with the shear layer example, that if the grid is not aligned with the flow the differences between the schemes become smaller. Since AUSM produces the largest recirculation zone, even larger than experiment with possibly three-dimensional effects and possibly turbulent reattachment, AUSM yields a better solution than the oscillatory ENO solution and Van Leer solution with smaller recirculation zone.

2.9.3 Holden ramp experiment

The next viscous two-dimensional perfect gas test case is a cold hypersonic laminar flow past a 15° ramp. (Case III.4 of the Antibes workshop [Abgrall et al. 1991]). Table 2.3 shows the freestream and wall conditions considered.

The grid contains 120x80 grid points and is clustered in the boundary layer, the stagnation

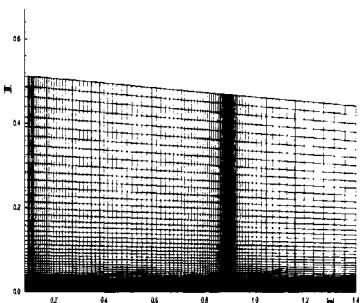


Figure 2.7: Mesh (100x80 grid points) used for the Hakkinen experiment.

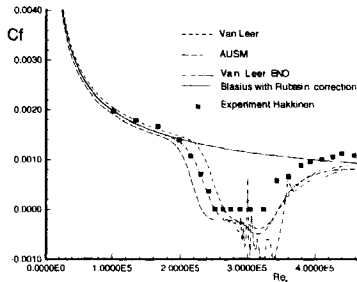


Figure 2.8: Skin friction of the Hakkinen experiment.

Gas	γ	Re_{Hinge}	M	Wall
air, $T_\infty = 64.6$ K	1.4	$2.47 \cdot 10^5$	11.68	$T_{wall} = 297.2$ K

Table 2.3: Test case of the Holden ramp experiment.

and the hinge zone. For this grid the difference between AUSM, Van Leer and ENO is small, except for the fact that the second order ENO scheme close to the reattachment is oscillatory. Higher order ENO discretization was not possible, because the oscillations deteriorate the solution too much. The measured skin friction from the experiment performed by Holden [1978] is plotted, see Figure 2.10. The Mach isolines are plotted in Figure 2.9. The boundary layer growth on the flat plate, the separation bubble, the induced separation shock and reattachment shock are visible. As in the Hakkinen case - and any two-dimensional test case - the experiment could contain three-dimensional effects, decreasing the bubble size in the experiment. Again AUSM produced the largest separation zone, followed by the second order ENO-Van Leer approach. The smallest separation zone is computed with the most dissipative scheme of Van Leer-MUSCL.

2.10 Conclusions

In this chapter the equations to solve a hypersonic nonequilibrium flow field have been described. We have constructed a numerical procedure to solve these equations and selected a modified AUSM flux function with a MUSCL extrapolation to be used in the 1 calculations to be described in the following chapters. This selection was based on the compromise between

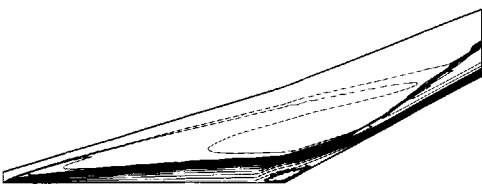


Figure 2.9: Holden test case : Mach isolines.

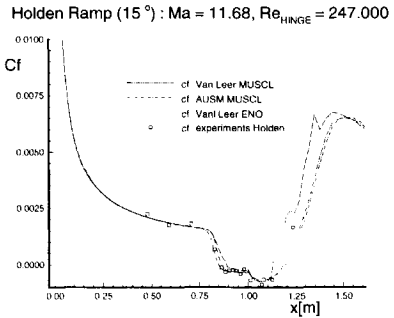


Figure 2.10: Skin friction of the Holden ramp experiment.

ease of implementation of the thermal and chemical nonequilibrium models in the flow solver and low CPU costs compared to FDS methods and accuracy.

Before this solver can be used in the assessment of hypersonic flow fields, one needs to know whether the numerical scheme actually solves the physical model at hand (verification) and whether these models and their numerical approximation exhibit the physical features encountered in experiments. These requirements will be addressed in the next chapter.



3

Verification and validation

In the scope of CFD, there are many state-of-the-art numerical schemes that are able to solve the Navier-Stokes equations. In general, each of these schemes has advantages and disadvantages in terms of numerical accuracy, robustness and stability. Likewise, there are many state-of-the-art physical models that can approximate the chemical processes in high temperature gas dynamics. Each model has its limitations in application. For the code, solving the partial differential equations, it has to be *verified* that the equations are solved correctly and it produces a consistent solution with mesh refinement. Whether the numerical solution bears any relation to a physical solution is the subject of *Validation*.

In order to validate the solver, we will simulate wind tunnel experiments and a flight experiments with its corresponding input data. While performing these calculations, we will verify whether the code produces mesh convergent solutions. The choice of the test cases must obviously be representative of typical physics encountered in the hypersonic flow regime.

The validity of the input data, such as freestream conditions in flight and from wind tunnels, or conditions needed to prescribe the catalycity of the surface of the test cases, is not pursued here. Usually for flight experiments standard atmosphere tables, such as the US Standard Atmosphere [1976] and the CIRA model [Keating 1996], are used to prescribe the freestream conditions. These tables are based on flight measurements as well as numerical interpolation which could introduce an uncertainty of 5 to 10%. Above 50 km altitude the different tables available from literature start to differ more so that Mach and Reynolds numbers can vary significantly which may influence the results. Similarly for hypersonic wind tunnels not all necessary conditions in the test section are measured. The static values such as temperature, pressure and mass fractions are calculated and can give rise to uncertainties in the conditions necessary to calculate a test case in the wind tunnel, even if the accuracy is known from the heat flux or pressure measurement. In addition it is difficult from literature to assess the quality of the measurements due to a lack of information concerning the accuracy of the available experimental flight as well as the wind tunnel data. It is the author's believe that no better estimates as provided by literature can be made, and therefore these inputs values will be taken as nominal.

Since validation of a code is restricted especially in the hypersonic regime, one can only validate the capability of the code to current available experimental data from literature. On the other hand, where possible, other numerical data is used for comparison, to assess the sensitivity of the results of different solvers to simulate hypersonic flows.

The software for this thesis was developed to study hypersonic flows around re-entry vehicles. The numerical scheme selected in Chapter 2 will be validated by comparing CFD predictions with available experimental data in cold hypersonic conditions in which no thermal excitation or chemistry takes place. Similarly, we choose hot hypersonic conditions for validation of the thermo-chemistry models employed in LORE. In this way we can validate the physical models individually.

The following test cases have been selected being typical for the physics of hypersonic flow regime. They range from perfect gas (cold) to thermo-chemical nonequilibrium ionized gas in hypersonic flow regime (hot). Moreover, all test cases have been selected such that the uncertainty resulting from turbulence is avoided in this validation exercise by selecting laminar flow conditions.

- Hollow Cylinder Flare wind tunnel experiment (cold)
- Hyperboloid Flare wind tunnel experiment (moderately hot)
- RAM C-II flight probe (hot)

In addition, since the first two test cases have been studied in hypersonic workshops for numerical tool validation, a comparison with the numerical results obtained by other authors is also provided.

3.1 Hollow cylinder flare test case

3.1.1 Introduction

This test case was proposed for the validation of Navier-Stokes solvers in the field of perfect gas high speed flows characterizing strong shock-wave boundary layer interaction in fully laminar regime over an axisymmetric configuration that produces a large separated region. This test case was designed to avoid uncertainties caused by transition and the associated turbulence modeling. It also avoids three-dimensional effects that affect two-dimensional ramp-plate experiments. The experiment was carried out in the R5Ch blow down hypersonic wind tunnel of ONERA at Chalais-Meudon, France. A description of the wind tunnel is given by Chanetz et al. [1992].

In this section the numerical results will be compared with experiments as well as numerical results obtained by other researchers. Grid convergence is achieved to get a mesh independent separation length prediction.

3.1.2 Experimental test case

This experiment, carried out in the R5Ch hypersonic blow down wind tunnel, is described in Chanetz [1995]. Experimental surface pressures, heat flux data and density profiles are taken from Bonnet et al. [1996]. A sketch of the geometry of the model is depicted in Figure 3.1. The model consists of a hollow cylinder with an external diameter of 65 mm and an internal diameter of 45 mm. A flare at an angle of 30 degrees is located 101.7 mm downstream of the sharp leading edge, the flare is followed by a cylindrical part having an outer diameter of 115 mm and a length of 25 mm to ensure a supersonic flow at the end of the model.

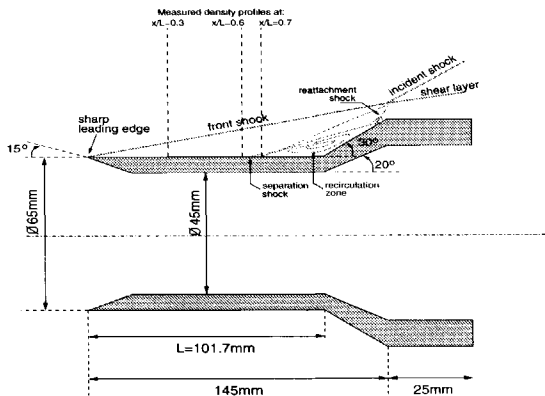


Figure 3.1: Hollow cylinder flare geometry.

From oil flow visualization and testing with small angle of attack and/or yaw, it was verified that the model was inclined at zero degrees angle of attack with an uncertainty of 10 minutes. The uncertainty for pressure and heat flux measurement is maximum 5% and 10%, respectively [Chanetz 1995]. The selected flow conditions are assumed under the nominal stagnation conditions with a total pressure of 2.5 bar and total temperature of 1050 K. The static pressure and static temperature in the test section are not measured directly. They are deduced from the total pressure in the test section, the stagnation pressure and the stagnation temperature, measured during the run. The ratio of total and static pressure yields the Mach number which in turn allows for the determination of other quantities. The precision of the 3 parameters measured during the run leads to a uncertainty for the Mach number of 5 % and for the Reynolds number of 2% [Chanetz et al. 1990]. The resulting freestream condition are given in Table 3.1.

$L[mm]$	101.7	$P[Pa]$	6.3
Re_L	18916	$T[K]$	51
M	9.91	$T_{wall}[K]$	293

Table 3.1: Freestream conditions of R5Ch, taken as freestream conditions for the hollow cylinder flare computations.

3.1.3 Numerical results

A grid convergence study was conducted on four meshes, each time doubling the number of points in each direction. The size Δ of the smallest distance normal to the wall is given in Table 3.2. The coarsest computational mesh (74×50 cells) is shown in Figure 3.2. The mesh has been divided into 4 blocks such that the computation could run on 4 processors. The grid points have been clustered at the leading edge of the cylinder and near the hinge line. As a general numerical procedure, the solution obtained on the coarse mesh is interpolated on a refined mesh.

grid cells	$\Delta[mm]$
74×50	$.1 \cdot 10^{-2}$
148×100	$.5 \cdot 10^{-3}$
296×200	$.25 \cdot 10^{-3}$
592×400	$.125 \cdot 10^{-3}$

Table 3.2: Grids used for hollow cylinder flare computations.

The convergence histories in terms of L^2 norm of the density updates versus the number of iterations obtained on the four meshes are shown in Figure 3.3. Here it is shown that the

code converges for all meshes. In addition, it was verified for each mesh that the wall values, such as skin friction and wall pressure, converge with increasing number of iterations. Grid convergence results in terms of pressure coefficient, skin friction coefficient are presented in Figures 3.4 and 3.5. Even though the above mentioned values agree on the cylindrical part for each mesh, the separation length still increases with the doubling of the cells up to the finest mesh where it does not change anymore compared to one coarser level.

The pressure along the wall represents the typical shock-wave boundary layer interaction on a ramp configuration in supersonic/hypersonic flow, which can be seen also in the schematic drawing of the flow phenomena in Figure 3.1. The pressure drops from the stagnation point until it reaches a separation shock, formed by the presence of the recirculation zone. Behind this shock the pressure is increased to a more or less constant plateau. A re-attachment shock is formed due to compression waves near the end of the flare where the separated region ends. The pressure increases again up to the point where the flare ends and the flow expands.

A comparison in Figures 3.6 and 3.7 in terms of pressure coefficient and Stanton number is made both with experimental and numerical data from the HSFF database (First Europe-US High Speed Flow Field database) [Grasso and Marini 1997]. As can be seen, the pressure coefficients from all numerical simulations on the cylindrical part differ by 40% with the experimental values. This difference can only be seen in log scale, since the pressure is low on the cylinder compared to the rest on the model. This difference was never noticed since many people plotted the pressure coefficients on a linear scale. A possible explanation is that these low pressures are not measured correctly or that the freestream values are not correct. The latter seems to be unlikely since the numerical heat fluxes agree better with the experimental values. The difference between the wall pressures obtained by different codes is smaller than 2-3%, except near the separation and re-attachment point which is predicted within a 5mm range. The computation yields the largest bubble size.

The Stanton numbers differ less than 2-5% compared to the other numerical and experimental results. One can see that there are some minor differences in the prediction of the separation point, in which computations predict a slightly more upstream separation point.

Density profiles have been measured by X-ray detection at three streamwise sections at $x/l=.3$, $x/l=.6$ and $x/l=.76$ (Figures 3.8 - 3.10). All are located upstream of the separation point as can be seen in the sketch in Figure 3.1. Even though the experimental uncertainty is not known and the freestream normalized density is not one for some experimental points, the computed shock position, originating from the leading edge, compares within 1 mm of accuracy at all three x -locations with both experimental and other numerical data. The error of the density values inside the boundary layer with respect to the other numerical data except of the DSMC calculation of NASA is smaller than the deviation of the experimental values.

From the comparison of the numerically obtained skin frictions in Figure 3.11, the maximum difference of the location of the separation point of the numerical solutions is smaller than 4 mm, whereas the re-attachment point is predicted within 2 mm. Since the re-attachment point occurs very close to the end of the flare, the question is whether the re-attachment is

influenced by the expansion at the end of the flare.

Therefore an additional computation has been performed in which the flare has been extended as can be seen in Figure 3.12. The skin friction and pressure coefficient are plotted in Figures 3.13 and 3.14 where it is shown that the results are grid convergent. The values obtained from the grid converged solution are compared to the configuration with and without extended flare in Figures 3.15 and 3.16. As can be seen the re-attachment point moves downstream, and the separation point moves upstream.

3.1.4 Conclusion

The numerical method is capable of computing a hypersonic perfect gas over the axisymmetric hollow cylinder model. It has been shown that the code converges with mesh refinement. The discrepancy of pressure coefficient and skin friction distributions of the results with other numerical data and experimental data are found to be below 5%. These small differences can be attributed to the definition of the freestream conditions and/or measurement uncertainty.

Finally, it is shown that by comparing all the numerical data, the spread of the location of the separation point is larger than the spread of the reattachment point. The reason of the smaller spread for the re-attachment can be attributed to the too short flare design, fixing the re-attachment point.

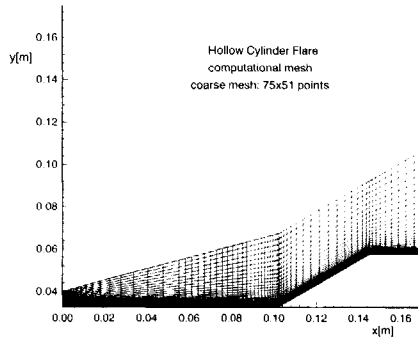


Figure 3.2: Hollow cylinder flare computational mesh.

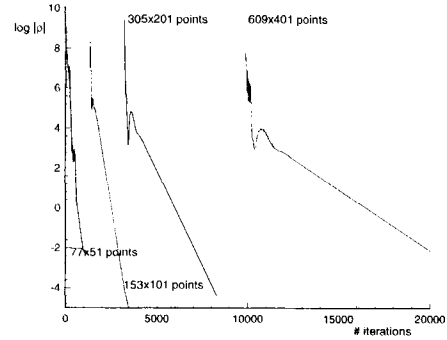


Figure 3.3: Convergence history on sequentially finer grids.

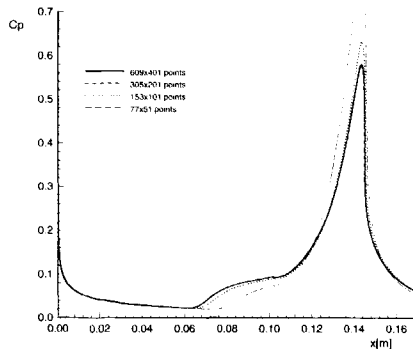


Figure 3.4: Grid convergence for pressure coefficient.

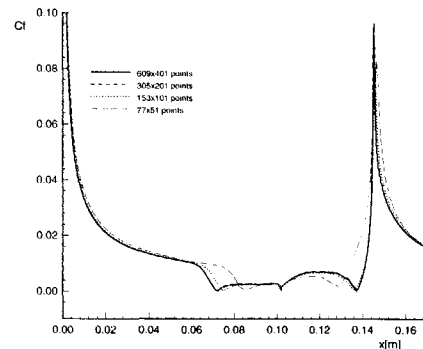


Figure 3.5: Grid convergence for absolute value of skin friction coefficient.

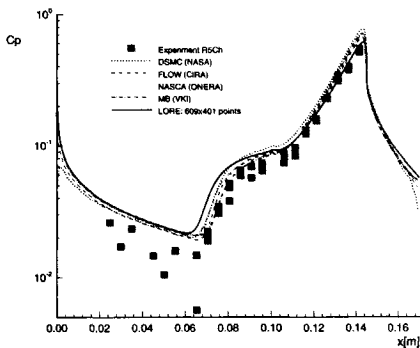


Figure 3.6: Pressure coefficient on hollow cylinder flare model.

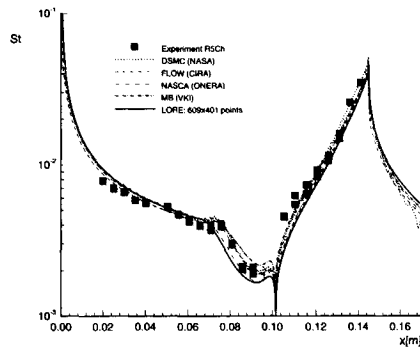


Figure 3.7: Stanton number on hollow cylinder flare model.

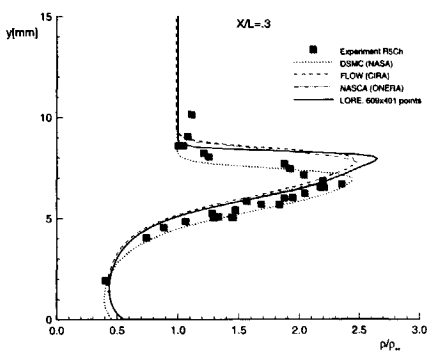


Figure 3.8: Density profile at position $x/L = .3$

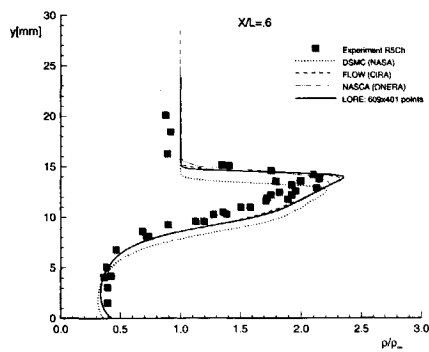
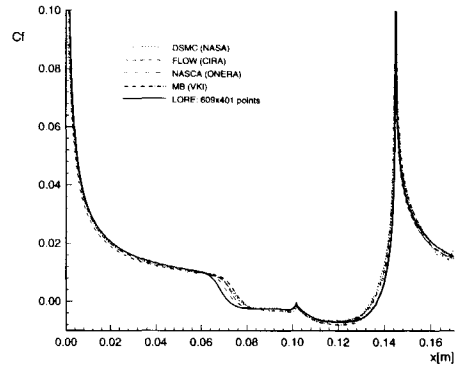
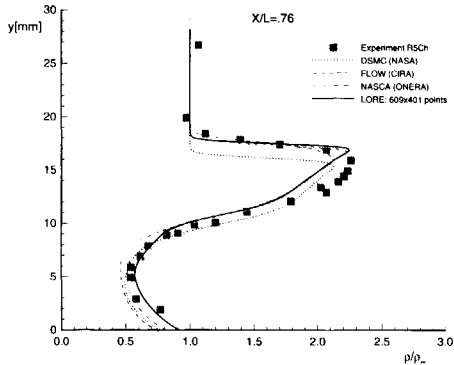
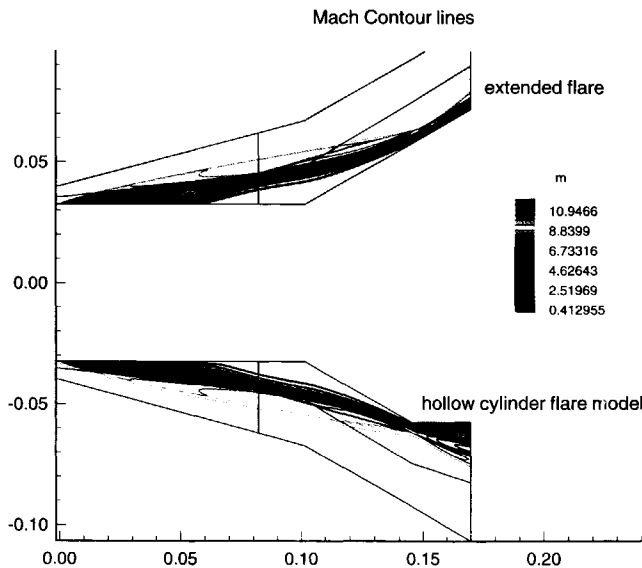


Figure 3.9: Density profile at position $x/L = .6$

**Figure 3.10:** Density profile at position $x/L=0.76$ **Figure 3.11:** Skin friction comparison on hollow cylinder flare model.**Figure 3.12:** Influence of extended flare on the wind tunnel model.

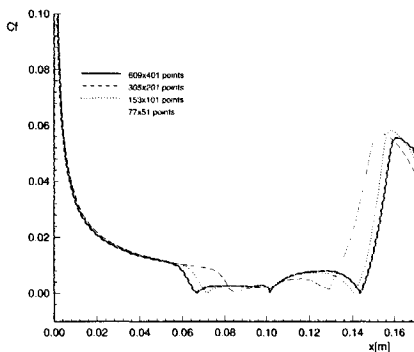


Figure 3.13: Grid convergence for the skin friction on the modified geometry.

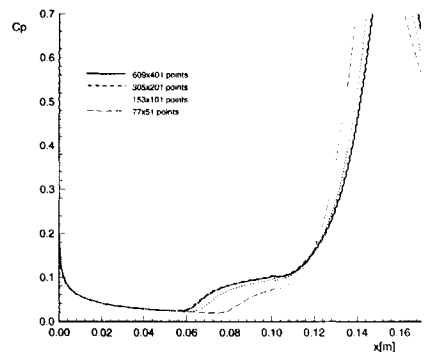


Figure 3.14: Grid convergence for the pressure coefficient on the modified geometry.

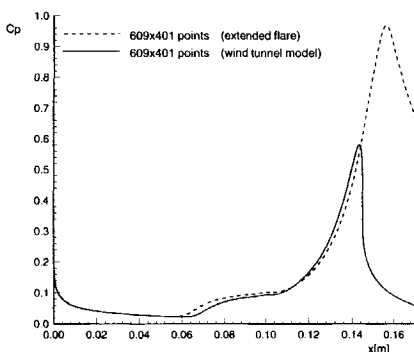


Figure 3.15: Comparison of pressure coefficient between modified and original geometry.

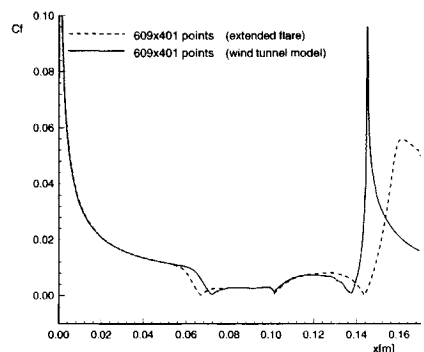


Figure 3.16: Comparison of skin friction between original and modified geometry.

3.2 Hyperboloid-flare in F4

In the previous section we have shown that the tool LORE predicts a hypersonic perfect gas flow within experimental uncertainties. Since the interaction between the different thermo-chemical models is quite complex, the next step is to validate the behavior of a thermally excited, but chemically still frozen gas. In this case the temperature is increased in the shock layer compared to the previous case. But due to the small and slender model, hardly any dissociation should occur.

3.2.1 Introduction

The hyperboloid-flare is an axisymmetric configuration which contour is described by the centerline of the Hermes windward shape. The concept of an “equivalent axisymmetric body” was first proposed by Adams et al. [1977] who showed that an appropriate axisymmetric body at zero degree angle of attack could model the windward-centerline flow field over the Shuttle at a given angle of attack. The results of their investigation demonstrated good agreement between experimental heat transfer data on the windward side of the shuttle at 30 degrees angle of attack and computed heating rates on a 30 degree half angle hyperboloid. This concept was further extended to include an axisymmetric flare to study the physical phenomenon associated with flap efficiency and flap heating [Durand 1992].

For the present configuration the forward part is not a hyperboloid but the Hermes windward centerline at 30 degrees angle of attack with 20 degrees deflected body flap, nevertheless the name “hyperboloid-flare” was kept in the literature for unknown reasons. A curve fit of the geometry is given in Schwane and Muylaert [1992].

In this section the hyperboloid-flare test cases of EHVDB Workshops (European Hypervelocity Database) held at ESTEC 1994 and 1996 have been computed with LORE and compared with experimental and other numerical results. The experiments were carried out in the ONERA F4 facility, see also Appendix C.1

3.2.2 Experimental test cases

For the EHVDB workshop 1994 test case, the freestream conditions in the F4 were determined from the total pressure and enthalpy assuming an inviscid non-equilibrium flow field with an Edenfield [1968] boundary layer correction. However in 1996, after testing with a sharp and blunt cone, the measured pressure levels on the models as well on the wind tunnel wall fitted best with numerical calculations assuming that the boundary layer of the nozzle is laminar and the flow field in equilibrium. Therefore, the freestream conditions as prescribed by the EHVDB Workshop 1996 were calculated with the above assumptions. The inflow conditions are given in Table 3.3. The experimental data correspond to a total pressure of 240 bar and a total enthalpy of 13.7 MJ/kg. One has to note that the total conditions of the experimental data provided for the 1996 Workshop are different from the total conditions

	Workshop '94	Workshop '96
freestream	nonequilibrium	equilibrium
F4 exp cond.	run 597(30ms)	run 585(60ms)
Ref. Length		.1114m
P_o [bar]	411	300
H_o [J/kg]	9.6	12.9
\bar{u} [m/s]	3934	4930
$10^3 \rho$ [kg/m ³]	1.557	.545
T [K]	188	795
T_{n2} [K]	4078	795
T_{o2} [K]	2485	795
T_{no} [K]	188	795
c_{n2}	.7254	.7629
c_{o2}	.1354	.2371
c_{no}	.0895	.0
c_n	.0	.0
c_o	.0497	.0
Re_L	54097.5	8290.8
M	13.89	8.70
$\frac{M}{\sqrt{Re}}$	$5.97 \cdot 10^{-2}$	$9.55 \cdot 10^{-2}$

Table 3.3: Exit conditions of F4 nozzle nr. 2, taken as freestream conditions for the hyperboloid-flare computations.

provided in the test case description booklet, of which the freestream conditions used here are derived. At that time the reservoir conditions were already defined but no corresponding wind tunnel data were available. In addition the maximum deviation in the total enthalpy and total pressure is 30% and 5%, respectively. The accuracy of measurements on the model itself is 5% for the pressures and 15% for the heat fluxes.

3.2.3 Results of numerical simulations

The computation is performed on a mesh consisting of 12 blocks. A zoom of the mesh near the flare is shown in Figure 3.17. As can be noticed, the separation bubble is captured within 6 blocks. The cell spacing at the wall is 10^{-6} m. This is necessary to resolve the thermal gradient at the cold wall. Figures 3.18 and 3.19 show the density and pressure contour lines in the vicinity of the interaction region. It shows the expansion fan and slip line produced by the interaction of the front bow shock and the merged separation and re-attachment shock.

For the flow field comparison, the only experimental result is the shock location deduced from the schlieren picture. A qualitative comparison in Figure 3.20 between the numerical result

	VUB	DLR	ONERA	ESTEC	CIRA	present
Scheme		Roe	VanLeer/ Osher	Roe	Roe	Ausm
Chem.	Park	Park	Gardiner	Dunn/Kang	Park	Dunn/Kang
V-T coupl	M&W	M&W	M&W	M&W	M&W	M&W
Transport	Blottner	Blottner	Blottner	Blottner	Blottner	Blottner
Lewis		1.2	1.1	1.2	computed	1.2
			Catalytic wall			
Grid (WS '94)		228x121	80x110 123x110 206x110	300x200	122x102	151x101 151x201 301x201 301x401
Grid (WS '96)	233x241	455x121	80x110 123x110 206x110	300x200	122x102	151x101 301x101 301x201 301x401

Table 3.4: Computational and modeling features of the different codes.[Devezeau and Tribot 1996]

and the schlieren picture shows a similar shock structure, although the numerical method predicts a larger separation zone.

A comparison is made with calculations from different institutes. In Table 3.4 the main features of the numerical and physical models are summarized. These numerical schemes are commonly used in hypersonic flow solvers. Since all numerical solutions yield a chemically frozen shock layer, the effect of different chemical reaction rates used by the contributors is negligible. This chemical freezing of the shock layer may be attributed to the slender and small model. There is only recombination in the boundary layer near the catalytic wall. Also all contributors have used the same vibration-translation relaxation law, the thermal relaxation should be the same. Therefore under these conditions one should not expect much difference in the results.

The pressure coefficients and heat fluxes along the model for WS'94 are shown in Figures 3.21 to 3.24, and for WS'96 in Figures 3.25 to 3.28. For both test cases a grid converged solution is achieved. Each finer mesh is restarted from the previous interpolated result. The convergence history for the L^2 norm of the density equation is plotted in Figure 3.29 for the test case '96 for the successive grid refinements. As a remark, one can notice that at $x=0.005\text{m}$, a kink in the pressure distribution is present. This is caused by the description of the contour, which is described by two polynomials. At their junction the polynomials do not have the same second order derivatives.

For both test cases the difference in the pressure coefficient as well as the heat fluxes of all numerical computations are below 5%. The calculations, performed by CIRA '94 and VUB '96, do not take into account the aft cylinder part of the model. Therefore on the aft part the heat flux and pressure coefficient along the aft part do not change abruptly. The change in geometry compared to the experiment in this case is not important for the separated region as shown in the results, since in this case this region is small relative to the flare.

The comparison of the results with experiments are within the measurement uncertainties for the hyperboloid part until the separated region is reached. Comparing the separation length for both test cases (WS'94 and WS'96), assuming that the influence of the almost chemically frozen flow on the shock-boundary layer is similar, the nonequilibrium freestream (WS'94) results in a larger separation length compared to the experimental data. The equilibrium freestream condition reduces the separation length, which agrees better with the experimental result. Based on this result, the nozzle exit conditions are most likely close to equilibrium. There are also other reasons pointing in this direction, see Chapter 4. The trend towards a smaller separation length for the WS' 96 case can be confirmed with the help Figure 3.30, where the non-dimensionalized separation length ($\Delta L/L$), taken from tests in different cold hypersonic wind tunnels (H2K, R5Ch, R3Ch, S4, HKK and RWG), is plotted against the viscous interaction parameter $\chi = M/\sqrt{Re}$. This parameter describes the influence of the inviscid flow interacting with the boundary layer where the influence of viscosity on the flow is dominant. The two test cases in the F4 have been added in the figure. Both experimental and numerical results show that higher values of χ yield smaller separation lengths. For lower values of χ the separation length increases until a laminar-turbulent transition modifies the interaction region.

3.2.4 Conclusion

The numerical method is capable of computing a hot hypersonic gas over the axisymmetric hyperboloid model. Since the shock layer on this model is chemically frozen, the thermal modeling of the gas was mainly evaluated. Comparison of the pressure coefficient as well as heat fluxes with other numerical data yield differences less than 5%. It shows that the numerical method yields results within the experimental uncertainty for the hyperboloid part. Depending on the assumption made for the freestream conditions, the equilibrium freestream condition yields better comparison of the separation length compared to the measurement. Even though the correctness of the freestream conditions could be questioned, the trend of reduced separation length is also confirmed by other wind tunnels.

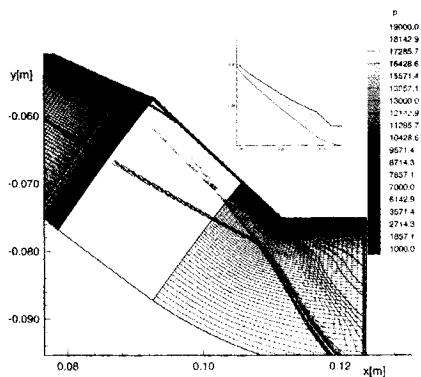


Figure 3.17: Enlarged view of the mesh (301x201) near the flare with Mach contour lines of the '94 test case.

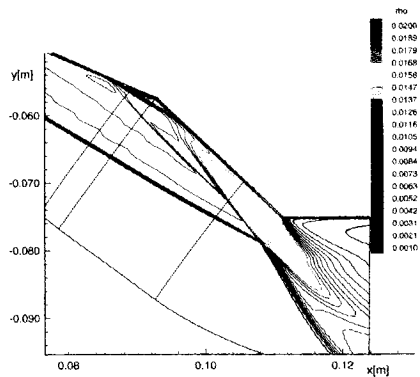


Figure 3.18: Density contours along the hyperboloid-flare WS'94.

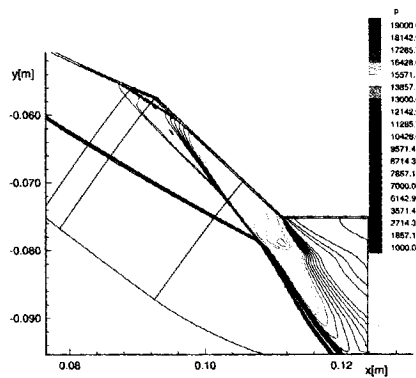


Figure 3.19: Pressure contours along the hyperboloid-flare WS'94.

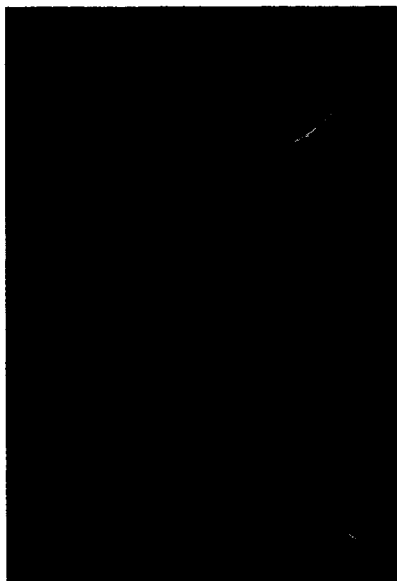


Figure 3.20: Schlieren picture (a) and computed Mach number contour lines (b) past the hyperboloid-flare.

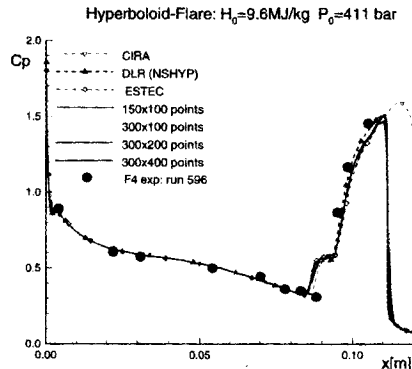


Figure 3.21: Wall pressure coefficient of hyperboloid-flare WS'94.

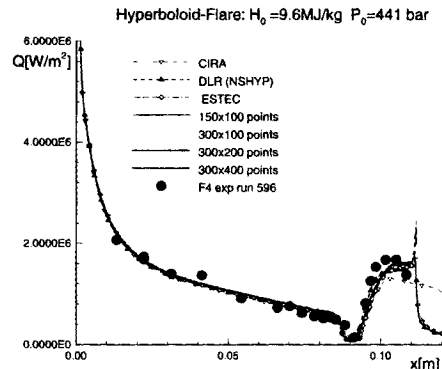


Figure 3.22: Heat flux of hyperboloid-flare WS'94.

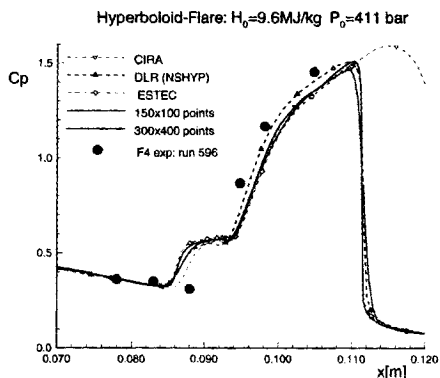


Figure 3.23: Enlarged view of the wall pressure coefficient near the separation zone of hyperboloid-flare WS'94.

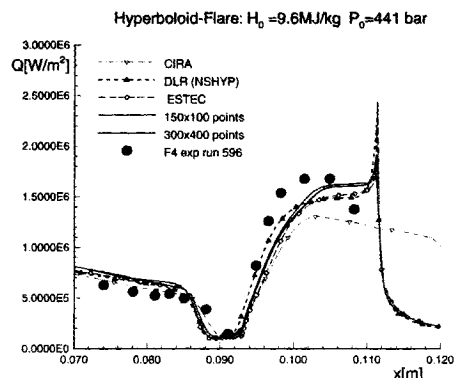


Figure 3.24: Enlarged view of heat flux distribution near the separation zone of hyperboloid-flare WS'94.

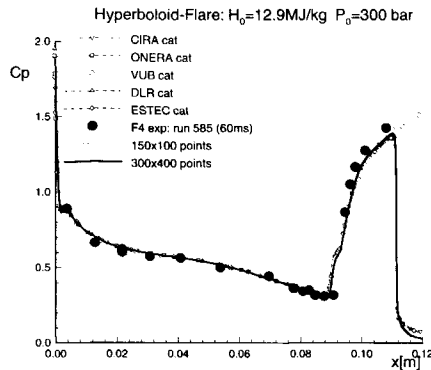


Figure 3.25: Wall pressure coefficient of hyperboloid-flare WS'96.

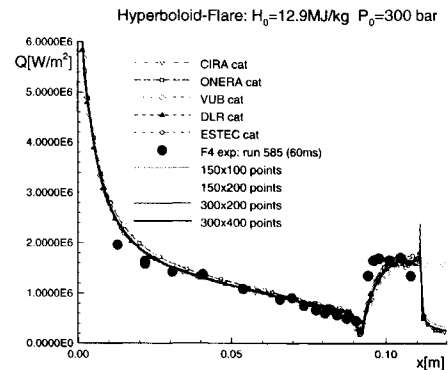


Figure 3.26: Heat flux of hyperboloid-flare WS'96.

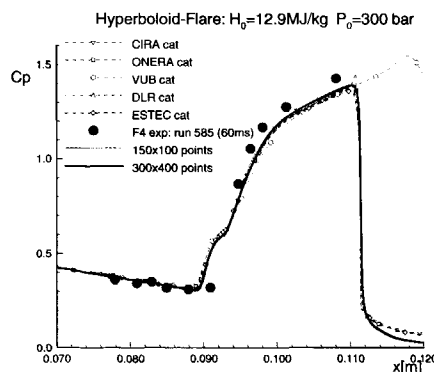


Figure 3.27: Enlarged view of the wall pressure coefficient near the separation zone of hyperboloid-flare WS'96.

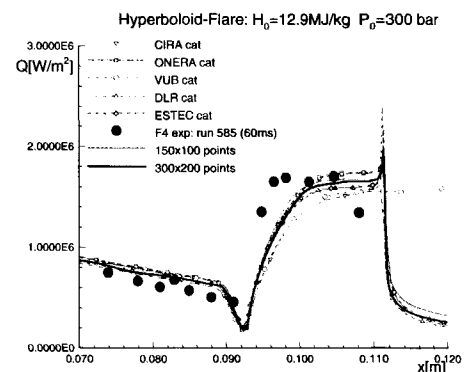


Figure 3.28: Enlarged view of heat flux distribution near the separation zone of hyperboloid-flare WS'96.

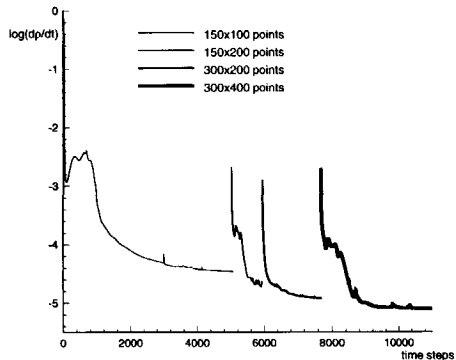


Figure 3.29: Convergence history for hyperboloid-flare test case '96.

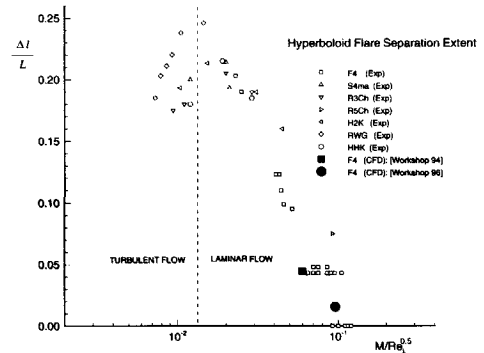


Figure 3.30: Correlation of measured and computed separation length of hyperboloid-flare.

3.3 RAM C-II flight experiment.

In this section the capability of the code to correctly simulate a weakly ionized flow field will be validated. Not many experiments have been carried out in hypersonic flow which reproduce this phenomenon. The freestream velocity should be sufficiently high to free the electrons. Hypersonic wind tunnels cannot reach these high energies. For this reason the RAM (Radio Attenuation Measurement) flight experiments were chosen to validate numerical results. These experiments were extensively studied by Candler [1988], Gnoffo [1989] and Park [1990].

3.3.1 Introduction

In the late 1960's, Langley Research Center (LARC) conducted in-flight measurements on sphere-cone shaped probes to understand the causes of degradation in the radio signal during earth re-entry of a space vehicle, Schexnayder et al. [1970], Akey and Cross [1970] and W.L. Jones and Cross [1972]. The RAM project was designed to obtain data in the velocity regime of about 7620 m/s. At these speeds the energy is high enough to weakly ionize the flow around the probes.

Three series of flights were made, namely RAM C-I, RAM C-II and RAM C-III. These probes were sphere-cone configurations with a nose radius of 0.1524 m, 9° cone half angle and a length of 1.295 m. The RAM C-I had water injection at the nose. The RAM C-II probe was covered by a Beryllium heat sink nose cap and a Teflon coated after body. The RAM C-III, of which a sketch is drawn in Figure 3.31 used water and electrophilic fluid for blackout alleviation. Only the RAM C-II flights are used for comparison since the other two were covered by a phenolic-graphite charring ablator polluting the flow field. Up to 55 km, the RAM C-II had Beryllium heat sink nose cap positioned over a Teflon ablator which resulted in a clean flow field. After 55 km the nose cap was ejected leaving the Teflon as ablator.

The probes were instrumented to measure the electron density at four axial locations using microwave reflectometers, [Lochte-Holtgreven 1968], and in the boundary layer near the end of the cone using an electrostatic rake.

3.3.2 Test case description

Two altitudes, at 71km and 61km, were chosen to simulate the RAM-C II flight in which in the first case the shock layer is both in a thermal- and chemical nonequilibrium situation and for the second case is close to a thermo-chemical equilibrium flow regime. The corresponding freestream conditions are given in Table 3.5. Since the Reynolds number is very low the assumption is made that the flow is laminar. For each of the cases the Dunn and Kang [1973] model and the Park [1993] chemistry model, both incorporating 11 species, were applied. Since the flight wall temperature is unknown, the assumption is made that the wall

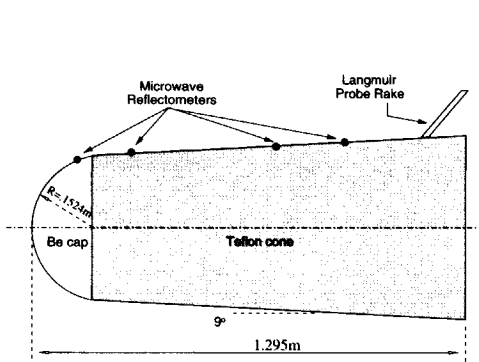


Figure 3.31: RAM configuration.

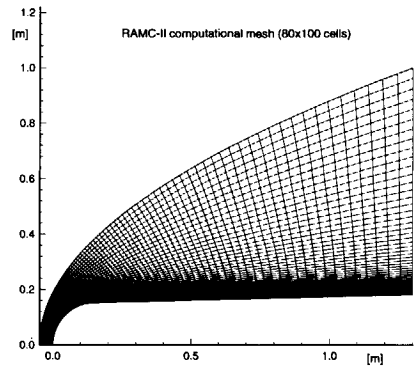


Figure 3.32: RAM computational mesh (80x100).

Altitude [km]	71	61
M	25.90	23.86
$V[m/s]$	7658.6	7636.4
$T[K]$	216.0	254.0
$P[Pa]$	4.764	19.856
$\rho[kg/m^3]$	$7.631 \cdot 10^{-4}$	$2.714 \cdot 10^{-4}$
Re/m	36470.	116501.
c_{N_2}	0.7624	0.7624
c_{O_2}	0.2376	0.2376

Table 3.5: Flight conditions for RAM C-II.

temperature is fixed at 1500K in accordance with the computations of Candler [1988] and Gnoffo [1989]. The melting point of Beryllium is 1550 K. Therefore the choice of the wall temperature could be too high. The influence of the wall temperature as well as the catalycity is examined.

3.3.3 Results of numerical simulation

A grid convergence study was made with four meshes, each time doubling the number of points in each direction. The size and the smallest distance to the wall are given in Table 3.6. The computational mesh (80×100 cells) is shown in Figure 3.32. The grid points have been clustered near the wall. As a general numerical procedure, the solution of the coarse solution is interpolated on the doubled mesh. The mesh has been divided into 4 blocks, such that it

grid cells	$\Delta[m]$
40×50	$1 \cdot 10^{-5}$
80×100	$5 \cdot 10^{-6}$
160×200	$1 \cdot 10^{-6}$

Table 3.6: Grids used for RAM C-II flight simulation.

could run parallel on 4 processors.

The temperature distribution on the stagnation line of the RAM configuration, for all meshes, is shown in Figure 3.33, in which T_{el} denotes the electron temperature, T_{vN_2} the vibrational temperature of N_2 and T the translations-rotational temperature.

There is a strong degree of thermal nonequilibrium behind the shock and only close to the wall the vibrational and electron temperature equilibrate to the translational. Using subsequently a finer resolution around the shock, sharpens the shock and increases the translational temperature closer to frozen gas values.

The molar concentration for the electron and ionized species on the stagnation line, with a catalytic and non-catalytic assumption at the wall, are plotted for the Dunn and Kang model in Figure 3.34 and for the Park model in Figure 3.35, respectively. One can notice that the concentrations are still very low (10^{-3} or lower), even for the high temperatures occurring in the stagnation zone. The concentrations are similar for both models except for species O^+ , caused by the different chemical rates. The difference between a non-catalytic and a catalytic wall assumption is only noticeable close to the wall. Since the diffusion coefficients for all the ionized species are the same, one can easily verify that the sum of the ionized species mole fractions equals the electron mole fraction locally: there is conservation of the charged species and electrons.

The effect of the use of a multi-vibrational temperature model or an average vibrational temperature is show in Figure 3.36 and Figure 3.37. All vibrational temperatures are similar and close to the average vibrational temperature. The effect on the mass fractions is negligible.

The heat fluxes along the wall for the subsequent refined meshes are plotted in Figure 3.38. There is a large noticeable decrease in heat flux from catalytic to the non-catalytic assumption. But the difference for the catalytic case between Park's and Dunn and Kang model is small compared to the non-catalytic case since all energy stored in the dissociated molecules is forced to be released at the wall. For the non-catalytic case the heat flux depends mostly on the recombination rate of the species given by the chemistry model, which are different for both models. In Figure 3.39, the peak electron number density versus axial distance of the RAM C-II at 71km is plotted. The peak electron number density is the maximum value normal from the wall. A good agreement is found with the Dunn and Kang model assuming

a catalytic wall. Park under predicts the electron densities.

Figures 3.40, 3.41 and 3.42 compare the computed results to the electron number density near the end of the body at $x=1.234\text{m}$ for an altitude 71km and 61 km. Again the Dunn and Kang model correctly predicts the electron number density in contrast to the Park model. At 61 km altitude the Dunn and Kang model also correctly predicts the flight experimental values assuming a catalytic wall.

As stated earlier, the assumption of a wall temperature of 1500K is not clear. A sensitivity analysis is made by lowering the temperature from 1500K to 1000K. The effect of the wall temperature on the electron density is shown in Figure 3.43 and Figure 3.44. There is only a noticeable difference in the vicinity of the wall, but this is within the uncertainties of the experimental values.

3.3.4 Conclusion

The numerical method comprising an 11 species air model with two chemical rate models has been applied to two different flow conditions, ranging from a “moderate” reactive flow field at 71 km altitude to a near equilibrium flow at 61km. For all the results grid convergence was shown, in contrast to other authors [Candler 1988; Gnoffo 1989]. As Gnoffo [1989] stated, numerical dissipation can become important if the grid is too coarse. Therefore, Gnoffo’s results have not been used for comparison.

The results from Candler [1988] agree well with the peak heating, but not with the electrostatic rake at the end of the probe. There are two possible explanations for this difference. Candler used a mesh of 35x50 points which is much less refined near the wall. Also he used 7 species instead of 11 (only allowing NO to ionize into NO^+) under the assumption that NO^+ ionize more easily compared to other ionized species (O^+ , N^+ , N_2^+ and O_2^+).

Assuming a catalytic wall, the results agree better with the experimental data than those with a non-catalytic wall. It is shown that the Dunn and Kang model with a catalytic wall predicts the electron density within experimental uncertainty. On the other hand the Park model underestimates the electron density. This trend is also confirmed by Gnoffo, although he used an older chemistry model by Park. Generally speaking, Park’s rates are faster than those in Dunn and Kang’s model.

The results also indicate that using one average vibrational temperature instead of a multi-temperature model is sufficiently adequate to model the physics in the flow field accurately.

The influence of the wall temperature is negligible with respect to the measured electron densities in flight.

Since the physical model is very complex and only the measured electron density could be compared, the validation is not complete. Experimental tests with other flow field quantities in similar environments are required to validate more aspects of the flow field.

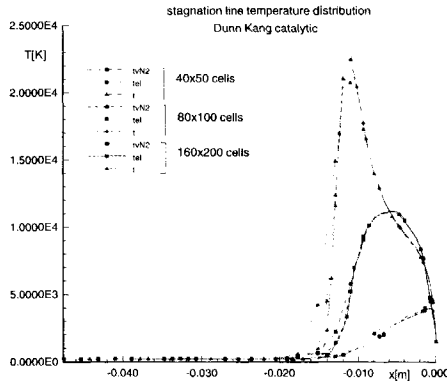


Figure 3.33: Influence of grid convergences on stagnation line temperatures using a 3 temperature model.

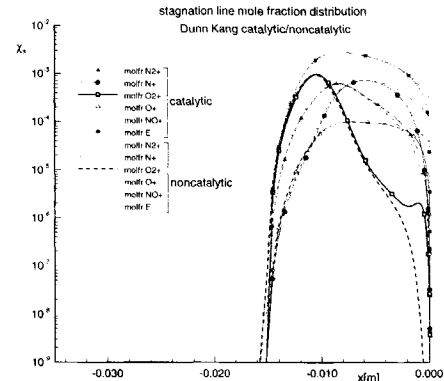


Figure 3.34: Stagnation line mole fraction distribution using a 3 temperature model.

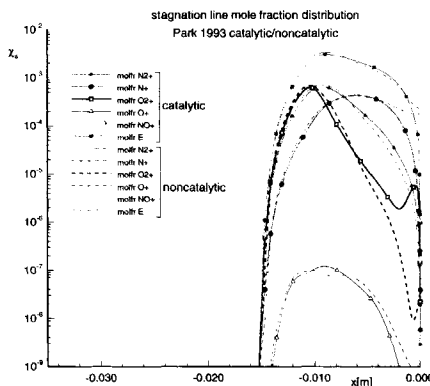


Figure 3.35: Stagnation line mole fraction distribution using a 3 temperature model.

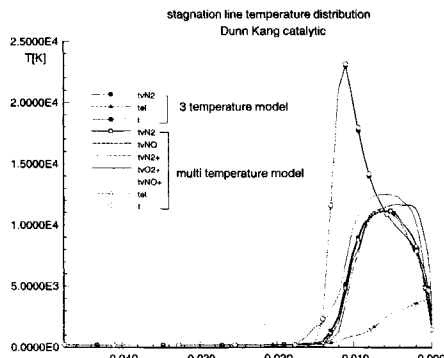


Figure 3.36: Comparison of stagnation line temperature using a 3- and multi-temperature model.

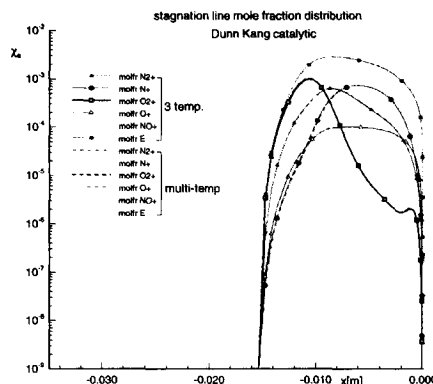


Figure 3.37: Comparison of stagnation line mole fraction distribution using a 3- and multi-temperature model.

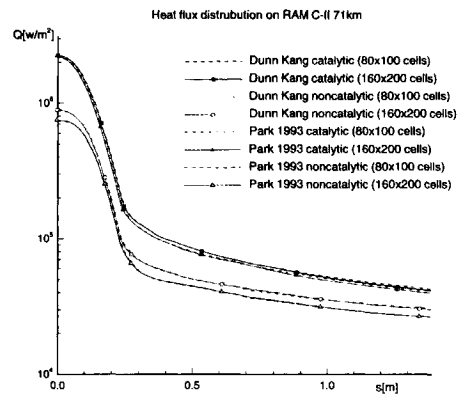


Figure 3.38: Comparison of stagnation line mole fraction distribution using a 3- and multi-temperature model.

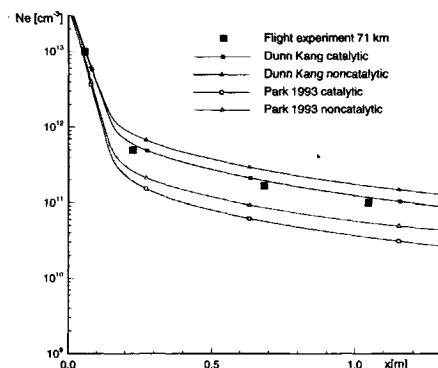


Figure 3.39: Peak electron number density versus axial distance for RAM C-II at 71km.

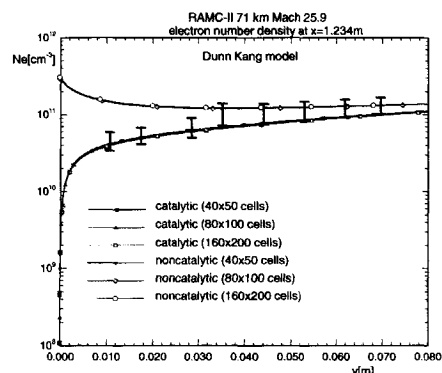


Figure 3.40: Electron number density versus normal distance for RAM C-II at $x=1.234\text{m}$, 71km using Dunn and Kang model.

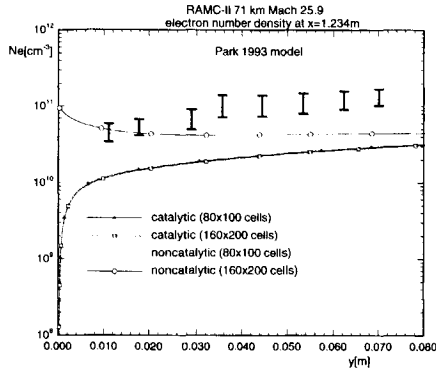


Figure 3.41: Electron number density vs normal distance for RAM C-II at $x=1.234\text{m}$, 71km using Park 1993 model.

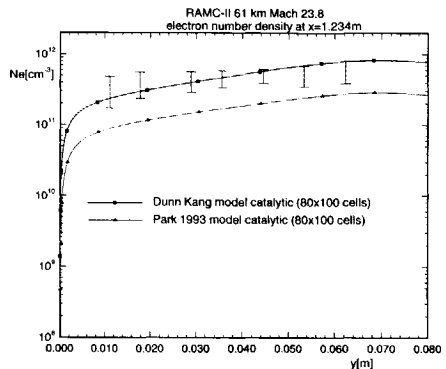


Figure 3.42: Electron number density vs normal distance for RAM C-II at $x=1.234\text{m}$, 61km.

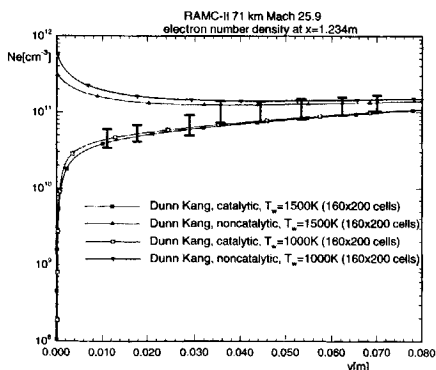


Figure 3.43: Influence of wall temperature on electron number density vs normal distance for RAM C-II.

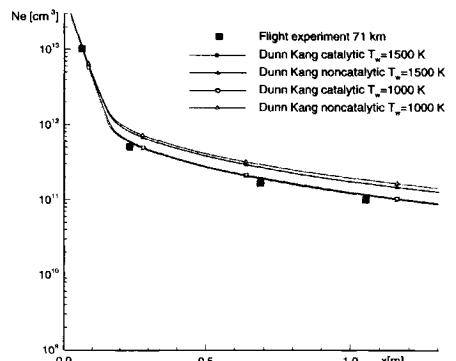


Figure 3.44: Influence of wall temperature on peak electron number density vs axial distance for RAM C-II at 71km.

3.4 Conclusions

In this chapter we have selected test cases, typical for the physics encountered in a hypersonic flow regime, to validate and verify the solver. They range from perfect gas (cold) to thermo-chemical nonequilibrium ionized gas in hypersonic flow regime (hot). Moreover, all test cases have been selected such that the uncertainty resulting from turbulence is avoided in this validation exercise by selecting laminar flow conditions.

It has been verified that the solver converges in space and in time towards a unique solution. In addition the solutions have been successfully compared with available experiments and other numerical results.

When analyzing the experimental results it becomes clear that, when the complexity of the flow field in terms of physics increases, the experiments exhibits uncertainties in model setup, freestream conditions and experimental measurements techniques, which make it difficult to assess the validity of the numerical simulation.

Therefore in the next section, we will assess the influence of the different thermo-chemical models in hypersonic wind tunnels to characterize flow fields on models in high enthalpy wind tunnels.

4

Hot hypersonic nozzle flow

4.1 Introduction

The characterization of the flow conditions in the test section of hypersonic short-duration wind tunnels is usually based on the measurement and/or theoretical determination of the total pressure and total enthalpy in the tunnel reservoir, nozzle wall static pressures and heat fluxes, and the Pitot pressure in the test section. As long as detailed test section flow field measurements are not available, the test section flow field is usually obtained by the computational modeling of the nozzle expansion process. The nozzle expansion process in high-enthalpy facilities however is complicated by thermo-chemical nonequilibrium or non-isentropic effects. These effects have to be modeled properly in order to know the correct free-stream conditions for the model placed in the test section flow field.

The subsequent discussion focuses on the sensitivity of computed test section flow field properties upon a number of assumptions made in the calculation of the nozzle expansion and on the adequacy of test section and nozzle wall measurements for the validation of computational models. For this purpose, two high-enthalpy wind tunnels are considered: the ONERA F4 arc jet facility and the DLR HEG piston-driven shock tunnel. A brief description of the F4 and HEG wind tunnels is presented in Appendix C.1 and C.2. In addition, the effects of the computed test section flow field properties on the pressure and heat transfer distributions over the Electre blunt cone standard test model are examined to estimate the sensitivity of test section conditions on the experimental results.

According to Seibert et al. [1992], four basic parameters must be considered in hypersonic wind tunnel flows:

1. the total temperature or enthalpy which determines the maximum velocity attainable,
2. the total pressure which determines the test pressure, and therefore the altitude to be simulated, and which has an effect on the nature of the gas,
3. the size of the test section which determines the scale and
4. the test duration which determines the type of instrumentation that can be used and the erosion from the wind tunnel structure into the hot flow.

To simulate high temperature gas effects in a wind tunnel as they occur in flight conditions, it is necessary to create a test gas with an enthalpy high enough to vibrationally excite and dissociate the molecules. At a temperature of about 3000 K, oxygen dissociation in equilibrium becomes significant under atmospheric pressures. This corresponds to a free flight velocity of about 2.8 km/s or a specific enthalpy of $h=4$ MJ/kg. At this temperature the beginning of the high enthalpy flows of air is usually defined. The dissociation enthalpy of O_2 is 15.4 MJ/kg and for N_2 it is 33.6 MJ/kg. At specific enthalpies $h > 27$ MJ/kg electronic excitation becomes important. These enthalpies are not reached today in hypersonic wind tunnels designed for external aerodynamic testing.

High enthalpy flows are achieved by heating the test gas prior to the expansion through the wind tunnel nozzle. The test gas can be heated by electrically created plasma arcs or by moving shock waves. These methods are used in the ONERA F4 hot shot wind tunnel and the free piston driven wind tunnel, respectively. For re-entry vehicles, like Hermes and X-38, high Mach numbers are required. These high Mach numbers are achieved by creating high expansion ratio's of the nozzle. The limiting factor for expansion is the condensation of the test gas.

The requirement to produce high densities in high enthalpy flows, puts a limit on the operation for high enthalpy wind tunnels. Due to high radiative and convective heat fluxes at the wall, the wall material melts, boils and contaminates the flow field.

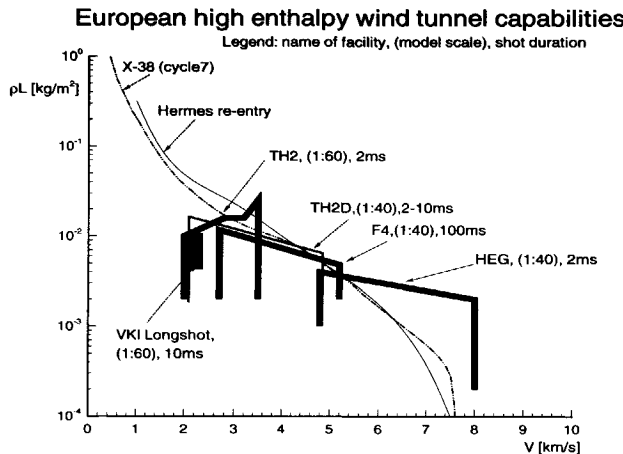


Figure 4.1: High enthalpy wind tunnel performance and re-entry trajectories of Hermes and X-38.

The performance of four European facilities is compared in Figure 4.1. Between brackets the model scale and the shot duration is given. For comparison the trajectories of Hermes and X-38 are incorporated. The performance is expressed in terms of the binary scaling parameter ρL , versus the flight velocity; L is the characteristic length of the model, and ρL represents

the number of collisions between the molecules. The reservoir pressure determines the ρL that can be achieved. The F4 and HEG are complementary since F4 covers enthalpies up to those corresponding to the complete dissociation of oxygen, whereas HEG starts where the nitrogen dissociation starts. Note the interesting overlap region at about 5000 m/s. Therefore the F4 and HEG conditions selected for the computations in this chapter are chosen in this region. Also shown in this figure is the performance envelop of the TH2 shock tunnel from the RWTH Aachen in Germany and the long-shot at the VKI Brussels in Belgium. In the TH2, simulation is possible up to 3500 m/s where vibrational excitation occurs and oxygen dissociates slightly, whereas the operation with the detonation driver TH2D allows flow velocities up to 4800 m/s corresponding to a total enthalpy of 14.5 MJ/kg.

4.2 Nozzle Flow

The conditions for F4 and HEG wind tunnels were chosen such that they have almost similar reservoir conditions as shown in Table 4.1. Although both wind tunnels have a contoured nozzle, their nozzle shape differ: the throat radius is 5 mm and 11 mm, respectively, the area ratio is 4489 and 1600, and the half cone angle from the throat is 8, respectively 15 degrees yielding for the HEG a more rapid expansion just after the throat.

	P_0 [bar]	H_0 [MJ/kg]
F4	430	20.4
HEG	408	15.7
HEG	408	21.0
HEG	408	22.3

Table 4.1: Reservoir conditions for F4 and HEG computations

High-density real gas effects may become important in the first stages of the nozzle expansion in hypersonic wind tunnels operating at high reservoir pressure. Today, the operation of high-enthalpy facilities, however, is restricted to relatively low reservoir pressures primarily to avoid the erosion of internal walls of the wind tunnel structure that occurs at high-enthalpy/high-pressure operation. Consequently, the operating conditions considered here are free of high-density real gas effects, the presence of which would call for an increased computational complexity in the numerical simulation of high-enthalpy tunnels. As illustrated in Figure 4.2 the maximum density encountered in the nozzle reservoir, depicted with a vertical line, is seen to be almost an order of magnitude lower than the level where intermolecular forces become important.

To compute the F4 and HEG nozzle flow a two-dimensional mesh was constructed with 282 points in streamwise direction and 100 points normal to the wall. The smallest cell spacing normal to the nozzle wall in the throat is $1 \cdot 10^{-7}$ m and increases to $1 \cdot 10^{-6}$ m at the exit of the

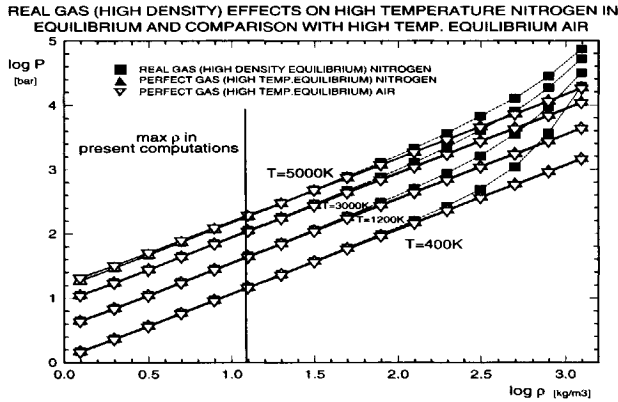


Figure 4.2: High-density real gas effects.

nozzle, allowing about 50 grid points in the boundary layer and the Reynolds number, based on the smallest cell size at the wall, is smaller than 1.0 for the current test cases. In Figure 4.3 and 4.4 the meshes for the F4 nozzle “number 2” and the HEG contoured nozzle are shown. These meshes are optimized to give a grid converged solution for the current conditions and have been used in the ESTEC-EHVDB workshop ’94 and ’96 where the solutions show very good agreement with other contributors. In the figures, comparing the Mach contour lines to the mesh, one can see how the mesh was adapted to capture the large boundary layer which develops in these facilities.

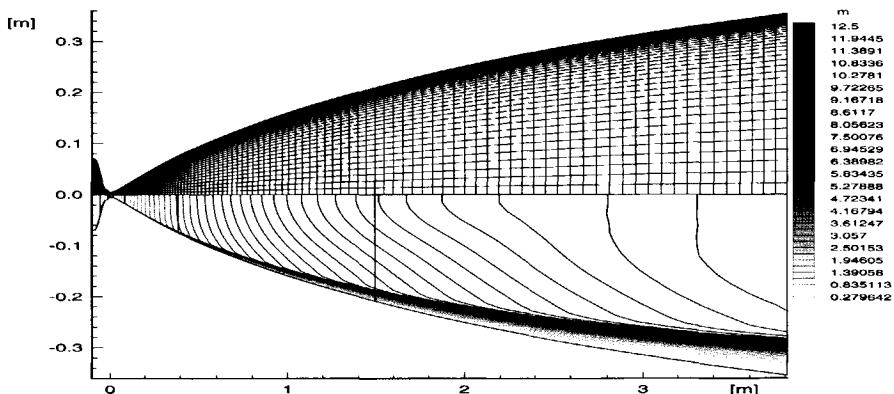


Figure 4.3: Computational mesh used for the F4 nozzle together with a two temperature laminar solution for a reservoir pressure of 430 bar and total enthalpy of 20.4 MJ/kg.

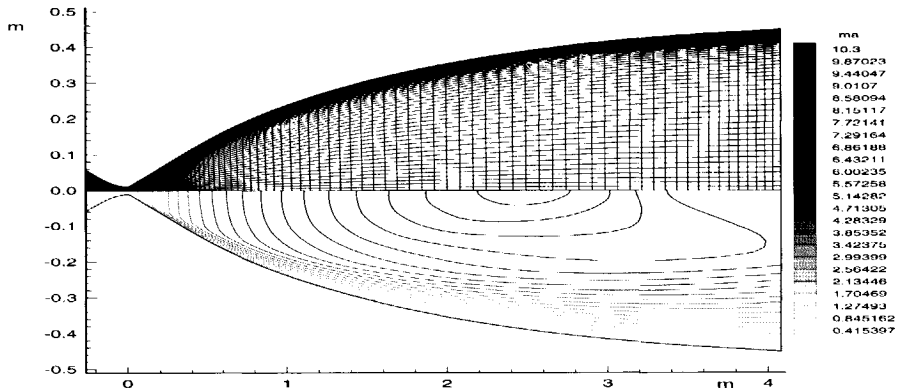


Figure 4.4: Computational mesh used for the HEG nozzle together with a two temperature turbulent (Baldwin-Lomax) solution for a reservoir pressure of 408 bar and total enthalpy of 21 MJ/kg.

For the quasi one-dimensional computations 2000 grid points are used. This is done since the run times are small (10 minutes on a SGI RISC 12000) compared to the axisymmetric computations (about 1-2 hours). The axisymmetric nozzle computations are started from the quasi one-dimensional solution and take about 2000 iterations to resolve the boundary layer in the nozzle on the very fine mesh. The quality of the solutions in terms of mass conservation of the nozzle flows is checked by computing the mass flow rate. In Figure 4.5 the mass flow rates for a quasi one-dimensional computation with a four temperature model and axisymmetric laminar computations assuming a two- and a four-temperature model are plotted of the F4 nozzle. The maximum deviation is 0.8 % for the axisymmetric computations, occurring in a small region behind the throat where a very strong expansion appears.

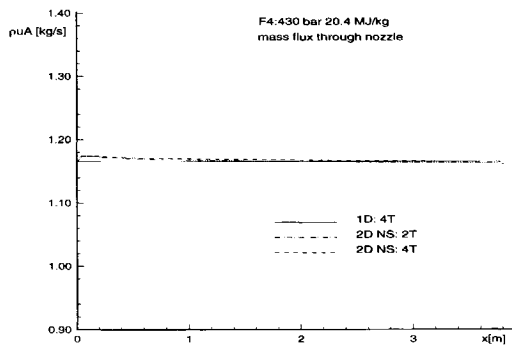


Figure 4.5: Mass flux distributions along F4 nozzle wall for quasi one-dimensional and axisymmetric laminar computations.

4.2.1 Nozzle exit flow sensitivity

The expansion along the nozzle number 2 of the ONERA F4 facility has been computed for a reservoir pressure of 430 bar and total enthalpy of 20.4 MJ/kg with various thermal and chemical nonequilibrium models: thermal equilibrium, full equilibrium and so-called “vibrational melting”. The latter model assumes a sudden vibrational relaxation at various streamwise stations, possibly caused by the presence of contaminants eroded from the tunnel structure (similar to the water vapor effects), as proposed by Boudreau and Adams [1988].

The centerline distribution for Mach number, temperature and mass fractions are plotted in Figures 4.6, 4.7 and 4.8 respectively. Relevant flow field parameters at the nozzle exit from quasi one-dimensional calculations are summarized in Table 4.2 together with exit centerline laminar flow values of axisymmetric nonequilibrium Navier-Stokes simulations.

From these figures one can draw the following conclusions:

1. The use of four- rather than two-temperature models is seen to have little influence on the free-stream conditions, and the same holds for the V-V coupling; it is likely that V-V coupling will be more significant above 2000 K. The Treanor-Marone (V-D) coupling inverts the relative magnitudes of T_{N_2} and T_{O_2} for this test case.
2. A significant difference is noted between the Park and Dunn & Kang chemical reaction rates where the former gives a somewhat lower Mach number. This can be attributed to the higher temperature in the Park case, a result of the faster reaction rates of the dissociation-recombination reactions in this model. For these reactions, the recombination dominates in the strong expansion and therefore in case of the Park model more energy is released into the flow.
3. Thermal and full equilibrium computations yield lower Mach number distributions by virtue of the increasingly higher temperatures. The vibrational melting model yields temperatures that are significantly higher than the thermal equilibrium case due to the irreversibility of the process and the associated entropy rise.
4. The chemical nonequilibrium behavior on the centerline of the nozzle can be seen from Figure 4.8. The freezing of the mass fractions is best seen compared with the equilibrium solution.

The measured and computed transverse Pitot pressure distributions in the test section of the F4 nozzle, are shown in Figure 4.9. Reasonable agreement is found between the measurements and the axisymmetric nonequilibrium computations assuming a laminar nozzle-wall boundary layer, compared to a turbulent (Baldwin-Lomax) assumption. The corresponding 1D results with various thermo-chemical models are also shown to be in reasonable agreement with the measured Pitot pressure in the inviscid core of the flow. Closer examination of Table 4.2, however, shows that the Pitot pressure is almost totally insensitive to the thermo-chemical behavior or non-isentropic flow expansion along the nozzle. Consequently, the

F4: 430 bar - 20.4 MJ/kg at nozzle exit x=3.56m from throat												
chem. therm. coupl.	DK 2T 2D NS	DK 4T 2D NS	DK 2T	Pk 2T	DK 4T	DK 4T	DK TM	Pk TMVV	DK 4T VV	DK IT equil	DK IT th eq	DK 2T melted
M	12.66	12.56	13.22	12.67	13.13	13.44	13.03	12.58	7.20	11.16	9.12	
$\frac{Re}{10^5 m}$	1.622	1.607	1.604	1.478	1.567	1.657	1.583	1.452	0.601	1.266	1.030	
$u[m/s]$	5833.	5797.	5785.	5802.	5819.	5797.	5821.	5836.	6102.	5862.	5847.	
$\rho[10^3 kg/m^3]$.6713	.6758	.6335	.6250	.6267	.6352	.6349	.6203	.5689	.6351	.6654	
$p[Pa]$	97.	98.2	83.89	90.82	85.18	81.64	87.49	92.42	292.1	121.2	189.0	
T	438.	399.	441.	410.	384.	412.	452.	1770.	577.0	855.2		
T_{n2}	4045	4257.	3911.	3871.	4248.	4235.	4172.	4153.	1770.	577.0	855.2	
T_{o2}	4045.	2435.	3911.	3871.	2408.	5005.	4955.	2560.	1770.	577.0	855.2	
T_{no}	4045.	3230.	3911.	3871.	3229.	3346.	4121.	3917.	1770.	577.0	855.2	
c_{n2}	.7906	.787	.7880	.7874	.7879	.7908	.7911	.7874	.7973	.7874	.7887	
c_{o2}	.0177	.021	.0254	.0340	.0247	.0175	.0165	.0327	.1946	.0263	.0229	
c_{no}	.0204	.0263	.0255	.0268	.0257	.0196	.0191	.0268	.0056	.0269	.0241	
c_n	.	.0	.0	.0	.0	.0	.0	.0	.0	.0	.0	
c_o	.1713	.161	.1608	.1516	.1615	.1720	.1733	.1529	.0022	.1592	.1641	
$p_{t2}[Pa]$	21013	20893	19391	19251	19410	19510	19663	19333	19625	19975	20852	

Table 4.2: Comparison of F4 nozzle exit flow conditions using various methods (reservoir conditions $P_0=430$ bar and $H_0=20.4\text{MJ/kg}$).

measurement of Pitot pressure alone in the test section is not adequate to characterize the test-section flow field in high-enthalpy facilities (in contrast to perfect gas/equilibrium facilities with isentropic nozzle expansion).

Similar to the Pitot pressure, the free-stream velocity and density are also highly insensitive to the thermo-chemical behavior of the nozzle flow, as opposed to the significant sensitivity observed in the free-stream pressure and temperature. These comments apply to the specific flow conditions encountered in present-day high-enthalpy wind tunnels, particularly for those having a moderately high level of total pressure where freezing occurs after a significant acceleration of the flow. In contrast, low pressure high enthalpy facilities (e.g. materials testing arc-jets), where freezing could occur upstream and closer to the nozzle throat, may exhibit a more significant sensitivity of the nozzle exit velocity and density upon the thermo-chemical behavior of the flow expansion.

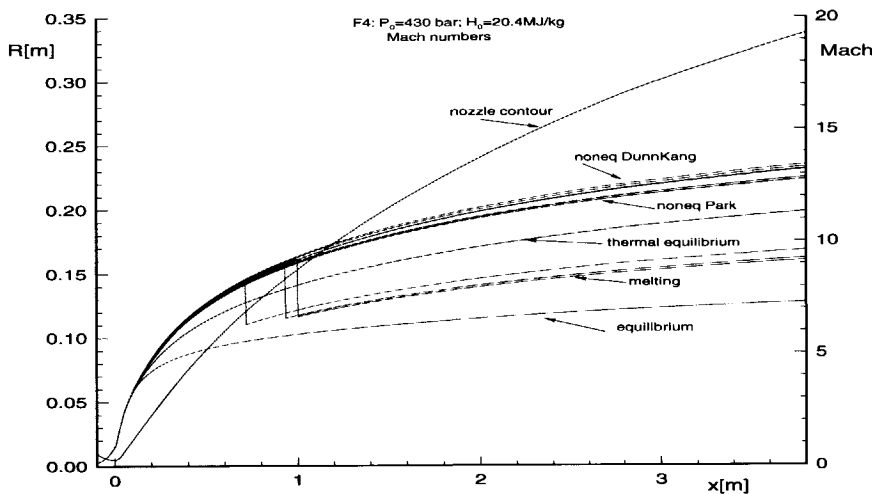


Figure 4.6: Mach number distributions along the F4 nozzle from 1D predictions, computed with various thermo-chemical models shown in Table 4.2.

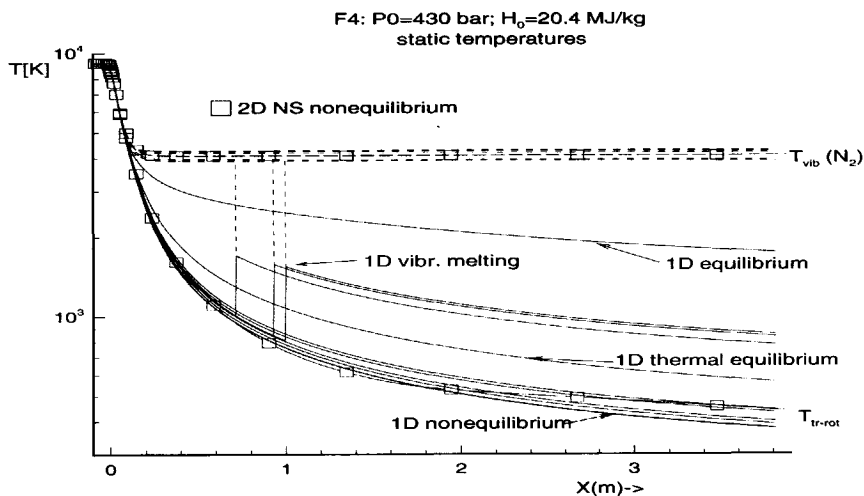


Figure 4.7: Temperature (translational and vibrational) distributions in F4 nozzle, computed with various thermo-chemical models shown in Table 4.2.

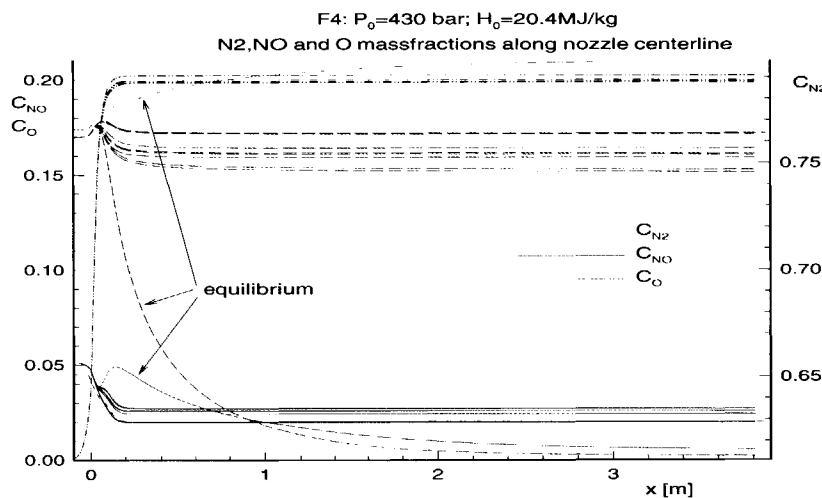


Figure 4.8: Mass fraction distributions along centerline of the F4 nozzle computed with various thermo-chemical models shown in Table 4.2.

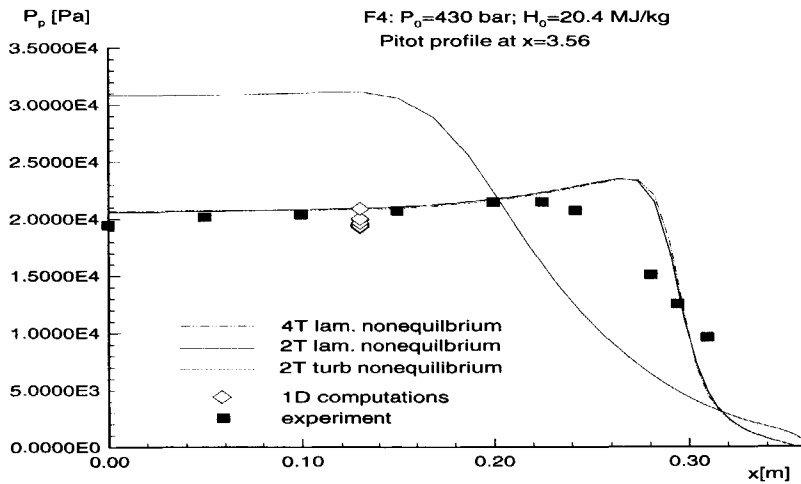


Figure 4.9: Comparison of measured and computed Pitot pressure in F4 test section at $x=3.56$ m, computed with various thermo-chemical models shown in Table 4.2. For clarity, the quasi one-dimensional results, representing the average values of the core flow, are plotted about $y=12$ m.

4.2.2 Nozzle wall distributions

To improve the level of characterization of the nozzle expansion and, thus, of the test section freestream conditions, surface pressure and heat transfer measurements have been performed along the F4 and HEG nozzle walls.

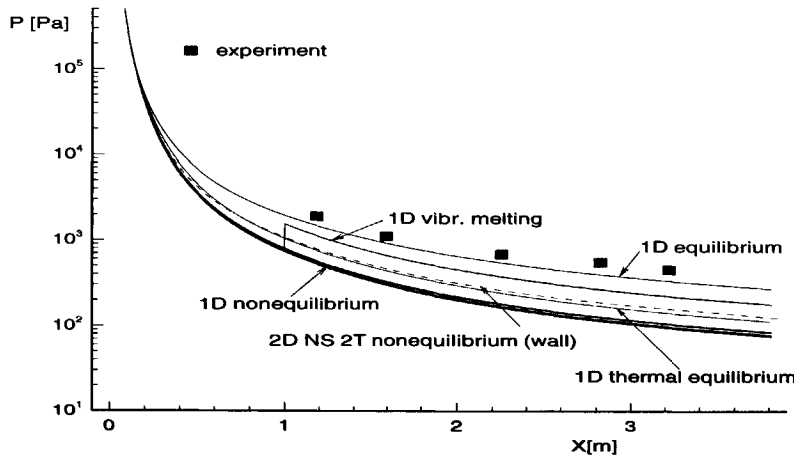


Figure 4.10: Pressure distributions along F4 nozzle wall, computed with various thermo-chemical models shown in Table 4.2.

To this end, the pressure distribution measured along the F4 nozzle wall is compared with 1D results using various thermo-chemical models in Figure 4.10. Moreover, the wall values obtained with an axisymmetric laminar two-temperature calculation are plotted. Also the wall pressure distributions from axisymmetric nonequilibrium computations are compared with PANASCE, [Verant 1994], which is a Parabolized Navier-Stokes code in Figure 4.11. As shown, there is an excellent agreement between the wall pressures of the two different codes assuming a nonequilibrium expansion, moreover the wall pressures are not dependent on the catalytic/non-catalytic boundary conditions nor on the use of a two or multi-temperature model. Only the solution from PANASCE with an equilibrium assumption yields better agreement with the experimental values.

It appears that the best prediction of the measured wall pressure distribution is provided by the axisymmetric and 1D full thermo-chemical equilibrium assumption (see Figure 4.10) along the nozzle, see also Sagnier [1995]. Although, from the comparison between the nonequilibrium 1D and axisymmetric wall computed pressures in Figure 4.10, it can be noted that the 1D computations tend to provide a transverse mean of the actual pressure field which is of the order of 0.8 times the respective axisymmetric predictions along the nozzle wall. Therefore,

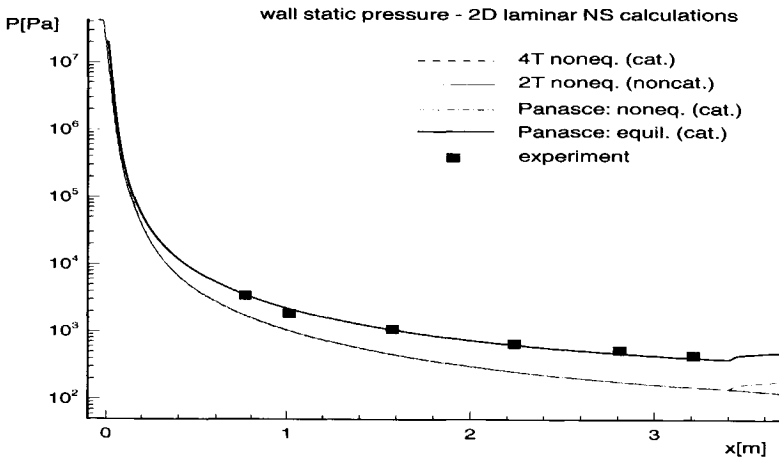


Figure 4.11: Comparison of wall pressure distributions with axisymmetric laminar computations along F4 nozzle.

if the 1D results are extrapolated to the nozzle wall by such a factor, the model assuming a sudden vibrational relaxation may be very close to the measurements. An assumption of sudden vibrational relaxation, possibly caused by the presence of contaminants eroded from the tunnel structure, appears to be more plausible than a full thermo-chemical equilibrium assumption, at least for this high-enthalpy rapid nozzle expansion test case.

An alternative explanation for the apparent (according to the comparison between computed and measured data) near-equilibrium thermo-chemical behavior of the flow along the F4 nozzle could be related to some inadequate modeling of the thermo-chemical nonequilibrium effects. With reference to Figure 4.7, it is noted that vibrational freezing occurs some distance downstream of the throat (i.e. after a significant flow acceleration, in contrast to lower pressure facilities), but nevertheless, in a region exhibiting very high gradients of the flow properties. The same applies for the freezing of atomic oxygen, whereas nitrogen in these conditions is close to equilibrium throughout the nozzle, as illustrated in Figure 4.8. So if freezing takes place just a few centimeters downstream of the numerically predicted location, this would occur at significantly lower temperatures and thus the flow would remain much closer to equilibrium than in the present predictions. Upcoming non-intrusive flow field measurements are expected to shed more light on these open questions on nozzle-expansion assumptions and the adequacy of thermo-chemical models.

The measured pressure distribution along the HEG nozzle wall is compared to equilibrium and nonequilibrium predictions in Figure 4.12 for three levels of total enthalpy. Excluding the

data point located at approximately 1.56 m downstream of the nozzle throat, which is said to have been obtained with a “problematic” pressure gauge [Krek et al. 1995], good agreement is found with the axisymmetric nonequilibrium predictions. The fact that one-dimensional computations yield a pressure distribution lower than the wall values, is supported by the nonequilibrium character of the flow expansion in the HEG nozzle. Furthermore, the sensitivity of the pressure distribution to the level of total enthalpy is seen to be modest.

The heat transfer distribution measured along the HEG nozzle is compared to the axisymmetric predictions, and to reference enthalpy predictions for conical boundary layer based on the 1D results in Figure 4.13. The correlation for a conical boundary layer is used since boundary layers in nozzles grow less rapidly than flat plate boundary layers due to the divergent streamlines. Following the discussion of Simeonides [1995], the heat flux correlation is given by:

$$Q = C St \rho_e u_e (h_{ad.wall} - h_{wall}) , \quad (4.1)$$

where subscript e denotes properties evaluated at the edge of the boundary layer or in this case from the inviscid 1D calculations. The correction factor $C = (9/4)^{0.2}$ is for a turbulent conical boundary layer compared to a turbulent flat plate, and $h_{ad.wall}$ is the adiabatic recovery wall enthalpy. The Stanton number is given by:

$$St = \frac{0.0296}{(Re_{e,x})^{1/5}} \left[\frac{\rho^*}{\rho_e} \right]^{4/5} \left[\frac{\mu^*}{\mu_e} \right]^{1/5} \quad \text{for a turbulent flow ,} \quad (4.2)$$

in which ρ^* , T^* and μ^* are defined assuming thermo-chemical equilibrium conditions at local pressure p and Eckert reference enthalpy h^* :

$$h^* = 0.28h_e + 0.5h_{wall} + 0.22h_{ad.wall} . \quad (4.3)$$

The adiabatic wall enthalpy is given by:

$$h_{ad.wall} = h_0 + (r - 1) \frac{u_e^2}{2} , \quad (4.4)$$

with the recovery factor $r=0.9$ for a turbulent flow and h_0 the total enthalpy of the flow.

The significant overprediction of the measured data by the equilibrium flow assumption tends to confirm the predicted nonequilibrium character of the nozzle expansion process in the HEG facility. Moreover, consistent with indications from the nozzle exit Pitot pressure profile, the nozzle wall boundary layer is most likely turbulent as seen by the important discrepancies between the measured nozzle wall heat flux and the laminar axisymmetric predictions. Comparison with the turbulent predictions, however, hints in the direction that the actual total enthalpy of the flow may be lower than the nominal (theoretically determined from shock tube considerations) value of 21 MJ/kg. This total enthalpy loss due to conduction and radiation in the tunnel reservoir is possible at these high temperature levels attained; their likelihood is further supported by heat transfer data over the Electre model in Section 4.3.

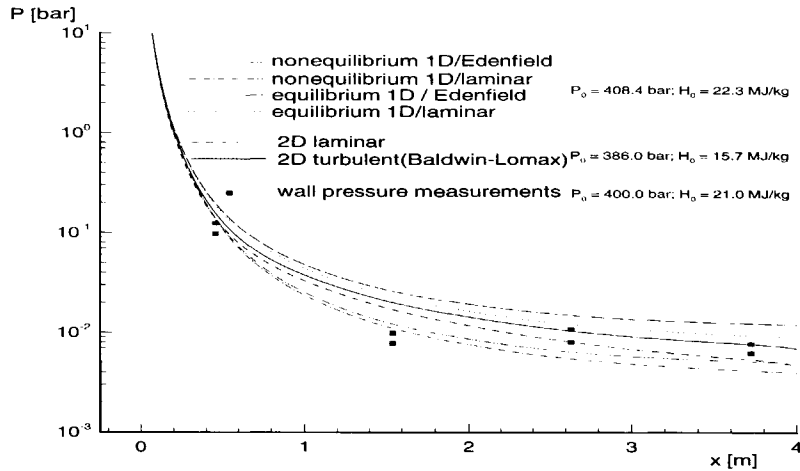


Figure 4.12: Pressure distributions along the HEG nozzle wall.

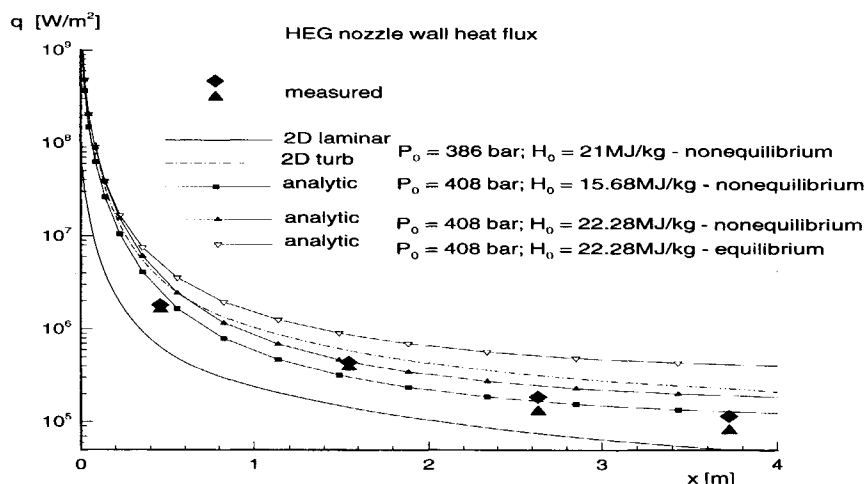


Figure 4.13: Heat transfer distributions along the HEG nozzle wall.

4.3 Standard model Electre

Having noted that Pitot pressure measurements are not sufficiently sensitive to give a complete characterization of the flow field, the Electre standard model was proposed by Papirnyk and Bohl [1992] to provide further insight into the flow exiting the nozzle of high-enthalpy facilities. The measurements over this configuration in the F4 facility and relevant computations have been reported by Masson and Allemane [1995] and Sagnier [1995]; the HEG Electre data have been reported by Krek et al. [1995].

Figure 4.14 shows the shape of the Electre model being a 1/4 scaled model of the Electre re-entry capsule. The Electre re-entry capsule was a sphere-conical body, which has flown in 1971 and 1973 [Sagnier 1992; Walpot et al. 1993; Muylaert et al. 1992]. Figure 4.15 shows the computational grid used for the analysis. The computational domain is discretized accounting for 80x100 grid points, with a smallest wall spacing of 10^{-6} m. For all computations, 30 to 50 points are located in the boundary layer. The difference in temperature between the wall and first cell center at the stagnation line is about 8 to 20 K, which is more than sufficient to get a grid converged solution.

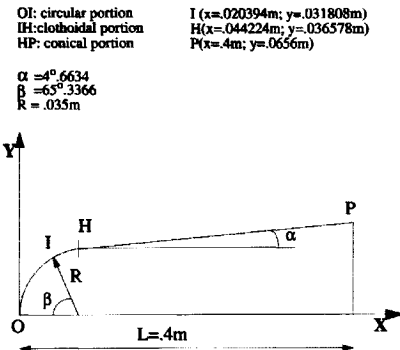


Figure 4.14: Geometrical definition of the shape of the Electre model.

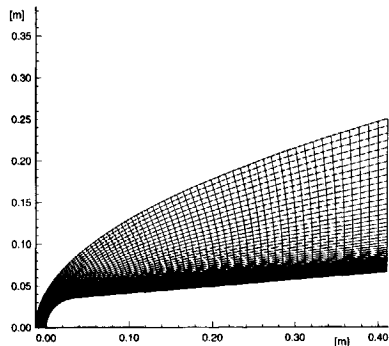


Figure 4.15: Mesh (80x100 grid points) used for the Electre test model.

4.3.1 Electre in the F4 facility

With reference to the normalized pressure distributions over the Electre configuration in F4 flow conditions, depicted in Figure 4.16, it is noted that the best match to the measured pressure distribution is provided by the full equilibrium nozzle-flow assumption, although nonequilibrium flow is assumed around the Electre configuration. This is consistent with the preceding observations from the nozzle wall pressure distribution that the flow expansion along the F4 nozzle is close to equilibrium.

With regard to the heat transfer distributions of Figure 4.17 however, the experiments exhibit a significantly sharper reduction in heat flux around the shoulder of the model than any of the computations and/or assumptions for the nozzle expansion are able to capture. No plausible explanation of these discrepancies has been offered yet. Still, it is noted that the computational results are mesh independent, with typically 30 or more points distributed within the attached boundary layer, and they appear consistent with computations presented independently at the November 1994 ESTEC code validation workshop. The effect of thermal equilibrium/nonequilibrium over Electre was also checked for the melting vibration nozzle flow assumption and was found to be negligible.

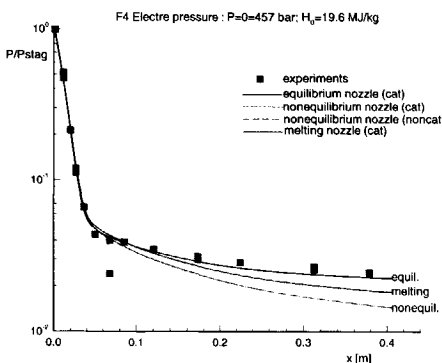


Figure 4.16: Normalized pressure distributions over Electre in the F4 tunnel.

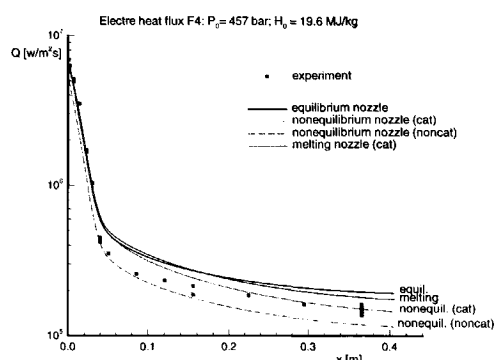


Figure 4.17: Heat transfer distributions over Electre in the F4 tunnel.

4.3.2 Electre in the HEG facility

The nozzle exit conditions used for the Electre model calculations are given in Table 4.3 using three different assumptions in the thermo-chemical modeling.

HEG: 411 bar - 19.97 MJ/kg at nozzle exit $x=3.97\text{m}$ from throat			
chem.	DK	DK	DK
M	10.00	8.03	6.53
$u[\text{m/s}]$	5714.	5723.	5891.
$\rho[10^3 \text{kg/m}^3]$	1.987	1.921	1.881
$p[\text{Pa}]$	449.4	675.7	1087.2
T	686.7	1067.6	1944.3
T_{n2}	3374.7	1067.6	1944.3
T_{o2}	3374.7	1067.6	1944.3
T_{no}	3374.7	1067.6	1944.3
c_{n2}	.7537	.7537	.76401
c_{o2}	.05355	.0530	.1890
c_{no}	.03478	.0347	.01282
c_n	.0	.0	.0
c_o	.15789	.1584	.34065
$p_{t2}[\text{Pa}]$	59434	57766	60504

Table 4.3: HEG nozzle flow exit conditions used for the Electre model calculations.

The Electre pressure and heat transfer distributions measured in the HEG wind tunnel are shown in Figures 4.18 and 4.19 respectively. The measured wall pressures are closer to those obtained when using the melting and equilibrium assumption.

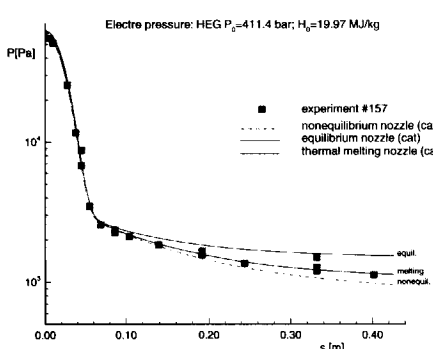


Figure 4.18: Pressure distributions over Electre in the HEG tunnel.

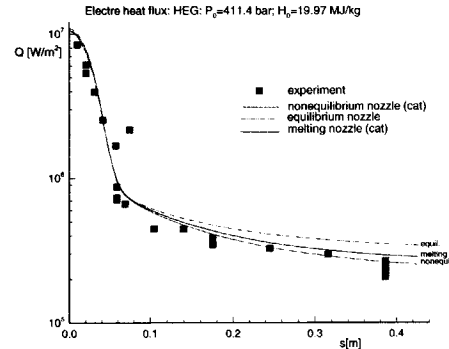


Figure 4.19: Heat transfer distributions over Electre in the HEG tunnel.

With respect to the heat fluxes, depicted in Figure 4.19, an important overprediction of 20%

compared to the measured heat flux in the stagnation region (which is insensitive to the thermo-chemical modeling of the nozzle flow) is observed. This, together with similar observations on the nozzle wall heat transfer distribution, indicates that the actual total enthalpy of the flow is likely to be lower than the nominal value computed from the shock speed.

Taking this into account, the data are normalized with respect to the experimental point closest to the stagnation point, as depicted in Figure 4.20 and 4.21. Here, the scatter in the measurements covers effectively the entire range of the computed results and no definitive conclusions may be drawn as to which nozzle expansion thermo-chemical assumption represents best the test section measurements. However, for the heat flux the experimental points fall largely within the prediction bands rather than being fully biased to the upper or lower prediction limits as in the F4 case (Figures 4.16 and 4.17).

In Figure 4.22 and 4.23 the heat fluxes are plotted for the various models assuming a catalytic and a non-catalytic wall. Clearly it shows that assuming a non-catalytic wall does not match the experimental values and for the catalytic case the band of solutions is smaller than the measured values. It has to be noted that near the sphere-cone junction, between $s=0.6$ m and $s=0.8$ m there are two anomalous heat flux measurements.

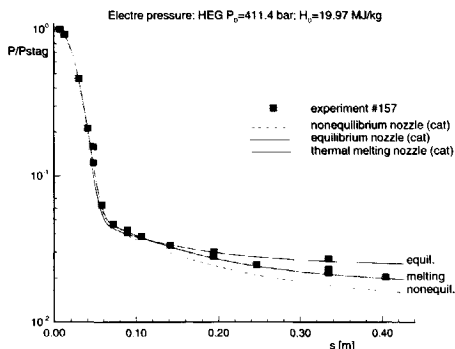


Figure 4.20: Normalized pressure distributions over Electre in the HEG tunnel.

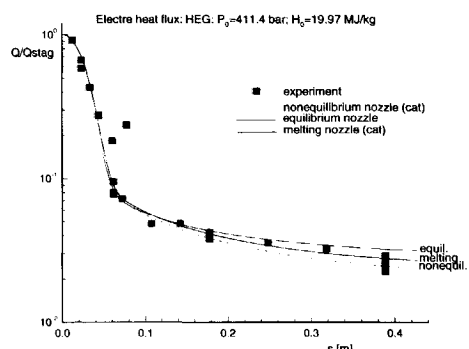


Figure 4.21: Normalized heat transfer distributions over Electre in the HEG tunnel.

4.3.3 Stagnation point heating

The influence of the Lewis number on the Electre heat transfer distribution has been investigated: for the F4 case assuming an equilibrium nozzle expansion using a two-temperature model and for the HEG case assuming a nonequilibrium nozzle expansion using a one-temperature model. With reference to Figure 4.24, the major effect of Lewis number is found in the stagnation region. Specifically, increasing the Lewis number from 1.0 to 1.4 causes an increase in stagnation-point heating of about 8% for the F4 case and 13% for the HEG case.

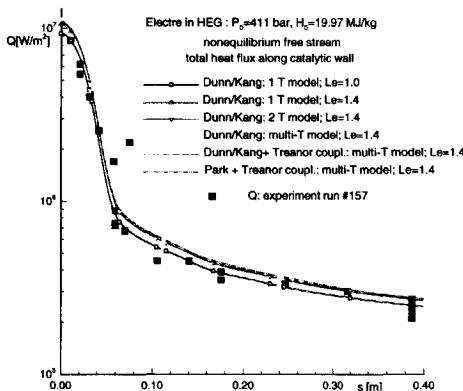


Figure 4.22: Comparison of various thermochemical models over Electre with experiments in HEG assuming a catalytic wall.

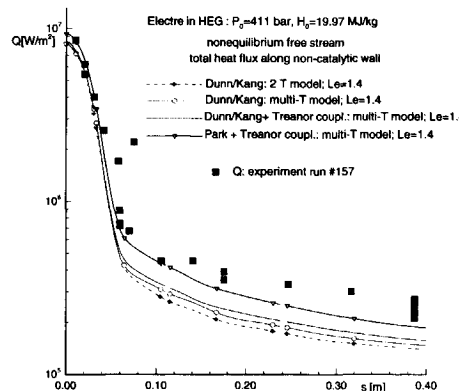


Figure 4.23: Comparison of various thermochemical models over Electre with experiments in HEG assuming a non-catalytic wall.

Measured and predicted stagnation heating values at the Electre stagnation point in F4 and HEG wind tunnel are collected in Table 4.4. In the absence of a stagnation point measurement in the HEG experiment, the quoted measured value has been extrapolated from the first available data point. Predictions include a number of Navier-Stokes computations (for various nozzle expansion assumptions in the Electre cases), semi-empirical estimates from the Fay-Riddell formulation (see Simeonides [1995]) and the correlation of Verant [1994]. The Fay-Riddell estimates assume an equilibrium boundary layer, Newtonian velocity gradient [Bertin 1994] at the stagnation point and a Lewis number of 1.0. For the present purposes of comparison between the measured and computed data of Table 4.4, the Fay-Riddell estimates for Prandtl number of 0.72 (at the ambient wall temperature) are the relevant ones. It should be noted, however, that the original Fay-Riddell formulation has been based on computations for a Prandtl number of 0.76, and the validity of the proposed Prandtl number dependence in this relation has not been confirmed for other values of the Prandtl number.

With reference to Table 4.4 the Fay-Riddell correlation assuming a Prandtl number of 0.6 is seen to be in close agreement with the Verant [1994] estimates; or, put differently, the more appropriate Fay-Riddell estimates, assuming a Prandtl number of 0.72, are some 10% lower than the Verant estimates. In general, the Fay-Riddell results for Prandtl number of 0.72 fall within $\pm 10\%$ of the Navier-Stokes predictions, with the maximum discrepancy in the F4 case where the total enthalpy of the flow has been determined through the Verant formulation. Consequently, the latter shows very good agreement with Navier-Stokes in the F4 case, whereas it also falls within 10% of the Navier-Stokes estimates in the other cases.

Lastly, the experimental data are in reasonable agreement with the theoretical predictions in the F4 case (where the total flow enthalpy is estimated from stagnation point heating measure-

ments). In the HEG the measurements are modestly overpredicted, pointing to the likelihood of significant heat losses in the moderately high pressure, high enthalpy environment in the reservoir.

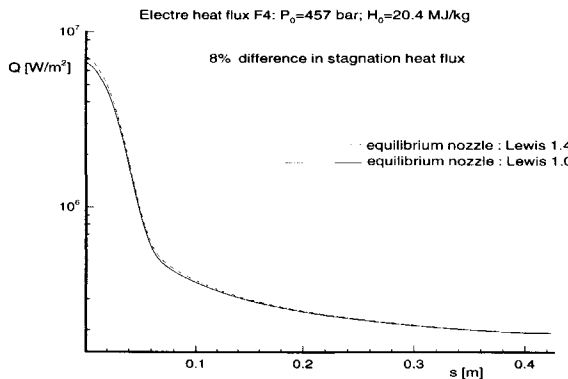


Figure 4.24: Lewis-number effect on heat-transfer distribution over Electre.

Case	Conditions Pitot[bar]- Enthalpy [MJ/kg]	Navier-Stokes computations LORE		measured values	Fay-Riddell Prandtl=	Verant values
		cat	noncat		.6 .72 .9	
Electre in F4 (Lewis =1.) equil. nozzle				.035m nose radius 6.9	6.4 5.7 5.0	6.7
Electre in HEG (Lewis =1.4) noneq. nozzle	.6 - 20	$6.55^4/6.50^6/6.42^7$ $9.4^1/10.7^2/11.0^3$ $10.9^4/11.2^5/10.8^7$	$8.3^1/8.1^2/8.3^3$ $8.1^4/8.4^5/9.3^7$.035m nose radius 9.3	11.6 10.4 9.1	11.6

¹ 1-temp with Dunn and Kang chemistry model, Lewis = 1.

² 1-temp with Dunn and Kang chemistry model, Lewis = 1.4

³ 2-temp with Dunn and Kang chemistry model

⁴ multi-temp with Dunn and Kang chemistry model

⁵ multi-temp with Dunn and Kang chemistry model + Treanor coupling

⁶ multi-temp with Park 87 chemistry model

⁷ multi-temp with Park 87 chemistry model + Treanor coupling

Table 4.4: Measured and predicted stagnation point heating, $\left[\frac{\text{MW}}{\text{m}^2}\right]$.

4.4 Conclusions

Quasi one-dimensional Euler nozzle flows with boundary layer correction and axisymmetric Navier-Stokes nozzle flow computations have been shown to provide an efficient means for the performance of parametric sensitivity studies. Examination of various thermo-chemical nonequilibrium models has shown that the most important differences are found between the Park and Dunn & Kang reaction rate models. In present-day, in moderately high pressure high enthalpy wind tunnels (in contrast to, say, low pressure high enthalpy materials testing facilities) static pressure, temperature and Mach number have been identified as the most sensitive to thermo-chemical behavior, in particular regarding thermal nonequilibrium, full equilibrium and sudden vibrational relaxation effects along the nozzle. Conversely, density, velocity and Pitot pressure have been found insensitive to thermo-chemical effects. High density real gas effects have been shown to be irrelevant at the current levels of operating pressure in high enthalpy facilities.

With respect to the F4 high-enthalpy results, the Pitot pressure indicates that the nozzle wall boundary layer remains far from a fully turbulent developed state over a large part of the nozzle length. The nozzle wall pressure distribution provides some indications that the nozzle-flow expansion in this facility is close to the equilibrium state which is not captured by the nonequilibrium computations. Plausible explanatory hypotheses include vibrational melting triggered by flow contaminants, and insufficiencies of the nonequilibrium models predicting a departure from the equilibrium state at a too early stage along the nozzle expansion. Similar indications are provided by the Electre pressure data in F4, whereas the presently unexplained behavior of the heat transfer measured data calls for a further examination of the accuracy of the measurements. Reduction of flow contamination and non-intrusive flow field measurements are expected to provide further insight into this matter.

Regarding the HEG facility, the Pitot pressure and the nozzle wall heat transfer measurements point to a fully turbulent nozzle wall boundary layer. Furthermore, the heat transfer measurements along the nozzle wall and over the Electre configuration indicate that the prescribed nominal total enthalpy of the flow, computed from the shock speed in the shock tube part of the facility, is higher than the actual flow enthalpy level after losses; the magnitude of these postulated losses is estimated from the available data to be of the order of $25\% \pm 10\%$ of the nominal total enthalpy level. Otherwise, the HEG data tend to support (or, at least, not contradict) the predicted nonequilibrium nozzle flow expansion, although data scatter should be reduced before more decisive conclusions may be drawn.

Finally, with respect to the stagnation point heating analysis, the Fay-Riddell and Verant semi-empirical formulations have been found to provide reasonable estimates of the Navier-Stokes results. Comparison between measurements and predictions again suggests the likely presence of significant heat losses in the reservoir of high enthalpy piston-driven shock tunnels. Concerning the Fay-Riddell formulation, a strong sensitivity to the Prandtl number has been illustrated.

5

Application to three-dimensional re-entry flows

In the previous chapters the governing equations have been outlined and the numerical implementation has been described. The model has been validated on a number of test cases covering a range of hypersonic test cases as shown in Chapters 3 and 4. In addition, the sensitivity of the thermo-chemistry has been scrutinized for high enthalpy wind tunnel testing.

The purpose of this chapter is to demonstrate the applicability for two hypersonic flight vehicles: the Atmospheric Re-entry Demonstrator (ARD) capsule and X-38 Crew Return Vehicle demonstrator. Both vehicles have been tested in “cold” hypersonic wind tunnels and these experimental results will be compared with the CFD predictions. Flight data comparison will be done for the ARD capsule and a flight prediction will be given for the X-38 demonstrator, which will fly late 2003.

5.1 Atmospheric Re-entry Demonstrator

ESA’s Atmospheric Re-entry Demonstrator is Europe’s first complete space re-entry mission. The mission involved launching a vehicle into space by the Ariane 5 launcher and its safe recovery from the Pacific Ocean. A description of the ARD and its mission is given in Section 5.1.1.

The usual methodology for extrapolation to flight has been implemented, by anchoring the start of hypersonic regime on the classical “cold” hypersonic wind tunnel test results. ARD’s aerodynamic and aerothermodynamic pre-flight values, were interpolated between ONERA S4 Mach 10 data and Apollo Mach 30 flight data to the ARD. After the description of the ARD and its mission, the results of the S4 wind tunnel tests as well as available flight data will be compared to numerical simulations in Section 5.1.2 and 5.1.3, respectively.

The S4 pre-flight measurements provide aerodynamic pitching moments versus angle of attack as well as pressure and heat flux measurements. The hypersonic flight data provides

pressure distributions along the symmetry plane and flight angles of attack during entry at conditions spanning the range between Mach 24 and Mach 10.

5.1.1 Background

The ARD is an unmanned, 3-axis stabilized capsule that has been launched on top of the Ariane-503 in 1998 from the European space port at the Guyana Space Center in Kourou, French Guyana. The ARD has an external diameter of 2.80 m, an overall height of 2.04 m and a launch mass of 2753 kg. Its shape is sketched in Figure 5.1 and globally resembles a 70%-scaled Apollo capsule.

The ARD had the following demonstration objectives:

1. validation of theoretical aerothermodynamic predictions,
2. qualification of the design of the thermal protection system and of thermal protection materials,
3. assessment of navigation, guidance and control system performances,
4. assessment of the parachute and recovery system and
5. study of radio communications during atmospheric re-entry (i.e. signal attenuation and black-out phenomena).

After the launch phase, Ariane 503 injected the ARD into a suborbital ballistic path which took it to a maximum altitude of 830 km before re-entering into the Earth's atmosphere. The ARD re-entered the Earth atmosphere at an altitude of 120 km above the Pacific Ocean, at a speed of 7 km/s. The ARD's flight path angle at entry interface was 3 degrees below the local horizontal marking the beginning of the aerodynamic flight phase. In order to reach the landing zone and to keep the deceleration forces and thermal fluxes within the allowable limits, the ARD was automatically guided by the on-board flight control system by using its reaction control thrusters to control its bank angle.

At an altitude between 90 and 80 km, the ARD entered the radiocommunications blackout zone from which it emerged at 45 km. During that part of the trajectory, the Mach number dropped from Mach 25 to Mach 10, as can be seen in Figure 5.2. In this work, the aerodynamic features governing this aerobraking mechanism and the associated aeroheating experienced by the ARD are rebuilt by means of CFD computations and wind tunnel testing.

Eighty eight minutes (5280 sec) after lift-off at altitude of 14 km (see also Figure 5.2), the automatic parachute deployment sequence began with an ejection of the small extraction parachute immediately followed by the opening of the drogue parachute. Seventy eight seconds later, at an altitude of 6 km, the three main parachutes were released for a splashdown at less than 20 km/h sink rate (or vertical speed). Hundred minutes after lift-off, the ARD landed in the Pacific Ocean south-east of Hawaii and north-east of the French Marques Islands. Two balloons were inflated for stability in the water, which completed this momentous mission.

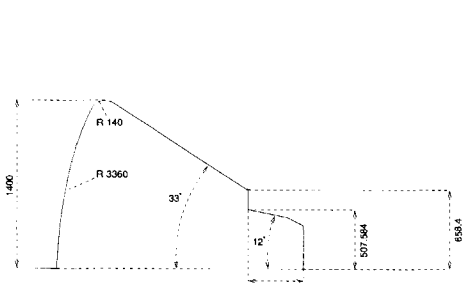


Figure 5.1: Geometrical definition of the shape of the ARD flight vehicle (dimensions in mm).

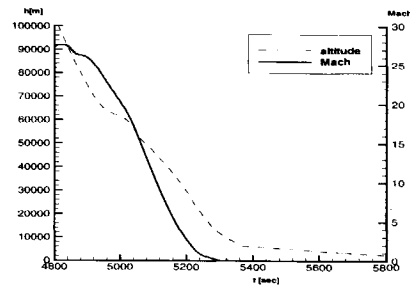


Figure 5.2: The trajectory of the ARD re-entering Earth's atmosphere.

5.1.2 Comparison of results in S4 Modane

The pre-flight experiment was carried out in the S4 hypersonic blow down wind tunnel and is described by Masurel et al. [1996]. The ARD wind tunnel model is a 6.4% scaled down aeroshape of the flight vehicle. Surface pressures, heat flux data and moments were measured on the symmetry plane of the ARD for two different Reynolds numbers at a Mach number about 10. The accuracy in pressure measurements is about 5% and in heat flux measurements about 20%.

The selected flow conditions are obtained under the two different nominal stagnation conditions which yield the nozzle exit flow conditions described in Table 5.1. Since the total temperature is 1151 K, no chemical and hardly any thermal excitation is expected to occur in the flow around the model. Therefore the choice of a perfect gas model seems justified for the computation of the S4 experiment.

$P_0[\text{bar}]$	85.	25
$T_0[\text{K}]$	1151	1108
Re_L	967237	319208
M	9.92	9.72
$P[\text{Pa}]$	211.3	71.17
$T[\text{K}]$	55.7	55.7
$T_{\text{wall}}[\text{K}]$	300.	300.
$L[\text{m}]$.18	.18
$AoA[\text{deg}]$	-20	-20
c.o.g.nominal	$x=.26L, z=.0353L$ from the nose	

Table 5.1: Exit conditions of S4, taken as free-stream for the ARD computations.

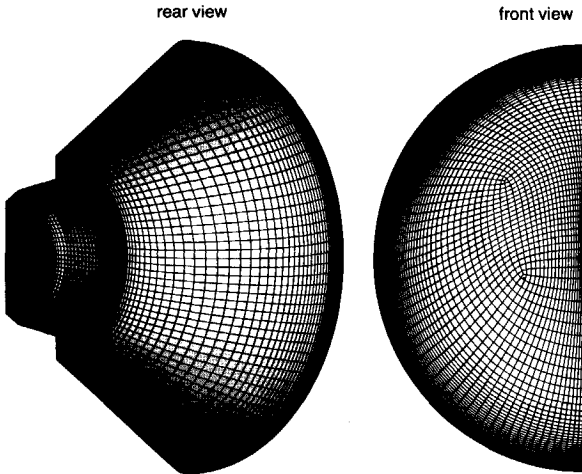


Figure 5.3: ARD surface mesh (fine).

The computational meshes range from coarse to fine with 98 blocks, consisting of 227000, 680000 and 1200000 cells respectively. The surface mesh is shown in Figure 5.3. As a general solution procedure, the coarser-mesh solutions are interpolated on the progressively finer meshes. The size of the smallest normal distance to the wall is $1 \cdot 10^{-5}$ m for the coarse grid and $5 \cdot 10^{-6}$ m for the finer meshes.

The grid does not include the model support, which is acceptable since in the base area the pressure is relatively low (in the order of 10 Pa or less) when compared to the front shield pressure (around 8000 Pa) and therefore should not influence the force measurements significantly.

From the schlieren graph and the oil flow patterns from the S4 tests, the following qualitative assessments can be made:

1. In Figure 5.4, the pressure contour lines in the symmetry plane are plotted together with the extracted shock location of the schlieren graph. It shows that the shock stand-off distance is predicted within the accuracy of the resolution of the schlieren graph.
2. The skin friction pattern in Figure 5.5 is compared with the oil flow pattern on the base of the ARD wind tunnel model. The separated zone on the back is well captured. It must be emphasized here that the point of view between the oil flow picture and the computational result is slightly different since the schlieren graph has been taken at an

unknown incidence close to the horizontal position whereas the computational result has been extracted for this comparison.

This aeroshape is geometrically quite simple but appears to be very difficult to compute. The reason for this is that the complete front heat shield is wetted by a low Mach number flow in the subsonic shock layer. In the vicinity of stagnation regions, disturbances are difficult to damp due to the large difference in magnitude of the eigenvalues of the system. This is more apparent for this case since the whole front area is embedded in subsonic flow. Although, in the present calculations this shortcoming, which many other solvers encounter, is not visible in the pressure and heat flux on the wall. The pressure coefficient contour lines on the surface are plotted in Figure 5.6 where the stagnation point is correctly resolved. The heat flux contour lines on the heat shield are shown in Figure 5.7. The maximum heat flux does not occur at the stagnation point, as referenced by the maximum pressure coefficient contour lines in Figure 5.6, but rather on the toroidal region where the radius of curvature is much smaller than the heat shield radius. The heat flux increase about the shoulder is related to the boundary layer thinning, as the flow accelerates toward the ARD's leeside.

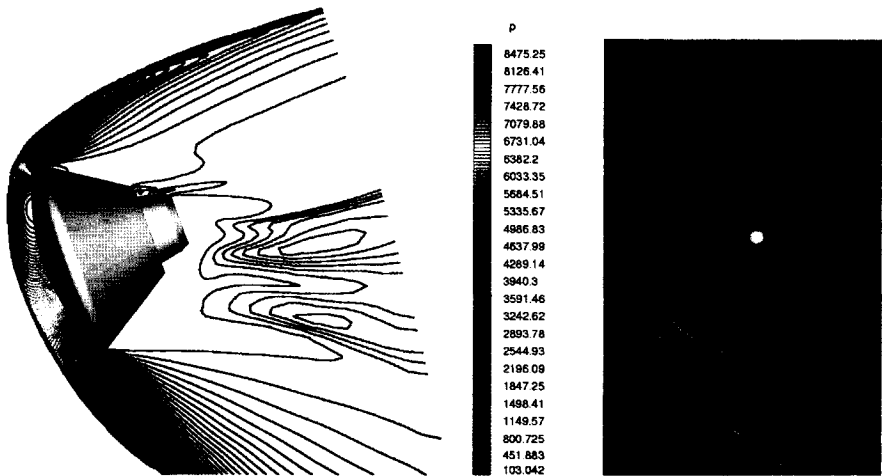
It is of interest to investigate the heat flux increase on the back cover, as plotted in Figure 5.8. It can be noticed that the shape of the back cover has been modified significantly versus the original Apollo shape to ease the support interface to the Ariane 5 launcher. Even though the fluxes in that area are quite small when compared with those of the heat shield, the relatively high levels (25% of the maximum heat flux) are still noticeable.

The heat fluxes on the symmetry plane are plotted in Figure 5.9. For both freestream conditions, the agreement between the experimental and computed heat fluxes is well within the measurement uncertainty of about 20%. The figure also demonstrates that the calculated heat fluxes are grid converged. Despite of the testing condition with a Reynolds number of one million where turbulent flow could occur more likely on the wind ward side than the low Reynolds case, the experimental heat flux is still in agreement with the laminar results.

The pressure coefficient distribution along the symmetry plane of the ARD is shown in Figure 5.10 where S4 data and the computational results for both conditions can be compared. Again the difference between the measured and computed data is well below the 5% measurement uncertainty.

In S4, the pitching moments were measured for various angles of attack. These are compared with the computed Euler and Navier-Stokes solutions in Figure 5.11. The computational results are in good agreement both for the pitching moment values as well as for the prediction of the slope. The viscous effect on the pitching moment is shown to be negligible, but the Navier-Stokes solutions deviate slightly more from the experiments than the Euler results.

Summarizing we were able to compute accurately, within the experimental uncertainty of the measurement, heat fluxes, wall pressures and moments. Since the data generated by the code is validated, the pitching moment data will be used as an anchoring point for the flight calculations in the next section.



(a) Pressure contour lines. The shock location of the schlieren picture is included.

(b) Schlieren graph.

Figure 5.4: Comparison of computed pressure contour lines on symmetry plane and schlieren graph of ARD tested in S4 ($P_0=25$ bar).



(a) Skin friction lines

(b) Oil flow.

Figure 5.5: Comparison of computed skin friction lines and oil flow visualization on the back of ARD in S4 ($P_0=85$ bar).

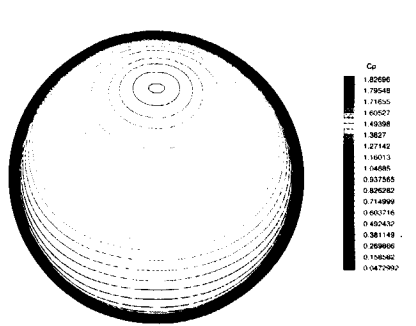


Figure 5.6: Pressure contour lines on heat shield of ARD in S4 ($P_0=25$ bar).

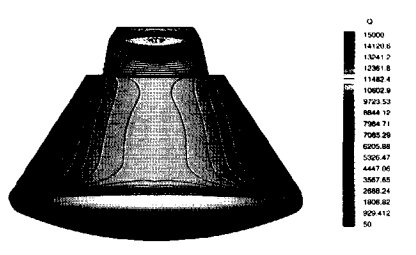


Figure 5.8: Heat flux contour lines on back of ARD in S4 ($P_0=25$ bar).

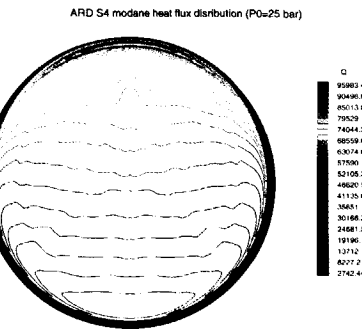


Figure 5.7: Heat flux contour lines on heat shield of ARD in S4 ($P_0=25$ bar).

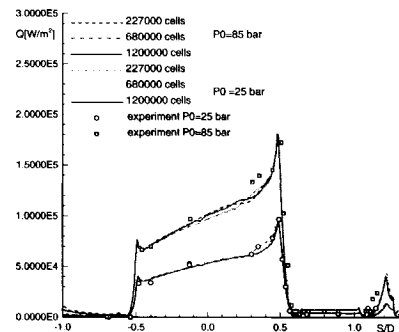


Figure 5.9: Heat flux along symmetry plane of ARD in S4.

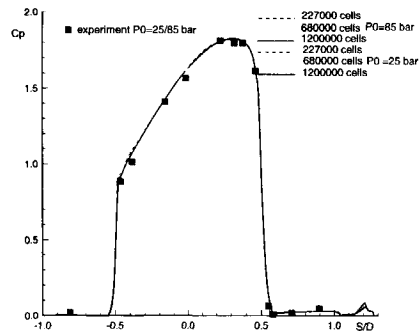


Figure 5.10: C_p distribution along symmetry plane of ARD in S4.

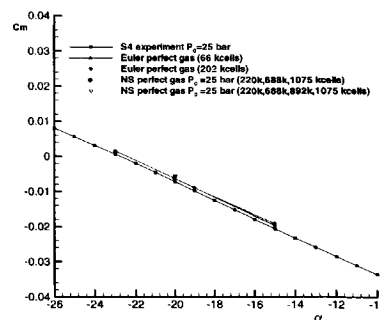


Figure 5.11: Comparison of measured and computed pitching moment of ARD in S4.

5.1.3 Comparison of results with flight data

In this section only pressure coefficients along the symmetry plane and trim angles are available for comparison with the computed results. Perfect gas as well as nonequilibrium calculations have been performed. For the nonequilibrium calculations the Dunn and Kang reaction set comprising 5 species (N_2, O_2, NO, N, O) has been applied. This reaction set was especially designed for Earth re-entry simulations for the RAM flights (see Section 3.3). A two-temperature model has been chosen to model the vibrational energy. The reason to choose for one averaged vibrational temperature instead of a different vibrational temperature for each diatomic species, has two reasons. It will increase the CPU time considerably and the difference on heat flux and pressure on the wall are negligible (see also chapter 4). The wall is assumed to be fully catalytic, although the correctness of this assumption is still debated, it provides a basis for this work. The heat shield material has been out-gassing during re-entry, although only a few millimeters of recession have actually been measured after flight. In addition, the catalytic properties of the heat shield material are poorly characterized and the wall temperature has not been accurately measured during the flight. As a working assumption for all Mach number conditions, a uniform 1500 K wall temperature has been taken, which corresponds roughly to the temperature in flight on the heat shield.

The pressure coefficients on the symmetry plane versus the non-dimensionalized distance from the center of the heat shield calculated under perfect gas and nonequilibrium assumptions for Mach 10, 15, 20 and 24 are shown in Figures 5.12 to 5.15. The error bar in the experimental data does not rule out a perfect gas behavior, even though this fact is questionable since the temperature in the shock layer is high enough to trigger chemical reactions, with Mach numbers as large as 15. This last statement is supported by the nonequilibrium calculations which clearly show a near equilibrium shock layer in the front. In the same figures calculations have been plotted with an angle of attack varying between 19 to 21 degrees to show the shape change pressure distribution. This change in angle of attack can not explain the differences with the flight data.

In Figure 5.16 the trim angles measured in flight are plotted against computed trim angles. The frequency signal on the flight data shows that the ARD oscillates about 1Hz around its trim angle. The trim angle (α_{trim}) from the calculations is obtained by assuming that the ratio (α/α_{trim}) of the respective angles of attack is proportional to the ratio of the angles of the resulting forces on the ARD. It can be written for this ratio [Park and Yoon 1989] that

$$\frac{\alpha}{\alpha_{trim}} = \frac{\tan^{-1} \left(\frac{C_z}{C_x} \right)}{\tan^{-1} \left(\frac{z_{cg}}{x_{cp} - x_{cg}} \right)} \quad (5.1)$$

This equation is expected to work for angles of attack close (< 4 degrees) to the trim angle. This can be verified in Table 5.18 where S4 computations for different angles of attack have been performed.

In the perfect gas solutions, the trim angle is almost constant in the Mach range from Mach

10 until Mach 24. By assuming a perfect gas in this hypersonic regime, the resulting bow shock location is not influenced by the flight conditions in that range and so is the pressure distribution on the heat shield. Note that mainly the front shield contributes to the pitching moment, since in the rear part the pressures are relatively much lower and therefore their contribution to the pitching moment can be neglected.

In contrast, thermo-chemistry will change the bow shock location and should account for the phenomena encountered to better fit the increase of the trim angle with increasing Mach number. The best fit between computed and flight data is achieved by using the nonequilibrium assumption, with the nominal center of gravity (cg) location. A small shift of the center of gravity (ΔZ_{cg} of .5 cm or a ΔX_{cg} of 8 cm, still within the design specifications) suffices to fit the mean values of the hypersonic flight data (see Figure 5.17).

5.1.4 Conclusion

It has been shown that numerical simulations on the hypersonic aerodynamic characteristics of a capsule reentering earth atmosphere can be obtained by using the CFD code described in this thesis. Cold gas facilities like S4 provide an excellent mean of validating the CFD code. The simulated aerodynamics and aeroheating of the wind tunnel test cases is well below the experimental uncertainty band.

The extrapolation to flight conditions from cold to hot using CFD appeared to be adequate to simulate the change in pitching moment due to high temperature effects. For the re-entry vehicle, the trim angles could be calculated, within the uncertainty of the measurements. These uncertainties are dominated by the exact location of the center of gravity and by the input parameters to describe the aerothermodynamic conditions. Different atmospheric models can be used to yield different free-stream conditions above 50 km. The influence of the latter on the simulations has not been examined. In addition because of the unclear wall properties, such as the wall temperature, catalycity and out-gassing, no attempt is made to compare heat fluxes with flight values. It is expected that improvements in future flight measurements and the proper characterization of the wall properties will further enhance the understanding of the differences between CFD prediction and flight data.

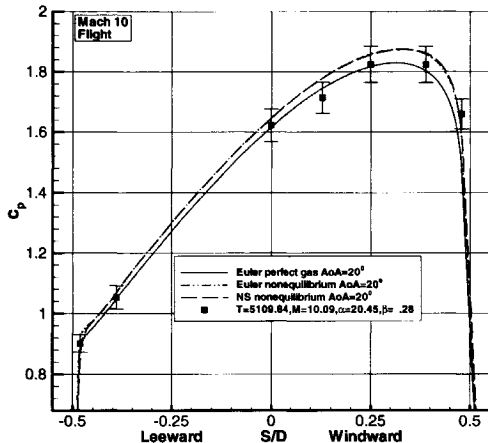


Figure 5.12: C_p distribution along symmetry plane of ARD heat shield in flight Mach 10.

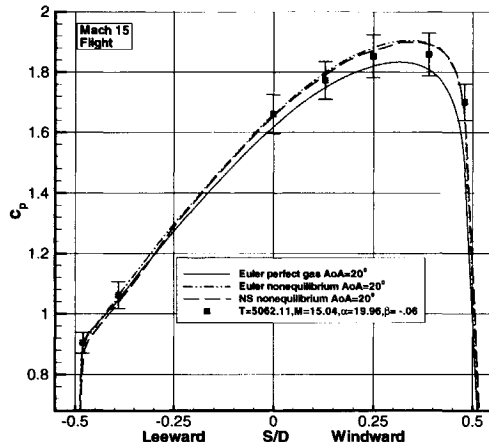


Figure 5.13: C_p distribution along symmetry plane of ARD heat shield in flight Mach 15.

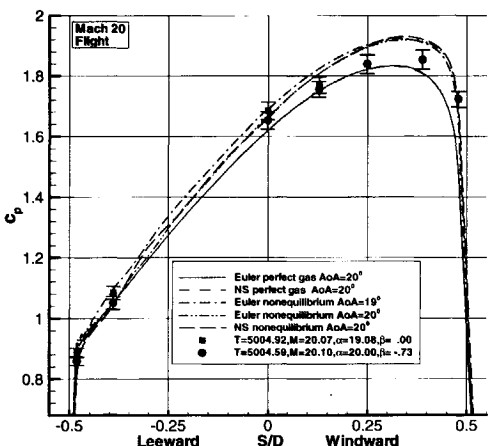


Figure 5.14: C_p distribution along symmetry plane of ARD heat shield in flight Mach 20.

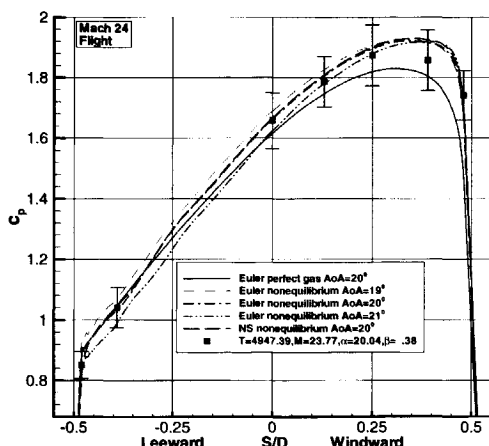


Figure 5.15: C_p distribution along symmetry plane of ARD heat shield in flight Mach 24.

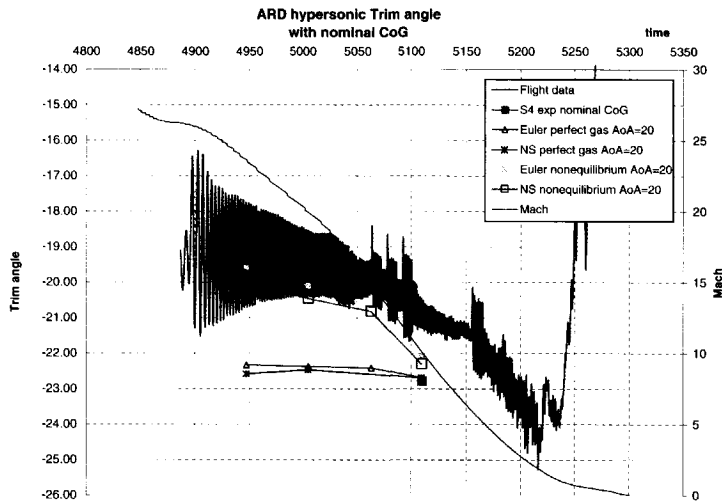


Figure 5.16: Comparison of computed and measured trim angle with nominal c.o.g.

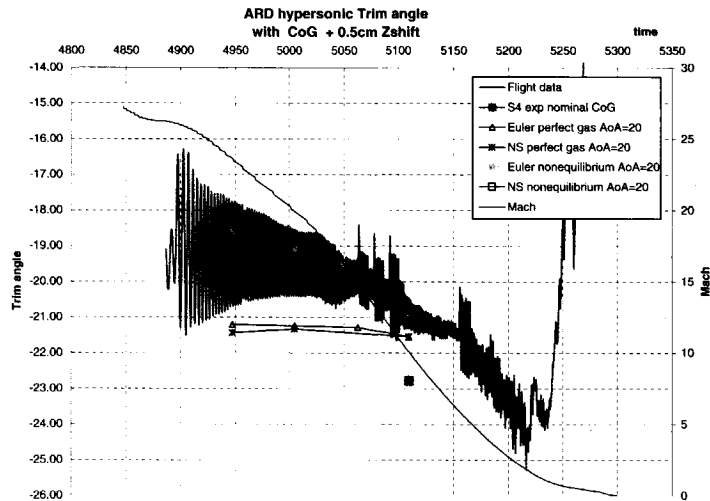


Figure 5.17: Comparison of computed and measured trim angle with offset of .5cm in Z direction.

		cells	grid	α	Ma	Re	CX	CZ	CL	CD	CMcog	L/D	α trim
S4-EULER													
coarse	EUL-PG	27630	-15	10	Inf		1.388370	-0.050494	0.408110	1.327994	-0.019556	0.3073	-24.94
coarse	EUL-PG	27630	-19	10	Inf		1.340774	-0.067488	0.500324	1.245755	-0.008903	0.4016	-23.39
coarse	EUL-PG	27630	-23	10	Inf		1.283764	-0.086113	0.580874	1.148064	0.001464	0.5060	-22.28
Medium	EUL-PG	221040	-15	10	Inf		1.391657	-0.048038	0.406588	1.331804	-0.019090	0.3053	-24.52
Medium	EUL-PG	221040	-19	10	Inf		1.345180	-0.064941	0.499351	1.250750	-0.008964	0.3992	-23.41
Medium	EUL-PG	221040	-23	10	Inf		1.288060	-0.085344	0.580004	1.153100	0.001515	0.5030	-22.26
S4-LOW													
Coarse	NS-PG	66350	-19	10	3.2E+05		1.342740	-0.072941	0.506120	1.245838	-0.008453	0.4062	-23.11
Medium	NS-PG	530800	-19	10	3.2E+05		1.346998	-0.069816	0.504552	1.250882	-0.008758	0.4034	-23.28
coarse	NS-PG	224064	-20	10	3.2E+05		1.329430	-0.074289	0.524501	1.223847	-0.006014	0.4286	-22.93
medium	NS-PG	688824	-20	10	3.2E+05		1.332494	-0.072431	0.523803	1.227362	-0.005807	0.4268	-22.81
fine	NS-PG	1075095	-20	10	3.2E+05		1.332637	-0.072426	0.523847	1.227498	-0.005796	0.4268	-22.80
S4-HIGH													
coarse	NS-PG	224064	-20	10	9.7E+05		1.318611	-0.074245	0.520759	1.213696	-0.005444	0.4291	-22.64
medium	NS-PG	688824	-20	10	9.7E+05		1.327915	-0.072394	0.522202	1.223072	-0.005868	0.4270	-22.86
fine	NS-PG	892143	-20	10	9.7E+05		1.331087	-0.071204	0.522168	1.226459	-0.005736	0.4258	-22.77
superfine	NS-PG	1075095	-20	10	9.7E+05		1.331438	-0.070889	0.521992	1.226897	-0.005574	0.4255	-22.68
MACH10 5109,84													
coarse	EUL-PG	34506	-20	10	Inf		1.327618	-0.070972	0.520764	1.223279	-0.005277	0.4257	-22.53
medium	EUL-PG	276048	-20	10	Inf		1.330588	-0.069801	0.520679	1.226470	-0.005543	0.4245	-22.67
fine	EUL-PG	443646	-20	10	Inf		1.332040	-0.070223	0.521573	1.227690	-0.005595	0.4248	-22.70
coarse	EUL-NE	34506	-20	10	Inf		1.369255	-0.075254	0.539288	1.260941	-0.005011	0.4275	-22.31
medium	EUL-NE	276048	-20	10	Inf		1.371318	-0.073646	0.538223	1.263429	-0.004792	0.4260	-22.19
fine	EUL-NE	654336	-20	10	Inf		1.371207	-0.073555	0.538100	1.263356	-0.004628	0.4259	-22.11
medium	NS-PG	688824	-20	10	1.2E+06		1.328069	-0.072212	0.522083	1.223279	-0.005756	0.4268	-22.79
fine	NS-PG	1075095	-20	10	1.2E+06		1.330905	-0.070763	0.521692	1.226439	-0.005578	0.4254	-22.69
coarse	NS-NE	224064	-20	10	1.2E+06		1.367702	-0.075884	0.539093	1.259264	-0.004851	0.4281	-22.23
medium	NS-NE	688824	-20	10	1.2E+06		1.372130	-0.074999	0.539772	1.263729	-0.004980	0.4271	-22.29
fine	NS-NE	1075095	-20	10	1.2E+06		1.373251	-0.076013	0.541108	1.264436	-0.005033	0.4279	-22.31
MACH15 5092,5													
coarse	EUL-PG	34506	-20	15	Inf		1.322886	-0.070484	0.518687	1.218999	-0.005071	0.4255	-22.43
medium	EUL-PG	276048	-20	15	Inf		1.325346	-0.069344	0.518457	1.221701	-0.005036	0.4244	-22.41
fine	EUL-PG	443646	-20	15	Inf		1.326320	-0.069133	0.518592	1.222681	-0.005069	0.4241	-22.42
coarse	EUL-NE	34506	-20	15	Inf		1.378396	-0.076369	0.543203	1.269149	-0.000776	0.4280	-20.32
medium	EUL-NE	276048	-20	15	Inf		1.381947	-0.075709	0.543797	1.272711	-0.001703	0.4273	-20.72
fine	EUL-NE	654336	-20	15	Inf		1.382759	-0.075444	0.543826	1.273565	-0.001637	0.4270	-20.69
medium	NS-NE	116352	-20	15	6.9E+05		1.370333	-0.080133	0.543984	1.260299	-0.002215	0.4316	-20.96
fine	NS-NE	930816	-20	15	6.9E+05		1.375614	-0.078599	0.544347	1.265772	-0.001937	0.4301	-20.83
MACH16 5050													
fine	EUL-NE	654336	-20	16	Inf		1.385862	-0.075265	0.544719	1.276542	-0.001307	0.4267	-20.55
MACH20 5005													
coarse	EUL-PG	34506	-20	20	Inf		1.322585	-0.071163	0.519222	1.218484	-0.004988	0.4261	-22.39
medium	EUL-PG	276048	-20	20	Inf		1.325320	-0.069844	0.518463	1.220707	-0.004949	0.4247	-22.36
fine	EUL-PG	443646	-20	20	Inf		1.325694	-0.069608	0.518924	1.221938	-0.004988	0.4246	-22.38
coarse	EUL-NE	34506	-20	20	Inf		1.405937	-0.070857	0.524725	1.306271	-0.003144	0.4017	-20.28
coarse	EUL-NE	34506	-20	20	Inf		1.380934	-0.075979	0.543704	1.271667	-0.000764	0.4276	-20.32
medium	EUL-NE	276048	-20	20	Inf		1.388098	-0.075285	0.545503	1.278637	-0.000511	0.4266	-20.21
fine	EUL-NE	654336	-20	20	Inf		1.389617	-0.075218	0.545959	1.280087	-0.000254	0.4265	-20.10
coarse	NS-PG	224064	-20	20	3.5E+05		1.325428	-0.075388	0.524165	1.219711	-0.005307	0.4297	-22.55
medium	NS-PG	688824	-20	20	3.5E+05		1.325906	-0.072347	0.521471	1.221200	-0.005250	0.4270	-22.52
fine	NS-PG	1075095	-20	20	3.5E+05		1.325917	-0.071938	0.521090	1.221350	-0.005145	0.4267	-22.46
fine	NS-NE	1075095	-20	20	3.5E+05		1.390053	-0.078227	0.548935	1.279467	-0.001113	0.4290	-20.46
MACH24 4947													
coarse	EUL-PG	34506	-20	24	Inf		1.321669	-0.071126	0.518874	1.217636	-0.004825	0.4261	-22.30
medium	EUL-PG	276048	-20	24	Inf		1.324265	-0.069858	0.518587	1.220509	-0.004893	0.4249	-22.33
fine	EUL-PG	443646	-20	24	Inf		1.324845	-0.069613	0.518538	1.221138	-0.004909	0.4246	-22.34
coarse	EUL-NE	34506	-20	24	Inf		1.380347	-0.075439	0.542996	1.2713	0.000447	0.4271	-19.82
medium	EUL-NE	276048	-20	24	Inf		1.388415	-0.074952	0.545298	1.279048	0.000878	0.4263	-19.65
fine	EUL-NE	654336	-20	24	Inf		1.391109	-0.075078	0.546338	1.281537	0.001029	0.4263	-19.59
fine	EUL-NE	654336	-19	24	Inf		1.40787	-0.070624	0.525134	1.308174	-0.002058	0.4014	-19.82
fine	EUL-NE	654336	-22	24	Inf		1.362927	-0.080957	0.574838	1.23842	0.005169	0.4642	-19.42
coarse	NS-PG	224064	-20	24	1.9E+05		1.324955	-0.075244	0.523865	1.219315	-0.005311	0.4296	-22.56
medium	NS-PG	688824	-20	24	1.9E+05		1.324763	-0.075166	0.523729	1.219162	-0.005414	0.4296	-22.61
fine	NS-PG	1075095	-20	24	1.9E+05		1.32647	-0.073949	0.523169	1.221182	-0.005361	0.4284	-22.58

Figure 5.18: Grid convergence effect on aerodynamic loads on ARD.

5.2 X-38 flight predictions

In the previous section a semi-ballistic re-entry of a capsule is simulated. The purpose of this section is to demonstrate typical aspects of hypersonic aerothermodynamic characteristics encountered for the X-38 lifting body. This vehicle generates its aerodynamic lift from its shape. The fins and control surfaces are added to stabilize and control the vehicle. The vehicle was found to be trimmed at 40 degrees angle-of-attack with approximately 15 degree body flaps at a corresponding L/D of .9. First, we give an overview on the evolution of the development of the X-38 aerodynamic shape to meet its mission requirements. Second, the heat fluxes of cold hypersonic wind tunnel tests are compared with CFD results to validate the prediction capability of the present code. After this validation, the heating during re-entry in the nose region is assessed using different wall catalysis assumptions. Third we assess the high temperature effects occurring during the hypersonic re-entry on pitching moments. This is achieved through nonequilibrium flight simulations as well as using freon as test gas to simulate the γ effects occurring in high enthalpy flows.

5.2.1 Background

In 1992, NASA JSC (Johnson Space Center), intended to provide an emergency evacuation capability from the ISS (International Space Station) to earth in the event of medical or mechanical problems and Shuttle non-availability.

Several configurations or aeroshapes have the potential to fulfill this Crew Return Vehicle (CRV) mission: capsule, lifting body or a mini shuttle, ranging from low to high cross range capabilities. Capsule-shaped vehicles however, have several recognized shortcomings with respect to the mission requirements. For example with the present Soyuz capsule, due to its low cross range capability, astronauts might have to wait as long as 18 hours in orbit for recovery close to an existing facility. It involves additional costs for landing close to an existing facility. In addition it involves additional costs for the recovery within a 300 km radius of the predicted landing site. Also, Soyuz can only accommodate a crew of 3 instead of the 7 ISS crew members agreed by the the international ISS partners.

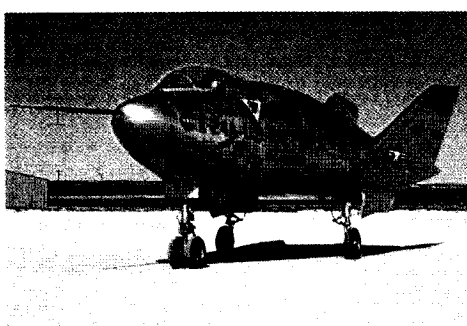
Scaling the Space Shuttle into a mini-shuttle is not straightforward. The heating increases proportionally to the inverse of the square-root of the vehicle size whereas the landing speed increases with the square of the inverse of the vehicle size. Practical landing speeds are limited to 113 m/s for tire integrity. It would require considerable changes in the design and its associated trajectory. It requires also the maintenance of long runway landing facilities.

Highly maneuverable entries with over 3800 km cross-range are possible with X-24B-like configurations. For non-military entry missions (space station return, space-rescue, etc.), where payload fraction is more important than cross-range, all lifting body concepts with entry L/D's of 0.9 to 1.4 are of interest. A lifting-body design would allow the lifeboat to fly during re-entry to a landing site, within a 1100 km cross range. To keep landing speed low of a lifting body, the vehicle would have to be either lighter or larger in size for the same weight.

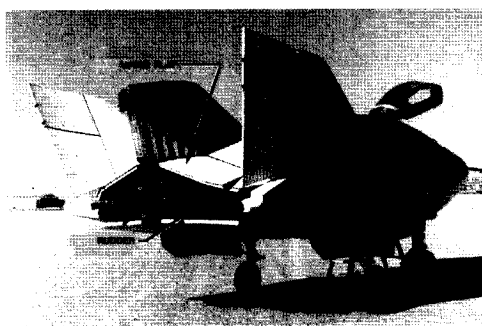
However, a larger lifting body would not be compatible with Ariane 5 or Space Shuttle cargo bay capability.

To circumvent the problems arising from the high landing speed of lifting body configurations, the use of a large parafoil has been proposed to reduce landing speeds to as low as 60 km/h offering the potential for off-runway landings around the world: after the vehicle has decelerated to subsonic speed at about 6 km altitude, a series of parachutes are deployed, followed by a large, rectangular-shaped, steerable gliding parafoil.

NASA JSC selected in 1992 the tried-and-proven lifting body SV-5 outer mold line (X-23/X-24) as the basis for the CRV development programme (although the aero- and aerothermo databases generated from these vehicles were never used for the new vehicle). The SV-5 was designed for the US Air force, as an alternative to the ballistic re-entry concepts, in the early sixties by Hans Multhopp of the Martin Aircraft Company. (As an aeronautical engineer, he worked during World War II for the Focke-Wulf Flugzeugbau in Bremen). The SV-5 shape was the only lifting body that had been proven in flight from near-orbital speeds to horizontal landing. The unpiloted X-23 (or SV-5D) see Figure 5.20, developed under the PRIME program (Precision Recovery Including Maneuvering Entry) had demonstrated maneuvering flights from orbital speeds down to Mach 2. This vehicle was a 400 kg aluminum vehicle with an ablative heat shield launched by an Atlas booster. At a high point in flight, the booster pitched downward while accelerating by the rocket to reach the required high re-entry speeds. The vehicle was separated and performed a full hypersonic entry from Mach 25 to Mach 2. After a parachute opened, the vehicle was recovered by an airplane. The X-24A (or SV-5P) developed under the program PILOT (Piloted Low speed Tests) had demonstrated flight from Mach 2 to subsonic landing speeds. On 11 July 1967, Martin rolled out the X-24A at its plant in Baltimore, Maryland.



(a) front view



(b) rear view showing subsonic control surface configuration

Figure 5.19: X-24A lifting body.

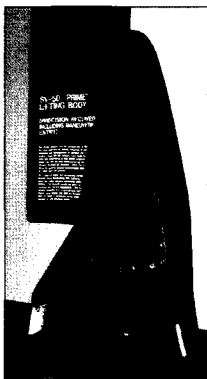


Figure 5.20: X-23 hypersonic lifting body.

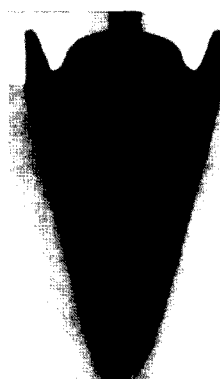


Figure 5.21: YPA01 wind tunnel model.

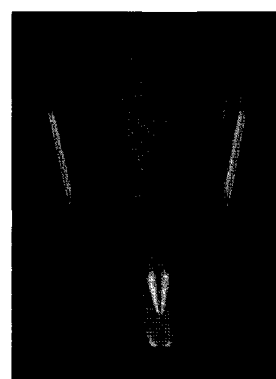


Figure 5.22: YPA02 configuration.

As a demonstrator for the CRV, the current X-38 is based on the X-24A through modification of the upper side the the vehicle. The windward side, dominating the hypersonic flight performance, has never been changed because its shape had proven to be successful with the X-23.

The original shape has been evolved in three main stages/modifications:

1. the NASA modifications resulting in the so-called X-38 Revision 3.1, see Figure 5.23,
2. the YPA shape designed by CNES-ESA, see Figure 5.21 and 5.22,
3. finally, the X-38 8.3 shape by Dassault-Aviation and NASA.

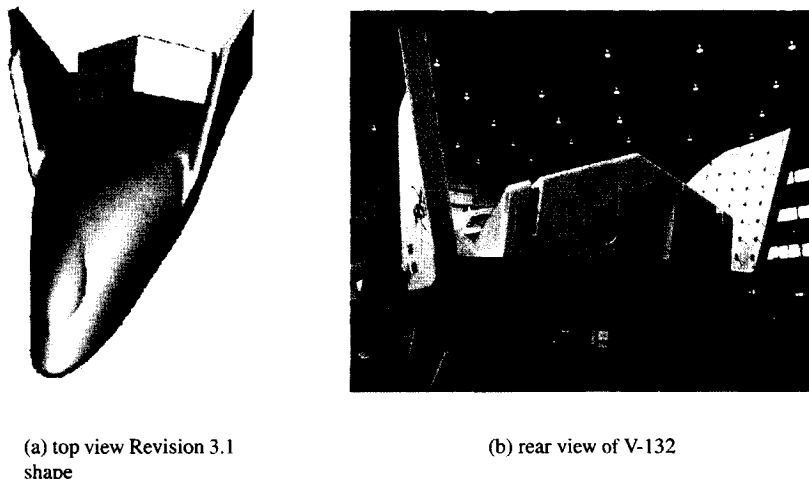
The main changes are summarized below:

1. Revision 3.1 V-131 and V-132 (1992-1996)

NASA JSC started from X-24A with an unchanged scale (7.32 m long). The central fin was removed, as well as the XLR-11 rocket engines. The upper aft flaps were fixed to 13 degrees angle. The base was filled and a chamber in the base was made to accommodate the drogue chute. Two vehicles have been built and dubbed V-131 and V-132 respectively. (see Figure 5.23) V-131 was built to assess the separation sequence from the B-52 as well as the parafoil opening sequence with a representative vehicle. The primary goal of the V-132 was to demonstrate the flight control systems using Electro Mechanical Actuators and Honeywell MACH control laws technology. V132 was successfully flight-tested on March 5, 1999 and July 9, 1999.

2. YPA shape (1996-1997)

To increase the useful volume i.e., payload of the X-24A, the length was scaled by



(a) top view Revision 3.1
shape

(b) rear view of V-132

Figure 5.23: X-38 Revision 3.1

120% and the height by 140%, while keeping the canopy at the same level. The canopy had to stay for political reasons, since there was never an intention to have a window for piloting, and was consequently embedded into the fuselage for a smoother shape. The central fin was removed (also not present in the X-23 configuration), the upper aft flaps were removed on the leeward side and replaced by a cylindrical tube from the maximum cross section half way of the vehicle till the aft. This increase in volume also allowed for the compatibility with an launch atop an ELV (Expendable Launch Vehicle). The fins were cut by 50% and the 12 degree flare was disposed off to fit in the Shuttle cargo bay. Also, only the upper rudders on the fins were kept. This resulted in the YPA01 shape, but the resulting lateral stability was very poor over the entire flight range. In addition transonic tests around trim angles between 10 and 20 degrees angle-of-attack in the NLR HST wind tunnel revealed an alternating stable-unstable-stable pattern for the longitudinal stability which also exhibited a high degree of hysteresis. This behavior was traced back to the erratic behavior of a strong vortex between the fins and the fuselage. In an attempt to alleviate this behavior, the gaps in between were filled. This shape was dubbed YPA02 and longitudinal stability was retrieved to the detriment of lateral stability. Lateral stability was recovered in shape YPA03 by removing the gap fillets, introducing a junction fillet at the root of the empennage and increasing fins' height. To accommodate the vehicle in the Shuttle, a folding mechanism for the fins was required and implemented.

3. X-38 8.3 (1997)

The shape Revision 3.1 was modified by Dassault-Aviation and NASA. Much along

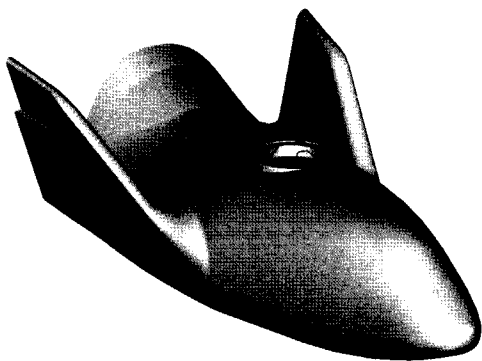


Figure 5.24: X-38 8.3 shape.

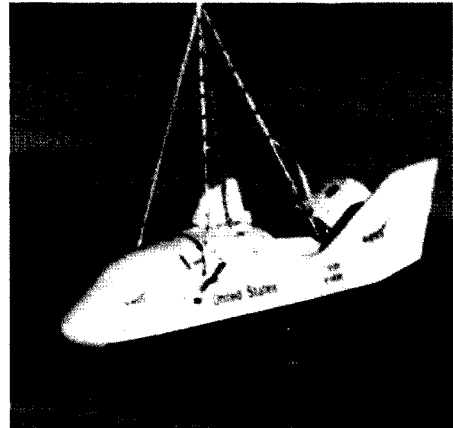


Figure 5.25: V-131R vehicle.

the lines of the YPA modifications, the aft part was increased and rounded to allow for launch capability atop of an ELV. A second ramp was introduced on the aft: wind tunnel tests prompted the need for such a modification to trim the vehicle in the transonic regime between 10 and 17 degrees angle-of-attack, in order to provide for aileron capability at 15 degrees angle-of-attack with 20 degrees body flap setting. Also the high lift devices at the leading edge tips, called droops, were removed, and a junction fillet at the root of the fins was added to increase the longitudinal stability in the transonic/subsonic regime. In addition, the inner part of the fins was straightened.

V-131 was refurbished into the new 100% V-131R configuration and equipped with active control surfaces. The first (unsuccessful) drop test of V-131 took place on November 2000.

The X-38 CRV technology demonstrator full re-entry mission, designated as V-201, will be planned late 2003. It has the X-38 8.3 configuration shape scaled 120% (8.7 meter long). In order to fit into the Orbiter's cargo bay, the upper parts of the fins are foldable. After jettisoning of the deorbit engine module, the X-38 will return unpowered and then use a steerable parafoil for the final part of descent and landing. Landing will be accomplished on skids.

5.2.2 Windward surface heating validation

The primary objective of the SV5-D project was to assess aerodynamic performance through flight testing during hypersonic re-entry. With the emphasis placed on aerodynamics, a detailed heating database was never produced. Ground based tests in the AEDC tunnel C and the Martin hot shot tunnel at Mach 20 [Screen and Nickel 1965; Rhudy and Merz 1965] proved to be sufficiently accurate for a conservative heat shield design, using ablative materials over the entire vehicle.

In order to setup an aerothermodynamic database for the X-38 program, measurements of aerodynamic characteristics were conducted in LaRC 20-inch Mach 6 Tunnel and 31-inch Mach 10 tunnel, primarily to use for validation of CFD tools, but also to assess quantitatively the effects of Reynolds number ($Re_L = 1, 2, 4$ and $5 \cdot 10^6$), angle-of-attack, boundary layer transition and configuration changes on heating, boundary layer transition and configuration changes on lee-side heating.

In this section we compare the heat flux measurement on the windward side of the X-38 model with a body flap deflection of 20 degrees in the LaRC 20-Inch Mach 6 tunnel. This tunnel, which became operational in 1958, is a blow down wind tunnel that uses dry air as the test gas. The wind tunnel was very active in configuration testing at the climax of interest in hypersonics in the late 1950's and 1960's and has remained active to the present.

The heat fluxes were measured with a thermo-phosphor paint and have an accuracy of 20%. The model length (10 inch) is determined by the facility core section size yielding scale factor of 2.95%. In Table 5.2 the freestream conditions of the wind tunnel are given.

M	$Re[L=2481681\text{m}]$	AoA	T [K]	$\rho[\text{kg}/\text{m}^3]$	U [m/s]
6	944479	40°	59.62	$1.6176 \cdot 10^{-2}$	928.89

Table 5.2: Freestream conditions of the LaRC Mach 6 wind tunnel

For this comparison, coarse, medium and fine meshes have been created with 118302, 946416 and 1569727 cells respectively. A side view of the medium mesh can be seen in Figure 5.26. The corresponding pressure contour plot on the body and symmetry plane is depicted in Figure 5.27. The convergence history for the pitching moment coefficient and L2 norm of the density equation are shown in Figure 5.28. First the coarse mesh is converged, then the solution is interpolated on the medium mesh and the computation is restarted, and similarly for medium to fine mesh. The residuals are normalized with the maximum value for each mesh. In addition one can see that the nose down pitching moment converges to a constant value of -0.0221 for both medium and fine mesh.

In Figure 5.29 the heat flux on the windward side is compared with those obtained from wind tunnel tests. The contour lines agree qualitatively very well with the topology of the heat flux mapping, except on the body flap where the flow re-attaches after the separation

bubble around the hinge of the flap. For the laminar simulation the heat fluxes are too low compared to the measured values. To see the effect of a forced transition, a Baldwin Lomax turbulence model is applied starting from the hinge of the flap. The result of this calculation, in Figure 5.30, shows an overall better agreement with the experiment.

A quantitatively comparison of the heat fluxes on the symmetry plane and a cut parallel to the symmetry plane are shown in Figures 5.31 and 5.32. One has to notice that there is a gap between the body flap and the symmetry plane, such that the heat fluxes at the end in the symmetry plane are taken in the cavity behind the flap. The difference between the heat fluxes predicted by the medium and fine meshes on the body is smaller than the uncertainty of the experiment. Also one can see that the separation point, where the heat flux suddenly drops at $x= .208$ m, is captured within the measurement uncertainty. Applying the Baldwin-Lomax model starting at the hinge cannot predict re-attachment line, but the difference of the heat fluxes is less than 10%.

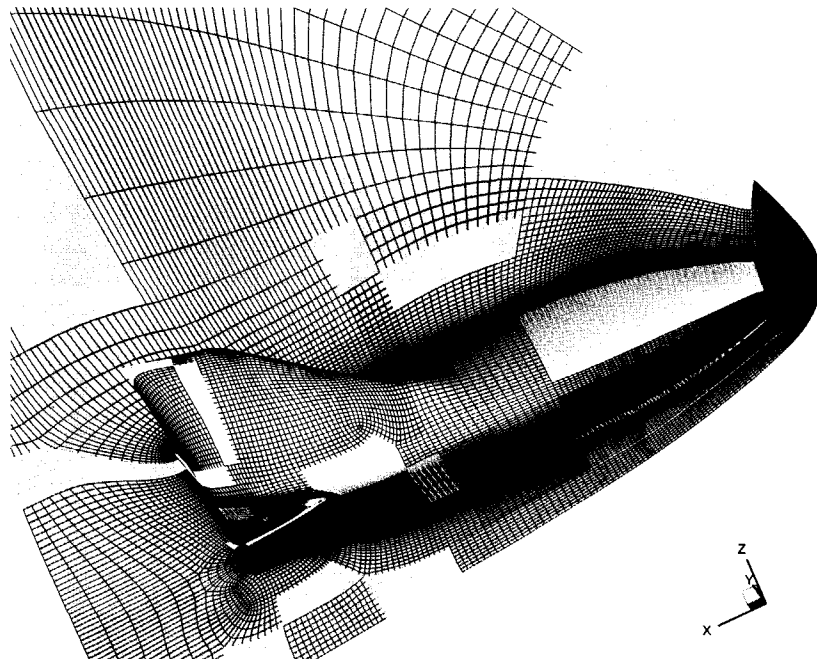


Figure 5.26: X-38 medium mesh containing 421 blocks and 946,416 cells

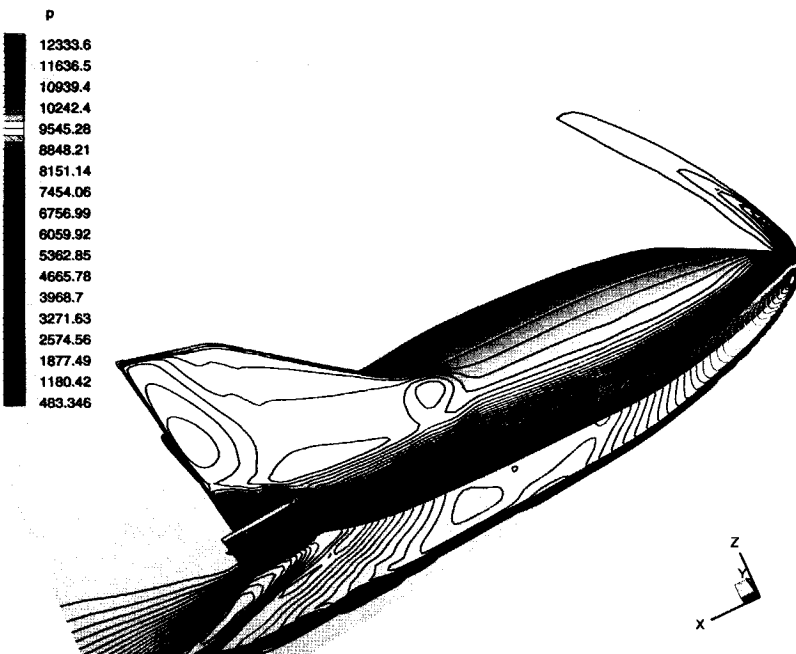


Figure 5.27: Pressure contour lines on X-38 in LaRC

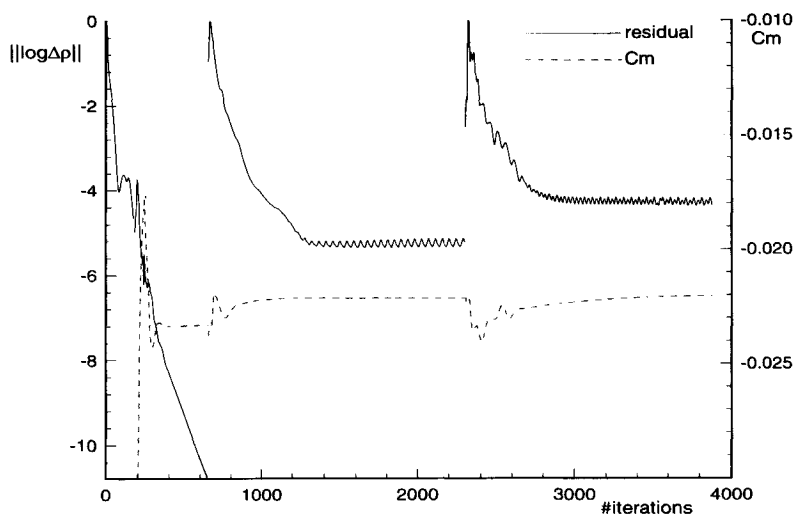


Figure 5.28: Residual of the three mesh refinements of X-38 in LaRC

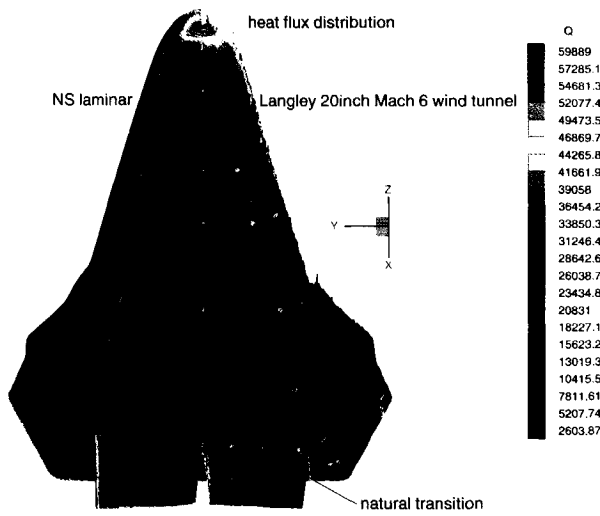


Figure 5.29: Comparison of heat flux distribution between computed laminar solution and measurements in the LaRC wind tunnel.

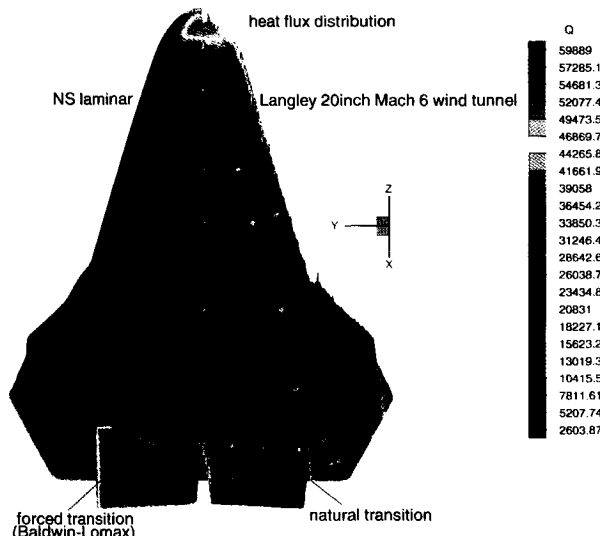


Figure 5.30: Comparison of heat flux distribution between computed laminar solution with forced transition and measurements in the LaRC wind tunnel.

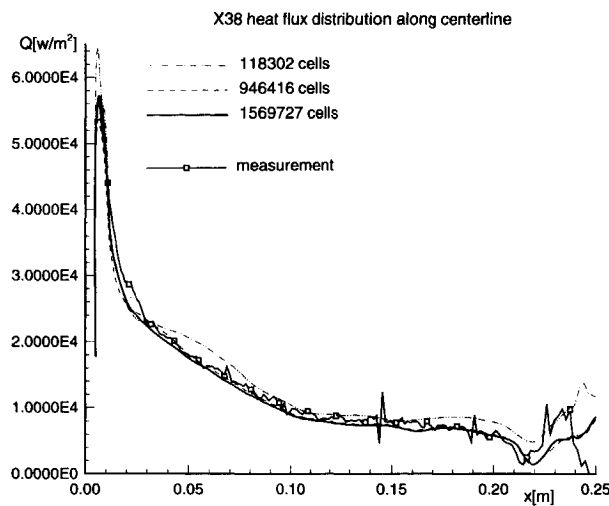


Figure 5.31: Comparison of heat flux distribution on the centerline between computed laminar solution and measurements in the LaRC wind tunnel.

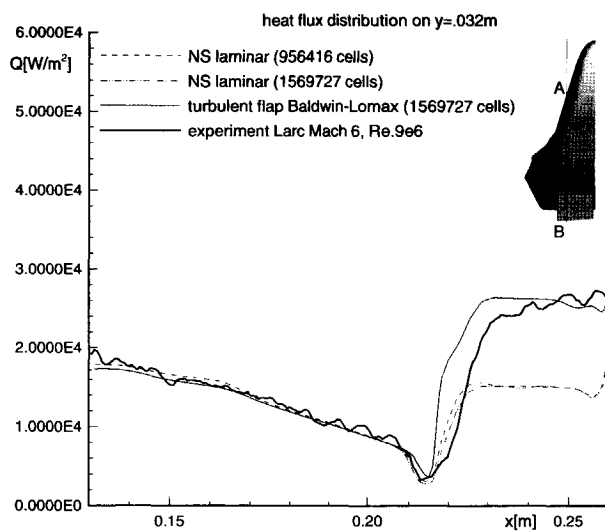


Figure 5.32: Heat flux comparison on line parallel to the symmetry plane with computed and measured in LaRC wind tunnel.

5.2.3 Nose heating along trajectory

In section 5.2.2 we focused on the validation of the solver through data from advanced heat flux measurement techniques in well defined conditions in a cold hypersonic wind tunnel. Here we shall assess the heating along a designed trajectory called “cycle 7”. Several cycles, based upon the Shuttle guidance, have been made to find the optimum re-entry based on knowledge of the aerodynamic characteristics of the vehicle and the vehicle constraints (maximum heating, maximum dynamic pressure, load factor and minimum duration of constant drag phase). A critical point in the design of the trajectory is the peak heating occurring during its hypersonic re-entry. Therefore the heating in the nose region is simulated and shows the influence of the material acting as a catalyst. In Table 5.3 the X-38 freestream conditions during hypersonic re-entry (cycle 7) are listed. For this exercise a medium and fine mesh

M	Re(L=8.41248m)	T [K]	$\rho [kg/m^3]$	U [m/s]
25	192965	218	.44297 10^{-4}	7399
22.5	377303	223	.96985 10^{-4}	6737
20	616285	231	.1782 10^{-3}	6105
17.5	1007181	243	.3419 10^{-3}	5472
15	1546672	255	.6225 10^{-3}	4807

Table 5.3: Freestream conditions along cycle 7 trajectory of X-38

has been created with 62,500 and 500,000 cells, respectively. A front view of the mesh is given in Figure 5.33. First the solution on the medium mesh is computed, then the solution is interpolated on the fine mesh and the computation is restarted.

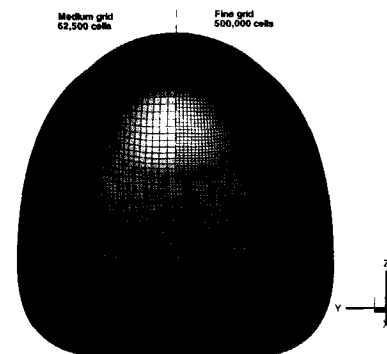


Figure 5.33: Surface plots of medium and fine mesh of the X-38 nose cap

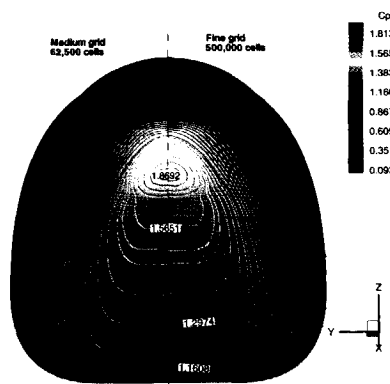


Figure 5.34: Pressure contour lines on X-38 nose cap for Mach 25 with catalytic assumption

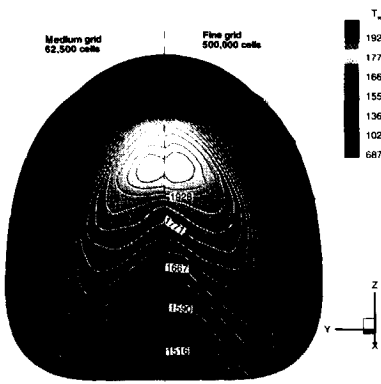


Figure 5.35: Heat flux contour lines on X-38 nose cap for Mach 25 with catalytic assumption

Similar to the ARD computational simulations, the nonequilibrium calculations have been performed using Dunn and Kang reaction set comprising 5 species (N_2, O_2, NO, N, O). A two-temperature model has been chosen to model the vibrational energy. The wall is modeled with a radiative equilibrium wall temperature with an emissivity value of 0.85. A pressure contour plot obtained on the medium and fine mesh is depicted in Figure 5.34. Corresponding heat fluxes have been plotted in Figure 5.35 assuming a fully catalytic wall. Qualitative comparison of pressures and heat fluxes contour lines on both meshes exhibit an overall grid independent solution.

Quantitative heat flux values using different assumptions of catalysis on the centerline for Mach 25 and 15 are shown for both meshes in Figure 5.36 and Figure 5.37. First it is noted that a grid independent solution is obtained within a 2% percent accuracy. Second, the typical behavior of the catalysis modeling can be observed: a fully catalytic assumption yields the highest heat flux, the non-catalytic assumption the lowest and the partial catalytic assumption an intermediate value. Since the catalysis of the material of the nose on X-38 is not yet determined, the test cases are assumed to be fully catalytic. It is interesting to note that between Mach 25 and Mach 15 the heating decreases when assuming a fully catalytic wall, whereas for the partial and non-catalytic cases the heating increases. This can be explained since for the latter two the recombination is faster due to the increased density, in contrast to the catalytic assumption where a full recombination is forced. When the Mach number approaches approximately 6 all three assumptions should result in the same value for heating.

The influence on the heat fluxes using a different chemistry set is shown on the centerline in Figure 5.38. The Park chemistry, which has faster reaction rates, produces, as expected, higher heat fluxes. The difference increases from the catalytic (1%), partial catalytic (2%)

towards non-catalytic assumption (8%).

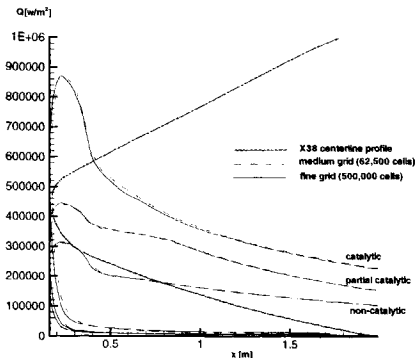


Figure 5.36: Heat flux centerline profile with different assumption of catalycity for Mach 25

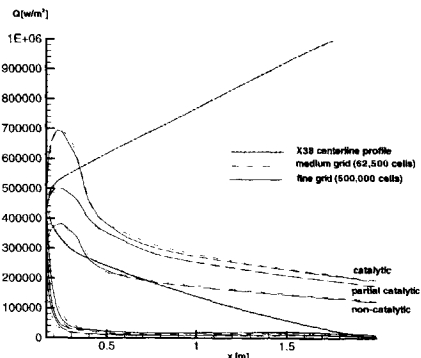


Figure 5.37: Heat flux centerline profile with different assumption of catalycity for Mach 15

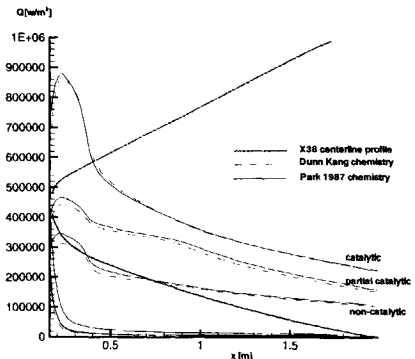


Figure 5.38: Heat flux centerline profile with different assumption of chemistry model

A comparison is made with quasi one-dimensional calculations using the CASL code [Verant and Walpot 2001]. For the CASL calculations the nose is approximated by a sphere with radius of 0.448 m. From the 3 dimensional calculations the translational and vibrational temperature on the stagnation line is extracted and compared with those from CASL. These comparisons are plotted in Figures 5.39 till 5.41. For all three Mach numbers the translational and vibrational temperature from the 3D simulation compare very well with the 1D simulation. Although the peak translational temperatures are not reached in the vicinity of the shock for the 3D case, due to reduced number of mesh points compared to the 1D case, it

has no influence on the temperature distribution in the shock layers. It can also be seen that a large portion of the shock layer for the Mach 25 case is in thermal nonequilibrium, whereas for the Mach 15 case it is almost completely in thermal equilibrium due to the higher density and lower velocity. A 1D -3D comparison is made for the N_2 massfraction distribution on the stagnation line assuming different catalysis in Figure 5.42. Here it is shown clearly that the recombination of diatomic nitrogen affects the heat flux by releasing energy at the wall.

The maximum heat fluxes for different Mach numbers are summarized in Table 5.4. A difference of less than 3% is obtained between the one-dimensional values and the three-dimensional values. Looking at this table, one can clearly notice the importance of the underlying assumption of wall catalysis. A maximum reduction of 60% in heat flux has been found at Mach 22.5 between the different wall catalysis hypotheses.

	$Q[\text{kW/m}^2] (T_w [\text{K}])$ (1D CASL)	$Q[\text{kW/m}^2] (T_w [\text{K}])$ 3D (LORE)
Mach 15 catalytic	698 (1950)	702 (1953)
	513 (1806)	505 (1799)
	395 (1692)	383 (1679)
Mach 20 catalytic	870 (2061)	874 (2063)
	526 (1817)	520 (1812)
	375 (1670)	372 (1667)
Mach 22.5 catalytic		902 (2079)
		486 (1783)
		351 (1641)
Mach 25 catalytic	881 (2067)	875 (2064) — 885(2069)*
	446 (1744)	446 (1744) — 467(1764)*
	317 (1601)	326 (1612) — 352(1643)*

Table 5.4: Maximum heat flux and wall temperatures for X-38 Cycle 7 trajectory

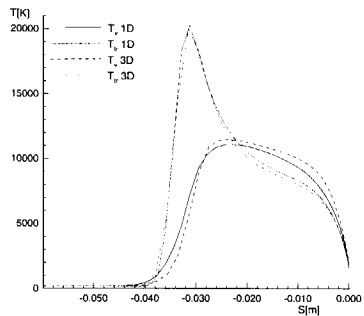


Figure 5.39: Stagnation line temperature profiles comparison (trans-rot and vibrational) for 3D and 1D predictions at Mach 25

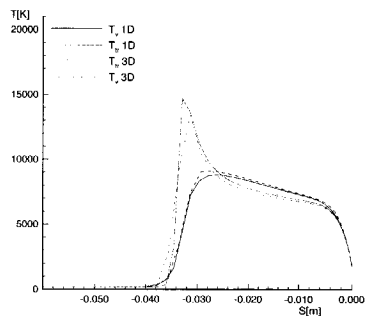


Figure 5.40: Stagnation line temperature profiles comparison (trans-rot and vibrational) for 3D and 1D predictions at Mach 20

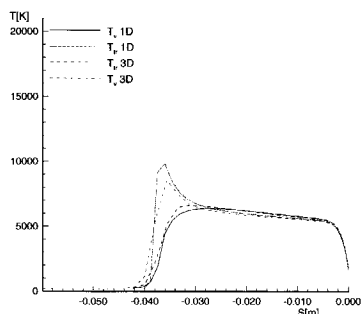


Figure 5.41: Stagnation line temperature profiles comparison (trans-rot and vibrational) for 3D and 1D predictions at Mach 15

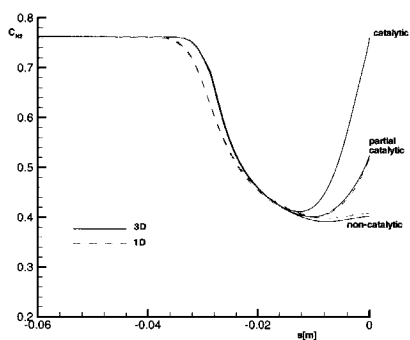


Figure 5.42: Stagnation line N_2 mass-fraction profiles comparison with different catalycity assumption for 3D and 1D predictions at Mach 25

5.2.4 Prediction of free-flight hypersonic pitching moments

Since there are no wind tunnels which can simulate all aspects of the hypersonic re-entry of the X-38, one has to rely on computational tools to predict the aerodynamic characteristics of the vehicle. In this section the different contributions of Mach number, viscous and “real gas” effects on the pitching moments will be demonstrated. For this purpose, the X-38 configuration has been chosen with the nominal hypersonic flush-outboard settings of the rudder and zero body flap deflection. The same meshes have been used as in Section 5.2.2, and grid convergence has been achieved. In Figure 5.43 several perfect gas, Euler as well as Navier-Stokes calculations are shown. Similarly thermo-chemical nonequilibrium modeling have been applied. First we can see the good agreement with the NAX solver [Molina et al. 1996] for modeling Euler perfect gas over the whole Mach range. Also the cold hypersonic facilities S3 (Mach 5.5) and S4 (Mach 10) show very good agreement within the computed perfect gas values.

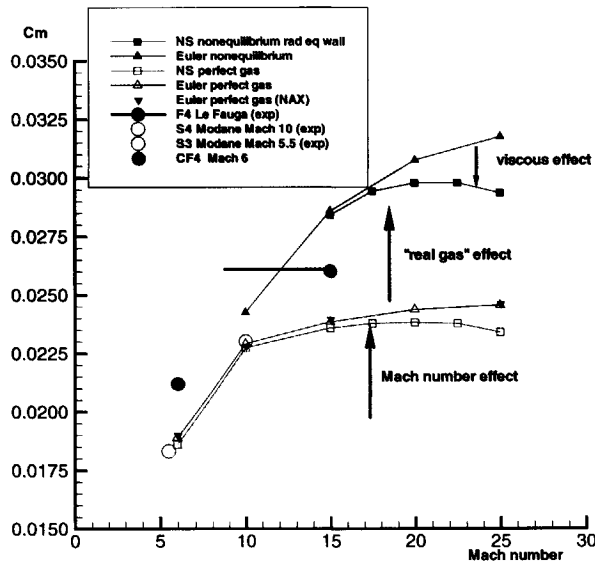


Figure 5.43: Computed and experimental obtained pitching moments in the hypersonic regime

The Mach number effect can be best assessed by increasing Mach number in a series of inviscid, perfect gas computations. The Mach number effect increases the pitch-up moment 0.02 towards 0.024. The viscous effects tend to decrease these moments at high Mach numbers. This is consistent, since at higher Mach numbers the Reynolds number decreases. Inclusion of “real gas” effects yields a noticeable increase in pitching moment. All these effects are consistent with the shuttle data. [Griffith et al. 1983] The measurement of the F4 high

enthalpy wind tunnel is included in the figure. As already mentioned in Chapter 4, it is difficult to assess the “real” freestream Mach number, due to lack of conclusive experimental data. Therefore a line is drawn from Mach 8.7 up to Mach 14, covering the range from thermo-chemical equilibrium to thermo-chemical nonequilibrium assumptions. Another possible way to interpret the F4 result is to compare the total enthalpy 21 MJ/kg of the wind tunnel tests with the flight enthalpy and deduce the corresponding Mach number from the trajectory. This results in a Mach number of 15. The F4 pitching moment is lower than all the computed free-flight moments, which could be explained by the scaled model which reduces the “real gas” effects.

An alternative means for the assessment of “real gas” effects on the aerodynamic characteristics in high enthalpy wind tunnels is the use of CF4 gas (tetrafluoromethane) in the Langley CF4 tunnel. Real gas effects on aerodynamics can be attributed to lowering of the specific heat ratio γ in the shock layer. This means that compared to perfect gas, compression regions exhibit higher surface pressures and expansion regions exhibit lower surface pressures. Freon is a heavy gas with three degrees of freedom for the rotational energy equal to $\frac{3}{2}RT$. The vibrational energy is modeled using a system of four harmonic oscillators, each with a different characteristic frequency [Jones and Hunt 1969]:

$$e_{vib} = R \sum_{i=1}^4 \frac{g_i \theta_i}{e^{\frac{\theta_i}{T}} - 1} \quad (5.2)$$

where

$$\begin{aligned} g_1 &= 1 & \theta_1 &= 1300\text{K} \\ g_2 &= 2 & \theta_2 &= 626\text{K} \\ g_3 &= 3 & \theta_3 &= 1845\text{K} \\ g_4 &= 3 & \theta_4 &= 918\text{K} \end{aligned} \quad (5.3)$$

This means that freon has a γ varying from $\frac{4}{3}$ to $\frac{6}{5}$ with full vibrational excitation.

We will investigate how the surface pressures on the X-38 surface changes compared to a thermo-chemical air simulation. In the present CF4 calculation the ideal gas equation of state is used and the viscosity is given by:

$$\mu = 1.22 \cdot 10^{-7} 149.5 \left(\frac{T}{409.5} \right)^{\frac{3}{2}} \frac{1.22}{\frac{T}{409.5} + .22} \quad (5.4)$$

The freestream conditions from the Langley CF4 tunnel are listed in Table 5.5. The same meshes have been used as in Section 5.2.2, and grid convergence has been achieved.

The pitching moment from the numerical simulation using CF4 gas is plotted in Figure 5.43. In this figure, a pitch-up moment is found compared to the perfect gas Mach 6 solution, but

M	Re(L=0.1475[m]) (Scale 1.75 %)	AoA	T [K]	$\rho [kg/m^3]$	U [m/s]
6	172417		40°	205.56	$1.7774 \cdot 10^{-2}$ 918.71

Table 5.5: Freestream conditions of the LARC CF4 Mach 6 wind tunnel

the increment is much smaller than predicted by the nonequilibrium solutions at higher Mach numbers. This can be explained by Figure 5.44 in which the centerline distribution of the pressure coefficient of freon in the wind tunnel is compared with a flight simulation at Mach 17.5 assuming perfect gas and thermo-chemical nonequilibrium.

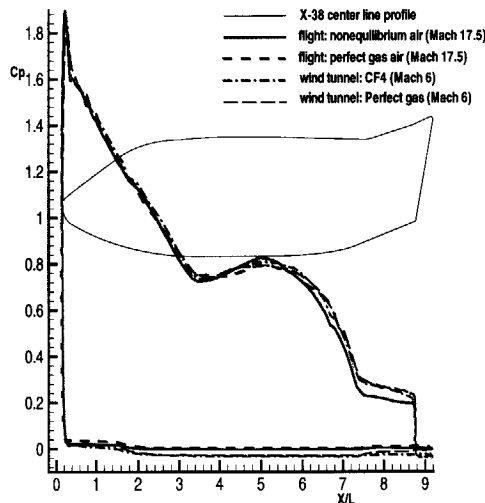


Figure 5.44: Pressure coefficient distribution comparison along X-38 centerline using air and freon gas

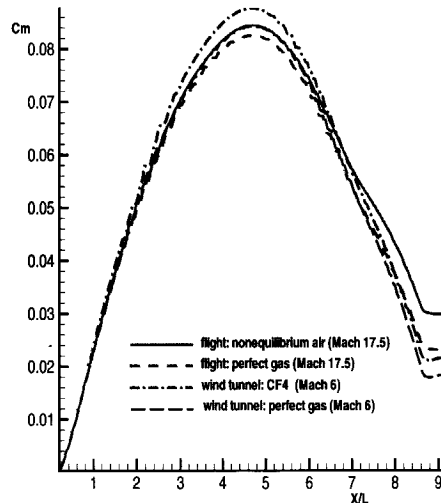


Figure 5.45: Pitching moment coefficient versus x-direction comparison for air and CF4 gas

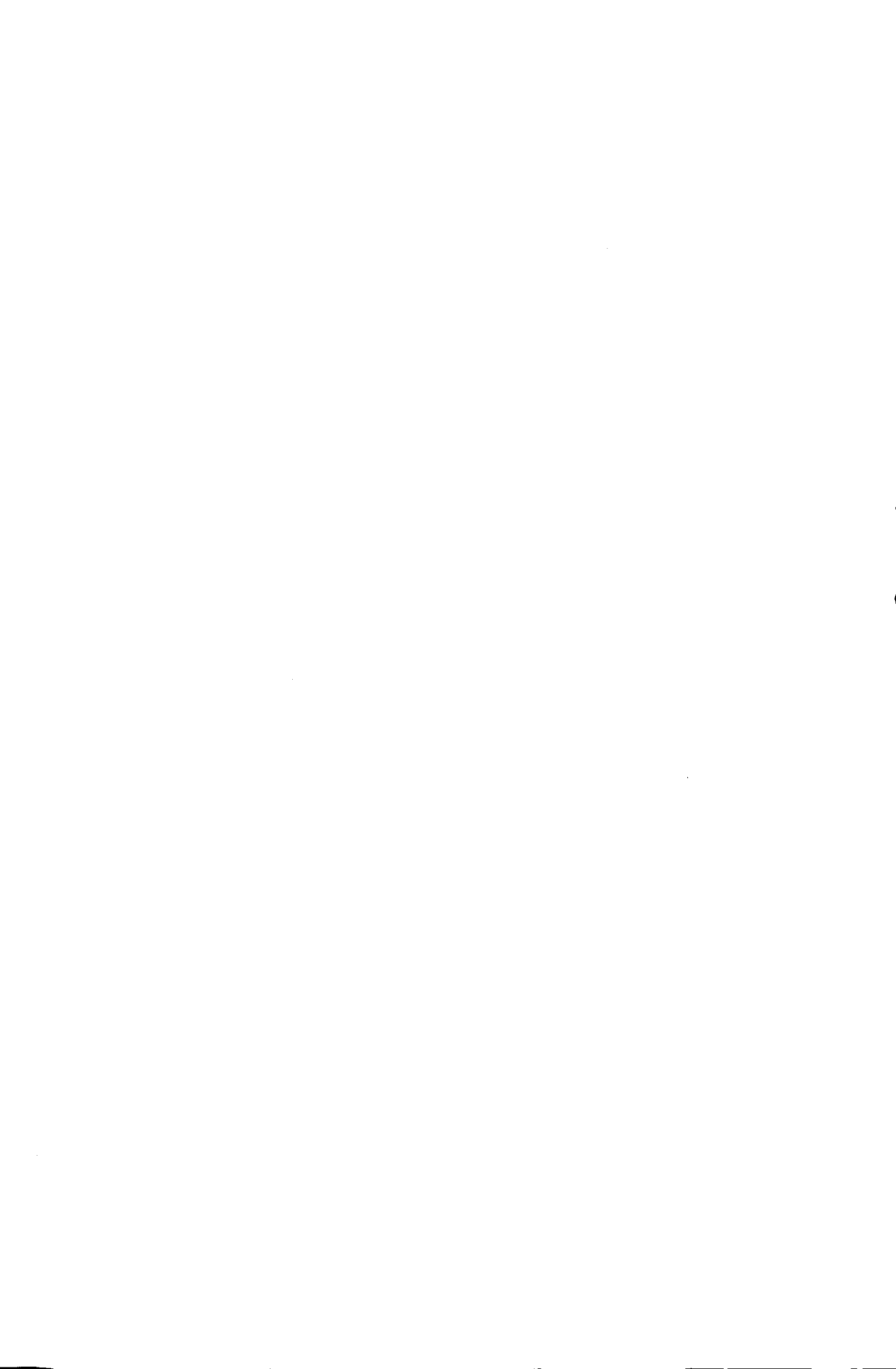
As can be noted lowering the specific heat of the gas at Mach 17.5 from perfect gas to nonequilibrium yield an increase of the pressure coefficient in the nose region and a decrease in pressure coefficient on the boat tail. Both effects contribute to the pitch-up moment. Also Shuttle test in the CF4 tunnel confirmed the nose-up pitching moment increment relative to pre-flight (cold hypersonic) predictions. A similar effect is noticeable between wind tunnel simulations using CF4 and perfect gas, although the effect is much smaller. The small effect of the Mach number increase is best seen at the leeward side where the pressure coefficients

for the Mach 6 cases are lower than the Mach 17.5. This small effect is also present on the windward side but here the effect of γ is dominant. The integrated pitching moments versus x-direction are plotted in Figure 5.45, where it shows clearly that the main difference originates from the windward boat tail. However, when comparing the CF4 result with the flight using a thermo-chemical nonequilibrium assumption, freon behaves similarly in compression region but not in expansion regions. From this comparison one concludes that freon wind tunnel tests, simulating “real gas” effects, are useful only for blunt bodies like capsules in which pitching moments are dominated by the compression regions. For this reason the X-38 project did not include the CF4 wind tunnel results in the aerodynamic database. In addition to this, the measured X-38 pitching moment from the CF4 wind tunnel has been disregarded by the X-38 project because it was determined to be faulty, for zero degree body flap.

5.3 Conclusions

In this chapter the capabilities of LORE have been demonstrated in real three dimensional hypersonic re-entry flows. In particular, in the Atmospheric Re-entry Demonstrator it has been shown how LORE can be used in the pre-flight analysis where extrapolation from wind tunnel experiments to flight situations have to be performed in order to achieve an optimal design. The post-flight analysis for the Atmospheric Re-entry Demonstrator shows excellent agreement with the flight data. The code allows one to switch on or off certain physical phenomena, thus demonstrating which physical contributions are responsible for the behavior which is experimentally observed.

An even more challenging enterprise was undertaken in the second section where flight predictions for the Crew Return Vehicle demonstrator X-38 are presented. Special attention in this section is paid to the heating of the vehicle since this is a critical issue for the type of thermal protection shields to be employed on the vehicle. Furthermore, predictions of the pitching moments have been presented. The different contributions of Mach number, viscous and high temperature effects on the pitching moments have been demonstrated, wherein in addition the simulations have been anchored with the wind tunnel data. It has been demonstrated that CF4 wind tunnel tests are useful for trends simulating “real gas” effects, but fail to predict the pitching moment increment compared to flight due to the different behavior in expansion regions.



6

Conclusions

The work presented in this thesis stresses the importance of CFD simulations in the analysis of the aerothermodynamic characteristics of hypersonic flow fields as has been demonstrated in ground based facilities with their associated test models and vehicles re-entering the earth atmosphere. For this purpose, an efficient combination of methods has been implemented to compute such flow fields. The equations governing the motion of a general mixture of thermally perfect gases for high temperatures have been formulated with finite rate chemistry and thermal nonequilibrium. A numerical scheme has been selected which has proven to be a good compromise between CPU cost, robustness and accuracy. A flow solver has been created and validated over the complete relevant hypersonic Mach range for a re-entry vehicle. Selected flows ranging from perfect gas to thermo-chemical nonequilibrium ionized gas conditions in hypersonic flow regime were considered. Moreover, in order to eliminate uncertainties arising from the modeling of turbulence, only laminar test cases have been selected. The results from the numerical simulations have been shown to agree with both wind tunnel experiments and flight data within measurement uncertainty.

The sensitivity of the thermo-chemical modeling has been highlighted in two state-of-the-art high enthalpy European wind tunnels: F4(ONERA) and HEG(DLR). Quasi one-dimensional and axisymmetric Navier-Stokes nozzle flow computations have been presented to provide an efficient means to assess the performance of parametric sensitivity. Based on these comparisons, static pressure, temperature and Mach number have been identified as the most sensitive to thermo-chemical behavior, in particular with respect to thermal nonequilibrium, full equilibrium and sudden vibrational relaxation effects along the nozzle. Conversely, density, velocity and Pitot pressure have been found to be rather insensitive to thermo-chemical effects. High density real gas effects have been shown to be irrelevant at the current levels of operating pressure in high enthalpy facilities in Europe. It is the author's belief that the present measurements techniques in these facilities are insufficiently developed to refine the current thermo-chemical models. This is mainly due to the uncertainties in the measurements, the associated operation conditions and the insensitivity of the measured parameters. As an example, the use of one averaged vibrational energy equation, instead of modeling vibrational energies, has produced heat fluxes and wall pressures well within the measure-

ment uncertainty limits. Moreover, the reservoir conditions for the computations depend on how accurately the measurements have been carried out and how these quantities are derived. Also flow contamination, e.g. helium contamination or copper vapor from the wall liner, could play a role on the accurate assessment of the measurements on the model. Therefore, presently, these high enthalpy wind tunnels can be used only to see trends for real gas effects compared to cold wind tunnels. However, quantitative wind tunnel results are essential because experimental wind tunnel results provide the anchoring for the prediction of flight conditions. Therefore, a quantitative assessment of high speed measurement techniques in nozzle flows is mandatory. The work presented in this thesis has proven to be a viable and useful tool to that end.

In this thesis the extrapolation to flight for two re-entry vehicles has been addressed, namely the ARD capsule and the X-38 CRV demonstrator. This methodology involves validating the computational simulations at the start of hypersonic regime with classical “cold” hypersonic wind tunnel tests. Wall pressures, heat fluxes, forces and pitching moments have been simulated within the uncertainty of the measurements of the S4 wind tunnel data. The “real gas” effects have been successfully simulated for the ARD in terms of predicting the shift in trim angle in flight compared to the cold wind tunnel tests.

For the X-38 demonstrator, when extrapolating to flight, the Mach number, viscous and “real gas” effects compared to “cold” hypersonic wind tunnel data on the pitching moment have been successfully demonstrated. Although this vehicle has not flown yet, the trend on the pitching moment increment is also confirmed by comparing Shuttle flight data with “cold” hypersonic wind tunnel data. It has been shown for the X-38 that CF4 wind tunnel tests are useful for trends simulating “real gas” effects, but fail to predict the complete pitching moment increment compared to flight due to the different behavior in expansion regions.

Also we have shown the importance of the assumption of surface catalysis of the material. A maximum difference of 60% in heat flux at the stagnation point has been obtained between fully catalytic and non-catalytic wall properties. Since heat fluxes are essential in setting the trajectory constraints, more effort has to be put into the characterization of catalytic and radiative properties of the materials.

To the author’s knowledge, the code developed in the frame of this thesis is unique in that it has been thoroughly validated on the most extensive set of well selected wind tunnel experiments and re-entry flight data available to this date. These test cases range from academic axisymmetric models as well as complex three-dimensional geometries. The applicability for the analysis is limited only by the ability of the structured mesh generation paradigm itself. The structure of the code is so general that, outside the goal of this thesis, a nonequilibrium two-phase flow extension to the solver has been readily implemented. [Walpot et al. 1997]. Because the tool has been carefully validated it becomes a valuable tool for design of wind tunnel/flight models and generation of aerothermodynamic characteristics for re-entry vehicles.

A

Physical modeling

A.1 Mass production rate due to chemical reactions

In this section an expression will be derived for the rate of change of mass of species s per unit volume (the source term ω_s in equation (2.9)). A number of different elementary chemical reactions between species in the gas can occur simultaneously. Consider the j th chemical reaction of N_{reac} elementary reactions between N_{sp} chemically reacting species χ_s :

$$\sum_{s=1}^{N_{sp}} \nu'_{s,j} \chi_s \xrightleftharpoons[k_{b,j}]{k_{f,j}} \sum_{s=1}^{N_{sp}} \nu''_{s,j} \chi_s , \quad (\text{A.1})$$

where $\nu'_{s,j}$ and $\nu''_{s,j}$ represent the stoichiometric mole numbers of reactants and products of reaction j , respectively. The chemical reaction equation (A.1) consists of a forward and backward part. Empirical results have shown that the time rate of formation of the number of moles per unit volume $[\chi_s]_j^f$ of the forward and backward reaction j is given by:

$$\text{forward : } \frac{d[\chi_s]_j^f}{dt} = \left(\nu''_{s,j} - \nu'_{s,j} \right) \left[k_{f,j} \prod_{s=1}^{N_{sp}} [\chi_s]^{\nu'_{s,j}} \right] , \quad (\text{A.2})$$

$$\text{backward : } \frac{d[\chi_s]_j^b}{dt} = \left(\nu''_{s,j} - \nu'_{s,j} \right) \left[k_{b,j} \prod_{s=1}^{N_{sp}} [\chi_s]^{\nu''_{s,j}} \right] ,$$

in which $k_{f,j}$ and $k_{b,j}$ denote the forward and backward reaction rate coefficients of reaction j , which generally depend on a reaction temperature. The net rate for the above general reaction j can be written as:

$$\frac{d[\chi_s]_j}{dt} = \frac{d[\chi_s]_j^f}{dt} - \frac{d[\chi_s]_j^b}{dt} = \left(\nu''_{s,j} - \nu'_{s,j} \right) \left[k_{f,j} \prod_{s=1}^{N_{sp}} [\chi_s]^{\nu'_{s,j}} - k_{b,j} \prod_{s=1}^{N_{sp}} [\chi_s]^{\nu''_{s,j}} \right] . \quad (\text{A.3})$$

Equation (A.3) is a general form of the law of mass action, which ensures the preservation of total mass during a chemical reaction.

The rate of change of mass of species s per unit volume of the mixture can be found by a summation over all the reactions N_{reac} :

$$\omega_s = \frac{d}{dt} (\rho_s) = M_s \sum_{j=1}^{N_{reac}} \frac{d}{dt} [\chi_s]_j . \quad (\text{A.4})$$

The forward reaction rates are generally determined experimentally. These empirical results are correlated in the form:

$$k_{f,j} = c_{f,j} T_{reac;f,j}^{n_{f,j}} e^{-\Theta_{f,j}/T_{reac;f,j}}, \quad (\text{A.5})$$

which is known as the Arrhenius equation. The parameters $c_{f,j}$, $n_{f,j}$ and the activation energy $\Theta_{f,j}$ for different reactions are given in Table A.1. The values for $k_{f,j}$ are usually computed by fitting experimental data. In the present thesis two sets of chemical reactions sets for air have been employed: the Park [1987] model and the Dunn and Kang [1973] model. The Park model yields much faster rates compared to the Dunn and Kang model. The Arrhenius equation contains the reaction temperature $T_{reac;f,j}$. For conditions at local thermodynamic equilibrium, $T_{reac;f,j}$ equals to the equilibrium temperature T . For thermal nonequilibrium situations, $T_{reac;f,j}$ will be a function of the different local vibrational and electronical temperatures, formally expressed as:

$$T_{reac;f,j} = T_{reac;f,j} (T; T_{v_m}; T_e) . \quad (\text{A.6})$$

The determination of $T_{reac;f,j}$ for thermal nonequilibrium situations is given in the next section. The backward rate $k_{b,j}$ is determined using the equilibrium constant $K_{eq,j}$. In equilibrium, the net rate in equation (A.3) is zero, thus the equilibrium constant of a reaction j can be written as:

$$K_{eq,j} = \frac{k_{f,j} \prod_{s=1}^{N_{sp}} [\chi_s]^{\nu''_{s,j}}}{k_{b,j} \prod_{s=1}^{N_{sp}} [\chi_s]^{\nu'_{s,j}}} . \quad (\text{A.7})$$

The equilibrium constant $K_{eq,j}$ in terms of concentrations is obtained using the minimization of Gibbs' free enthalpy and reads [Anderson 1989]:

$$K_{eq,j} (T) = \mathcal{R}T \left[- \sum_{s=1}^{N_{sp}} \left(\nu''_{s,j} - \nu'_{s,j} \right) \exp \left[\sum_{s=1}^{N_{sp}} \left(\nu''_{s,j} - \nu'_{s,j} \right) \left(\frac{s_s}{R_s} - \frac{h_s}{R_s T} \right) \right] \right] . \quad (\text{A.8})$$

The backward reaction rate $k_{b,j}$ can now be calculated from equation (A.8) and equation (A.5) :

$$k_{b,j}(T_{reac;b,j}) = \frac{k_{f,j}(T_{reac;b,j})}{K_{eq_j}(T_{reac;b,j})}. \quad (\text{A.9})$$

The backward reaction temperature $T_{reac;b,j}$ can be different from the forward reaction temperature $T_{reac;f,j}$. As noted earlier, expressions for both temperatures will be discussed in the next section.

reaction	Dunn and Kang model			Park '87 model		
	c_f	n_f	Θ_f	c_f	n_f	Θ_f
$O_2 + N \rightarrow 2 O + N$	3.60E18	-1.00	5.95E04	2.900E23	-2.00	5.975E04
$O_2 + NO \rightarrow 2 O + NO$	3.60E18	-1.00	5.95E04	9.680E22	-2.00	5.975E04
$O_2 + O \rightarrow 2 O + O$	9.00E19	-1.00	5.95E04	2.900E23	-2.00	5.975E04
$O_2 + O_2 \rightarrow 2 O + O_2$	3.24E19	-1.00	5.95E04	9.680E22	-2.00	5.975E04
$O_2 + N_2 \rightarrow 2 O + N_2$	7.20E18	-1.00	5.95E04	9.680E22	-2.00	5.975E04
$N_2 + O \rightarrow 2 N + O$	1.90E17	-0.50	1.13E05	4.980E22	-1.60	1.132E05
$N_2 + NO \rightarrow 2 N + NO$	1.90E17	-0.50	1.13E05	4.980E21	-1.60	1.132E05
$N_2 + O_2 \rightarrow 2 N + O_2$	1.90E17	-0.50	1.13E05	3.700E21	-1.60	1.132E05
$N_2 + N \rightarrow 2 N + N$	4.08E22	-1.50	1.13E05	1.600E22	-1.60	1.132E05
$N_2 + N_2 \rightarrow 2 N + N_2$	4.70E17	-0.50	1.13E05	3.700E21	-1.60	1.132E05
$NO + O_2 \rightarrow N + O + O_2$	3.90E20	-1.50	7.55E04	7.950E23	-2.00	7.550E04
$NO + N_2 \rightarrow N + O + N_2$	3.90E20	-1.50	7.55E04	7.950E23	-2.00	7.550E04
$NO + O \rightarrow N + O + O$	7.80E21	-1.50	7.55E04	7.950E23	-2.00	7.550E04
$NO + N \rightarrow N + O + N$	7.80E21	-1.50	7.55E04	7.950E23	-2.00	7.550E04
$NO + NO \rightarrow N + O + NO$	7.80E21	-1.50	7.55E04	7.950E23	-2.00	7.550E04
$NO + O \rightarrow O_2 + N$	3.20E09	1.00	1.97E04	8.370E12	0.00	1.945E04
$N_2 + O \rightarrow NO + N$	7.00E13	0.00	3.80E04	6.440E17	-1.00	3.837E04
$O_2^+ + O \rightarrow O_2 + O^+$	2.92E18	-1.11	2.80E04	6.850E13	-0.52	1.860E04
$N_2 + N^+ \rightarrow N_2^+ + N$	2.02E11	0.81	1.30E04	9.850E12	-0.18	1.210E04
$NO^+ + O \rightarrow NO + O^+$	3.63E15	-0.60	5.08E04	2.750E13	0.01	5.100E04
$N_2 + O^+ \rightarrow N_2^+ + O$	3.40E19	-2.00	2.30E04	6.330E13	-0.21	2.220E04
$NO^+ + O_2 \rightarrow NO + O_2^+$	1.80E15	0.17	3.30E04	1.030E16	-0.17	3.240E04
$NO^+ + N \rightarrow NO + N^+$	1.00E19	-0.93	6.10E04	1.700E13	0.40	3.550E04
$N + O \rightarrow NO^+ + e^-$	1.40E06	1.50	3.19E04	1.530E09	0.37	3.200E04
$O + O \rightarrow O_2^+ + e^-$	3.85E09	0.49	8.06E04	1.600E17	-0.98	8.080E04
$N + N \rightarrow N_2^+ + e^-$	1.40E13	0.00	6.78E04	1.790E09	0.77	6.750E04
$O + e^- \rightarrow O^+ + e^- + e^-$	3.60E31	-2.91	1.58E05	3.900E33	-3.78	1.585E05
$N + e^- \rightarrow N^+ + e^- + e^-$	1.10E32	-3.14	1.69E05	2.500E33	-3.82	1.686E05
$O_2 + N_2 \rightarrow NO + NO^+ + e^-$	1.38E20	-1.84	1.41E05	-	-	-
$N_2 + NO \rightarrow N_2 + NO^+ + e^-$	2.20E15	-0.35	1.08E05	-	-	-
$NO^+ + O \rightarrow O_2 + N^+$	1.34E13	0.31	7.72E04	-	-	-
$O_2 + NO \rightarrow NO^+ + O_2 + e^-$	8.80E16	-0.35	1.08E05	-	-	-
$NO + N_2^+ \rightarrow N + O + N_2^+$	-	-	-	7.950E23	-2.00	7.550E4
$NO + O_2^+ \rightarrow N + O + O_2^+$	-	-	-	7.950E23	-2.00	7.550E4
$NO + NO^+ \rightarrow N + O + NO^+$	-	-	-	7.950E23	-2.00	7.550E4
$NO + N^+ \rightarrow N + O + N^+$	-	-	-	7.950E23	-2.00	7.550E4
$NO + O^+ \rightarrow N + O + O^+$	-	-	-	7.950E23	-2.00	7.550E4
$N_2 + N_2^+ \rightarrow 2N + N_2^+$	-	-	-	8.300E24	-1.60	1.132E5
$N_2 + O_2^+ \rightarrow 2N + O_2^+$	-	-	-	8.300E24	-1.60	1.132E5
$N_2 + NO^+ \rightarrow 2N + NO^+$	-	-	-	8.300E24	-1.60	1.132E5
$N_2 + N^+ \rightarrow 2N + N^+$	-	-	-	8.385E24	-1.60	1.132E5
$N_2 + O^+ \rightarrow 2N + O^+$	-	-	-	8.300E24	-1.60	1.132E5
$O_2 + N_2^+ \rightarrow 2O + N_2^+$	-	-	-	9.680E22	-2.00	5.975E4
$O_2 + O_2^+ \rightarrow 2O + O_2^+$	-	-	-	9.680E22	-2.00	5.975E4
$O_2 + NO^+ \rightarrow 2O + NO^+$	-	-	-	9.680E22	-2.00	5.975E4
$O_2 + N^+ \rightarrow 2O + N^+$	-	-	-	9.680E22	-2.00	5.975E4
$O_2 + O^+ \rightarrow 2O + O^+$	-	-	-	9.680E22	-2.00	5.975E4

Table A.1: Forward rate constants in C.G.S. units of the kinetic model of Dunn and Kang [1973] and of Park [1987]

A.2 **Vibration-Dissociation coupling**

When vibrationally excited molecules dissociate, it is clear that dissociation reduces the vibrational energy of the molecules. Analogously, recombination will increase the vibrational energy. This process is taken into account by the term Q_{V-D} in equation (2.9).

Also it is likely that vibrationally excited molecules dissociate easier than molecules which are not vibrationally excited. This is the so-called preferential dissociation. To account for this effect the reaction rates depend on the vibrational temperature.

To account for both effects, two models are proposed in the literature: the simple Park [1990] model and the model of Treanor and Marrone [1962]. Both will be briefly discussed below.

A.2.1 **Park model**

When a molecule dissociates, the vibrational energy associated with that molecule has to be removed from the vibrational energy pool. Therefore

$$Q_{V-D} = \omega_m e_{v_m} , \quad (\text{A.10})$$

represents the amount of vibrational energy gained or lost due to molecular depletion or production of species m .

Concerning the preferential dissociation, Park [1990] suggests the inclusion of the influence of the vibrational energy in the reaction temperature as follows:

$$T_{\text{reac},f} = \begin{cases} T^n T_{v_m}^{1-n} & \text{if no free electrons are generated} \\ T_e^n T_{v_m}^{1-n} & \text{if free electrons are generated} \end{cases} , \quad (\text{A.11})$$

where n is between 0.5 and 0.7. Park applies the relation only in the determination of the forward reaction rate of dissociation reactions. The model assumes that the backward reaction rate is governed by the translational temperature:

$$T_{\text{reac},b_j} = T . \quad (\text{A.12})$$

The relations are empirical. Park calibrated his computational results with experiments.

A.2.2 Treanor and Marrone model

The vibrational dissociation coupling described by the model of Treanor and Marrone [1962; 1963] consists basically of two parts. The first part describes the vibrational energy, influenced by dissociation and recombination. The second part treats the effect of vibrational energy on the dissociation reaction rate.

The energy exchange between vibration and dissociation, term (8) in the vibrational energy equation in system (2.9), may be written as:

$$Q_{V-D} = [e_{v_m} - e_{v_m}^{diss}] \left(\frac{d\rho_m}{dt} \right)_{diss} + [e_{v_m}^{recomb} - e_{v_m}] \left(\frac{d\rho_m}{dt} \right)_{recomb} , \quad (\text{A.13})$$

in which $e_{v_m}^{diss}$ and $e_{v_m}^{recomb}$ is the vibrational energy lost by a dissociation and gained by a recombination, respectively. Let $\left(\frac{d\rho_m}{dt} \right)_{diss}$ be the rate of the mass depletion per unit volume of the dissociating species m , and $\left(\frac{d\rho_m}{dt} \right)_{recomb}$ the rate at which molecules are being formed by recombination. Summing over all the dissociation-reactions, yields:

$$\left(\frac{d\rho_m}{dt} \right)_{diss} = M_m \sum_{j=diss} \left(\nu'_{m,j} - \nu''_{m,j} \right) k_{f_j} \prod_s [\chi_s]^{\nu'_{s,j}} , \quad (\text{A.14a})$$

$$\left(\frac{d\rho_m}{dt} \right)_{recomb} = M_m \sum_{j=diss} \left(\nu'_{m,j} - \nu''_{m,j} \right) k_{b_j} \prod_s [\chi_s]^{\nu''_{s,j}} . \quad (\text{A.14b})$$

Marrone and Treanor [1963] assume that the rate of dissociation from any vibrational level is proportional to the product of the population in that level and the collision rate with particles having sufficient translational energy to cause dissociation from that level. The vibrational energy $e_{v_m}^{diss}$ of a dissociating molecule can therefore be expressed as:

$$e_{v_m}^{diss} = e_{v_m}(T_{F_m}) , \quad (\text{A.15})$$

where the temperature T_{F_m} is defined by

$$\frac{1}{T_{F_m}} = \frac{1}{T_{v_m}} - \frac{1}{T} - \frac{1}{U} . \quad (\text{A.16})$$

The probability temperature, U , models the tendency of the vibrating molecule to dissociate more explicitly at the upper levels (preferential dissociation). $U = \infty$ corresponds to the situation that dissociation occurs with equal probability from any vibrational level in any collision that has sufficient translational energy to effect the dissociation. Treanor and Marrone determine the constant U which fit best their computations with experiments as

$$U = \frac{\theta_{d_m}}{3} , \quad (\text{A.17})$$

where θ_{d_m} is the characteristic dissociation temperature, equal to Θ_f (Θ_{f_j} of the Arrhenius equation (A.5)) for a dissociation reaction of species m .

As a consequence of detailed balance at thermodynamic equilibrium ($T_{v_m} = T$), the vibrational energy $e_{v_m}^{recomb}$ of a molecule after recombination equals that of the dissociating molecule before dissociation.

$$[e_{v_m}^{recomb}]_{eq} = [e_{v_m}^{diss}(T, T_{v_m})]_{eq} = e_{v_m}^{diss}(T, T) = e_{v_m}(-U) . \quad (\text{A.18})$$

Using the harmonic oscillator model, the vibrational energy e_{v_m} expressed as a function of the temperature is:

$$e_{v_m}(T) = \frac{\theta_m R_m}{e^{\frac{\theta_m}{T}} - 1} - \frac{\theta_{d_m} R_m}{e^{\frac{\theta_{d_m}}{T}} - 1} , \quad (\text{A.19})$$

where the values for θ_m can be found in Table A.2. Formally, the negative quantity $-U$ can be considered as the vibrational temperature at which the molecules are formed by recombination. Being negative, it indicates an inversion of the population-distribution of newly formed molecules.

The effect of vibrational relaxation on the dissociation rate k_f is modeled as a function of T, T_{v_m} and U :

$$k_f = k_{f_{eq}} \frac{Q(T_F)Q(T)}{Q(-U)Q(T_{v_m})} , \quad (\text{A.20})$$

where $k_{f_{eq}}$ is the forward reaction rate coefficient evaluated at the equilibrium reaction temperature $T_{reac} = T$ and Q denotes the vibrational partition functions evaluated at the different temperatures. Application of the harmonic oscillator model yields for the vibrational partition functions:

$$Q(T_n) = \frac{1 - e^{-\frac{\theta_{d_s}}{T_n}}}{1 - e^{-\frac{\theta_s}{T_n}}} , \quad (\text{A.21})$$

where T_n stands for $T_{v_m}, T, -U$ or T_{v_m} .

A.3 Electronic energy reactive source term

Term (16) in equation (2.9) accounts for the rate of electron energy loss when a free electron strikes a neutral particle and ionizes the particle. When the electron temperature and density reach certain values, the reaction is triggered. The process occurs in a chain reaction, and the electron density increases exponentially within a short time in a small region and the energy absorption is very rapid. This results in a loss of electron translational energy and translational energy of the heavy particles. A reaction involving electron impact ionization has the form



where A stands for the ionizing nitrogen or oxygen and e^- denotes an electron. The loss of electron translational energy due to electron impact ionization is expressed as:

$$Q_{ERS} = \sum_{s=ion} \dot{n}_{e_s} \hat{I}_s , \quad (A.23)$$

in which $\dot{n}_{e_s} = \frac{d[e]}{dt}$ is the net molar rate of ionization in kmol/s, given by equation (A.3). The subscript j in equation (A.3) refers to the ionization reaction (A.22). The ionization-energy, \hat{I}_s , per kmole of species A is measured from the ground level. The ionization energy \hat{I}_s in $J/kmol$ equals:

$$\hat{I}_s = \frac{h_{0_{s_{ion}}} - h_{0_s}}{M_s} . \quad (A.24)$$

Values for the zero point enthalpies of the ionizing species h_{0_s} and the molar mass M_s are given in table A.2.

species	M_s kg/kmole	h_{0_s} J/kg	θ_m K
N ₂	28.0134	0	3395
O ₂	31.9888	0	2239
NO	30.0061	3.0091E+06	2817
N	14.0067	3.3747E+07	-
O	15.9994	1.5574E+07	-
N ₂ ⁺	28.0129	5.3886E+07	3177
O ₂ ⁺	31.9983	3.6592E+07	2691
NO ⁺	30.0056	3.3000E+07	3482
N ⁺	14.0062	1.3438E+08	-
O ⁺	15.9989	9.8056E+07	-
e ⁻	5.4858E-04	0	-

Table A.2: Thermodynamic species data from Gnoffo et al. [1989]

A.4 Energy exchange mechanisms

The energy exchange mechanisms, appearing in equation (2.9) between translation, vibrational and electronic energy due to elastic and inelastic collisions of particles are described in this section. The proposed models are simplifications of the complicated energy exchange processes that occur at the molecular level. The following energy exchange processes are discussed:

- translational-vibrational energy exchange (T-V), term (6)
- vibrational-vibrational energy exchange (V-V), term (9)
- translational-electronic energy exchange (T-E), term (14)
- vibrational-electronic energy exchange (V-E), term (7) and (15)

A.4.1 Translational-Vibrational energy exchange

The model of translational-vibrational relaxation is based on the early model of Landau and Teller [1936]. The model of Landau and Teller supposes that vibrationally excited diatomic molecules are submerged in an environment (heat bath) consisting of molecules in thermal equilibrium at translational-rotational-vibrational temperature T . The submerged vibrationally excited molecules have a different vibrational temperature T_v from that of the bath. The vibrational excited molecules will exchange their vibrational energy with the translational-rotational energy and after a period of time will relax towards a new translational-rotational-vibrational equilibrium temperature T of the whole system. In Figure A.1, $e_v(T_v)$ denotes the instantaneous value of the vibrational energy immediately after the excitation at $t=0$. For this case, the vibrational energy of the submerged molecules exceeds the equilibrium value of the bath, $e_v(T)$. This results in a redistribution of the internal energy and therefore the equilibrium temperature increases. The model is derived for diatomic molecules which

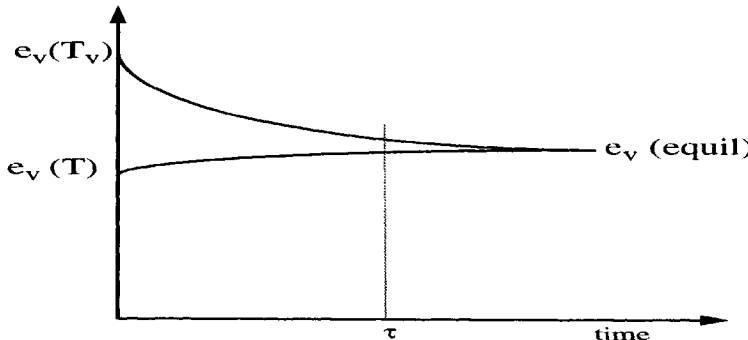


Figure A.1: Illustration of relaxation time

are assumed to behave as harmonic oscillators, allowing only transitions by one vibrational quantum level [Vincenti and Kruger 1965]. The resulting vibrational energy exchange rate

per unit of volume (term (6) of equation (2.9)) becomes:

$$Q_{T-V} = \rho_m \frac{e_{v_m}(T) - e_{v_m}(T_{v_m})}{\tau_m} , \quad (\text{A.25})$$

where e_{v_m} is the vibrational energy per unit mass of the vibrational excited species m . If, in a general case, the heat bath is not in thermal equilibrium, the local equilibrium thermodynamic temperature is supposed to be equal to the translational-rotational temperature. Therefore, e_{v_m} is the vibrational energy per unit mass of a molecule m evaluated at this local translational-rotational temperature. The quantity τ_m is the molar averaged relaxation time of species m .

If the heat bath consists of different species, Lee proposes to take the molar averaged relaxation time over all different species s [Lee 1985a].

$$\tau_m = \frac{\sum_s \chi_s}{\sum_s \frac{\chi_s}{\tau_{m-s}}} \quad \text{for } s \neq e , \quad (\text{A.26})$$

where χ_s denotes the mole fraction of species s and τ_{m-s} is the inter-species relaxation time. To obtain the inter-species relaxation times τ_{m-s} , Millikan and White [1963] derived an expression on a semi-empirical basis, which is valid within a temperature range from 300 K to 9000 K, yielding:

$$\tau_{m-s} = \frac{101325.0}{p} \exp \left[0.00116 \mu_{m-s}^{\frac{1}{2}} \theta_m^{\frac{4}{3}} (T^{-1/3} - 0.015 \mu_{m-s}^{1/4}) - 18.42 \right] , \quad (\text{A.27})$$

where $\mu_{m-s} = \frac{M_s M_m}{M_s + M_m}$ is the reduced mass and θ_m is the characteristic vibrational temperature of species m , which can be found in Table A.2.

If expression (A.27) is used in equation (A.26), the average relaxation time τ_m is denoted as τ_m^{MW} , the Millikan and White relaxation time. For high temperatures ($T > 8000$ K), the Landau-Teller expression (A.25), used with the Millikan and White relaxation time expressed by equation (A.27), yields a relaxation rate that is too large, due to an overprediction of the collision cross-section. Therefore Park [1987] corrected the molar averaged Millikan and White relaxation time as follows:

$$\tau_m = \tau_m^{MW} + \tau_m^P . \quad (\text{A.28})$$

Park has proposed the following expression for the correction term τ_m^P ,

$$\tau_m^P = \frac{1}{\sigma_m \bar{c}_m n_m} , \quad (\text{A.29})$$

depending on the number density n_m , the average molecular velocity \bar{c}_m and the limiting cross-section σ_m . The average molecular velocity is defined as:

$$\bar{c}_m = \left(\frac{8\pi T}{\pi M_m} \right)^{\frac{1}{2}} . \quad (\text{A.30})$$

The limiting cross section σ_m is a measure of the probability for the collision process. Park proposed σ_m to be dependent of the temperature as follows:

$$\sigma_m = 10^{-21} \left(\frac{50000.0}{T} \right)^2 . \quad (\text{A.31})$$

A.4.2 Vibrational-Vibrational energy exchange

In a mixture of species, each diatomic species can be differently vibrationally excited. In this case species can exchange their vibrational energy between each other. This transfer of vibrational energy between the different molecules causes the vibrational energy to equalize. Term (9) of equation (2.9) accounts for this type of energy exchange. The model that describes this vibrational-vibrational energy exchange and which is applied in the present work, is proposed by Candler [1988].

According to Candler, the rate of vibrational energy transfer per unit volume from species r to species m may be formulated as follows:

$$Q_{V-V;r-m} = P_{r-m} Z_{r-m} \frac{e_{v_r} M_r}{\mathcal{N}} , \quad (\text{A.32})$$

where P_{r-m} is the probability of transferring vibrational energy from r to m , $\frac{e_{v_r} M_r}{\mathcal{N}}$ is the average vibrational energy per particle of species r with \mathcal{N} as Avogadro's number. The quantity Z_{r-m} is the number of $r - m$ collisions per unit time and volume.

From kinetic theory an expression for Z_{r-m} can be determined [Vincenti and Kruger 1965] as follows:

$$Z_{r-m} = n_m n_r \sigma_{r-m} \sqrt{\frac{8\mathcal{R}T}{\pi \mu_{r-m}}} . \quad (\text{A.33})$$

In this expression n_m and n_r appear as the number density of species m and r , respectively. Further μ_{r-m} is the reduced mass, and σ_{r-m} is the collision cross section. The collision cross section σ_{r-m} can be approximated by the product of the collision diameters, $d_m d_r$, of species m and r . The collision diameters are given in Table A.3. Inserting equation (A.33) into (A.32) yields:

$$Q_{V-V;r-m} = P_{r-m} \mathcal{N} \frac{\rho_m}{M_m} \rho_r \sigma_{r-m} \sqrt{\frac{8\mathcal{R}T}{\pi \mu_{m-r}}} e_{v_r} . \quad (\text{A.34})$$

The net vibrational energy change of species m per unit time and unit volume as a result of interaction with species r then becomes

$$[Q_{V-V;m,r}] = Q_{V-V;r-m} - Q_{V-V;m-r} . \quad (\text{A.35})$$

Summation over all different species r , yields for the energy transfer to species m :

$$Q_{V-V,m} = \sum_r [Q_{V-V;m,r}] . \quad (\text{A.36})$$

The probabilities for air, originating from the work of Taylor et al. [1967], have been presented in an exponential form by Park and Lee [1993]:

$$\begin{aligned} P_{N_2-NO} &= 5.5 \cdot 10^{-5} \left(\frac{T}{1000} \right)^{2.32} , \\ P_{N_2-O_2} &= 3.0 \cdot 10^{-6} \left(\frac{T}{1000} \right)^{2.87} , \\ P_{O_2-NO} &= P_{N_2-NO} . \end{aligned} \quad (\text{A.37})$$

The two probabilities P_{m-r} and P_{r-m} have to be coupled in such a way that the energy transfer $Q_{V-V,m}$ becomes zero as soon as the two vibrational temperatures T_{v_r} and T_{v_m} become equal. This results in the following relation between the probabilities, which are depending on both vibrational temperatures.

$$P_{m-r} = P_{r-m} \frac{M_r}{M_m} \sqrt{\frac{e_{v_r}(T_{v_r}) e_{v_r}(T_{v_m})}{e_{v_m}(T_{v_r}) e_{v_m}(T_{v_m})}} . \quad (\text{A.38})$$

Notice that the probabilities P_{m-r} given in equation (A.37) are small, implying that the influence of this coupling is rather unimportant in the case of air.

A.4.3 Translational-Electronic energy exchange

The energy transfer rate per unit volume between heavy particles (molecule, atom) and free electrons (term (14) of equation (2.9)) is given by Sutton and Sherman [1965]:

$$Q_{T-E} = 2n_e \left(\frac{3}{2}kT - \frac{3}{2}kT_e \right) M_e \sum_{s \neq e} \frac{\nu_{e-s}}{M_s} , \quad (\text{A.39})$$

where n_e is the number density of the electrons. Collisions between electrons and heavy particles cause a change in translational energy of the electrons. According to Lee [1985a], the effective collision frequency, ν_{e-s} is expressed as:

$$\nu_{e-s} = n_s \sigma_{e-s} \sqrt{\frac{8\mathcal{R}T_e}{\pi M_e}} . \quad (\text{A.40})$$

The effective collision cross-section σ_{e-s} between an electron and a heavy particle s depends on the fact whether the heavy particle is charged or neutral.

For the case of charged particles the effective collision cross-section is given by [Petschek and Byron 1957; Yos 1963]:

$$\sigma_{e-ion} = \frac{8}{3}\pi \frac{e^4}{(3kT_e)^2} \ln \left[1 + \frac{l^2(3kT_e)^2}{e^4} \right] , \quad (\text{A.41})$$

where $e = 1.609 \cdot 10^{-19}$. C denotes the magnitude of the electronic charge and l is Debye shielding length, at which the electrostatic field is truncated.

$$l^2 = \frac{\epsilon_0 k T_e}{n_e e^2} . \quad (\text{A.42})$$

The quantity ϵ_0 is the permittivity of vacuum and has a value $8.854 \cdot 10^{-12} \frac{C^2}{J m}$. If positive and negative charged particles were distributed completely random, this distribution would have no electrostatic energy, since on the average, attractive configurations would be exactly balanced by the repulsive ones. This is not the physical situation, since in the immediate neighborhood of an positive ion, an negative charged particle is more likely to be found than another positive one. The thermal motions effectively prevent any complete ordering and the final situation is a dynamic compromise between the electrostatic interactions tending to produce ordered configurations and the kinetic collisions tending to destroy them. The Debye-Hückel theory yields a radius beyond which there is no noticeable electrostatic energy any more.

For electron-neutral interactions, the effective electron-neutral collision cross-section is described by Lee [1985a]

$$\sigma_{e-s} = \tilde{a}_s + \tilde{b}_s T_e + \tilde{c}_s T_e^2, \quad s \neq \text{ion} . \quad (\text{A.43})$$

The constants \tilde{a}_s , \tilde{b}_s and \tilde{c}_s for equation (A.43) are presented in Table A.3. The curve fit was generated by Gupta et al. [1989] from experimental effective collision cross-section data.

species	\tilde{a}_s	\tilde{b}_s	\tilde{c}_s	d_s
N ₂	7.5E-20	5.5E-24	-1.0E-28	3,709E-10
O ₂	2.0E-20	6.0E-24	0	3,608E-10
NO	1.0E-19	0	0	3,534E-10
N	5.0E-20	0	0	-
O	1.2E-20	1.7E-24	-2.0E-29	-
N ₂ ⁺	-	-	-	3,709E-10
O ₂ ⁺	-	-	-	3,608E-10
NO ⁺	-	-	-	3,534E-10

Table A.3: Constants in expressions for collision cross-section determination

A.4.4 Vibrational-Electronic energy exchange

Similar to the vibrational-translational energy transfer, Lee [1985b] derived a rate equation for the electronic-vibrational energy exchange (term (7) and (17) of equation (2.9)):

$$Q_{V-E} = \rho_m \frac{e_{v_m}(T_e) - e_{v_m}(T_{v_m})}{\tau_{e_m}} , \quad (\text{A.44})$$

where e_{v_m} is the vibrational energy of species m and e_{v_m} is the vibrational energy evaluated at temperature T_e .

The derivation is based on a method to describe the V-E process accounting for multiple-quantum level transitions. Lee [1985b] derived an expression for the relaxation time, τ_{e_m} , of V-E energy transfer. A curve fit of τ_{e_m} , generated by Candler [1988] based on the results of Lee for nitrogen, lists:

$${}^{10} \log(p_e \tau_{e_{N_2}}) = \begin{cases} 7,50 ({}^{10} \log T_e)^2 - 57,0 {}^{10} \log T_e + 98,70 & T_e \leq 7000\text{K} \\ 2,36 ({}^{10} \log T_e)^2 - 17,9 {}^{10} \log T_e + 24,35 & T_e \geq 7000\text{K} \end{cases},$$

where p_e is the electron pressure in atmosphere and $\tau_{e_{N_2}}$ is the relaxation time of nitrogen in seconds. At values of T_e of about 7000 K the relaxation time is smallest due to a strong resonance between the electron and vibrational modes, away from this temperature it increases strongly. Only the relaxation time for N_2 is taken into account. According to Park and Lee [1993], the relaxation times for O_2 and NO in a collision with free electrons are about 300 times faster than for N_2 . Therefore, in this work only the V-E coupling for N_2 is modeled.

A.5 Energy, enthalpy and specific heat

To compute aerothermodynamic flow fields accurately, the energy contained in a molecule and the derived quantities such as specific heat, enthalpy and entropy have to be known for the appropriate range of temperatures. Accurate data is known only for temperatures lower than $6000K$, but during an earth re-entry, temperatures can rise up to $25000K$. For these high temperatures, diatomic species can still exist in nonequilibrium situations, for example in a shock layer. In the literature c_p data may be found from the work of Browne [1962], Balakrishnan [1986], Jaffe [1987], Gurvich et al. [1989] and Capitelli et al. [1994].

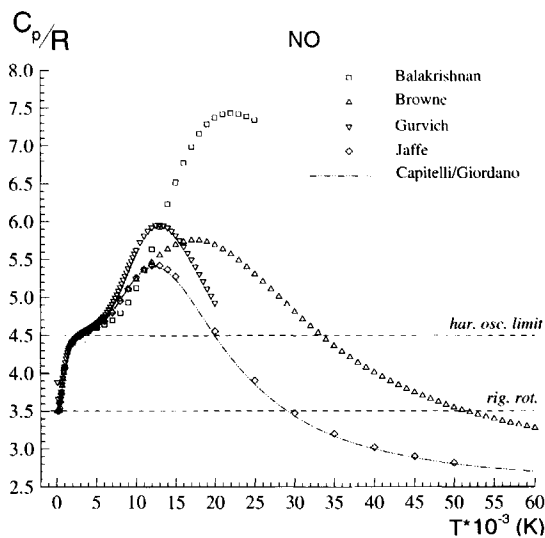


Figure A.2: Specific heat values for NO.

For example, the available c_p data for *NO* has been assembled in Figure A.2. In the low temperature range up to $6000K$, the c_p -values agree reasonably well, however they diverge substantially beyond $T > 10000K$ and can differ up to a factor of two. The questions are: what could be the cause of all these differences, what will be the influence of these differences on the computational results and which data set is appropriate for the calculations. Concerning the first question the differences at high temperatures can be attributed to the use of different spectroscopic data as well as to the possible inclusion of the high-lying excited electronic states. The largest difference appears between Balakrishnan and the others. As stated by Jaffe, the expressions used by Balakrishnan for computing the partition functions and specific heats are not sufficiently accurate for the high temperatures considered. In addition, Balakrishnan does not properly allow for the dissociation of diatomic species, nor does he adequately address the separability of the vibrational and rotational energy. Jaffe explains

more in depth his method in deriving the specific heats.

To answer the second question, i.e. the influence of the various specific heat coefficient models on the computational results, a well documented and validated data set is mandatory. So it has been decided to perform an analysis on how the energy contained in a molecule is modeled whereby the underlying assumptions will be discussed. Based on these observations a method is described, yielding c_p data that are used in this thesis.

For temperatures larger than 5 K, the energy of the molecules is distributed over so many energy levels, that a Boltzmann distribution of the molecules over the energy levels can be assumed. A Boltzmann distribution for a system of N molecules in thermodynamic equilibrium has the form [Vincenti and Kruger 1965]:

$$\frac{N_j}{N} = \frac{g_j e^{-\frac{\epsilon_j}{kT}}}{Q} , \quad (\text{A.45})$$

where N_j is the number of molecules in a given energy level ϵ_j , and k denotes the Boltzmann constant. In principle each discrete energy level ϵ_j has a certain number of degenerate states, g_j . The partition function Q is defined as:

$$Q = \sum_j g_j e^{-\frac{\epsilon_j}{kT}} . \quad (\text{A.46})$$

The average energy per unit mass of species s can be written as [Vincenti and Kruger 1965]:

$$e_s = \frac{1}{M} \sum_j \epsilon_j N_j = R_s T^2 \left(\frac{\partial \ln Q(T)}{\partial T} \right)_V , \quad (\text{A.47})$$

where M is the mass of the system of N molecules.

In order to calculate the energy of a molecular species, the energy levels of the molecule have to be known. Molecular spectroscopy shows that the internal energy levels can be organized into a set of widely separated groups where each group corresponds to a specific electronic state of the molecule. Within each group the levels can be decomposed into a common electronic part but different vibrational and rotational parts. This vibrational contribution shows nearly equal intervals, whereas the rotational contribution is separated by larger intervals with increasing rotational energy. The structure of the internal energy levels suggests the separation of the energy of the molecule into electronic vibrational and rotational modes. If this can be assumed, the total energy level including the translational mode becomes:

$$\epsilon_j = \epsilon_j^{el} + \epsilon_j^{vib} + \epsilon_j^{rot} + \epsilon_j^{tr} . \quad (\text{A.48})$$

Due to the separation, the partition function can be decomposed into the product of partition functions of each mode:

$$Q(T) = Q^{tr} \times Q^{rot} \times Q^{vib} \times Q^{el} . \quad (\text{A.49})$$

In the next section the different energy contributions will be described shortly.

A.5.1 Translational mode

The translational energy levels ϵ_j^{tr} are [Pauling and Wilson 1985]:

$$\epsilon_j^{tr} = \epsilon_{j_x j_y j_z} = \frac{h^2}{8M} \left(\frac{j_x}{a_x} + \frac{j_y}{a_y} + \frac{j_z}{a_z} \right), \quad j_x, j_y, j_z = 1, \dots, \infty. \quad (\text{A.50})$$

where j_x, j_y, j_z are the quantum numbers, a_x, a_y, a_z are linear dimensions which describe the size of the system, and M denotes the mass of the molecule. The expression for the translation partition function becomes:

$$Q^{tr} = \sum_{j_x=1}^{\infty} \sum_{j_y=1}^{\infty} \sum_{j_z=1}^{\infty} e^{-\frac{\epsilon_{j_x j_y j_z}}{kT}}. \quad (\text{A.51})$$

Because of the close spacings between the translational energies, the summation can be replaced by an integral which yields [Vincenti and Kruger 1965]:

$$Q^{tr} = \left[\frac{2\pi M k T}{h^2} \right]^{\frac{3}{2}} V, \quad (\text{A.52})$$

where $V = a_x a_y a_z$ is the volume of the system. Using equation (A.47), the translational energy of species s can be evaluated:

$$e_s^{tr} = \frac{3}{2} R_s T. \quad (\text{A.53})$$

A.5.2 Electronic mode

In order to evaluate the electronic partition function, no closed-form expression analogous to the translational mode can be found. From the definition (A.45) the electronic partition function follows as:

$$Q_s^{el} = \sum_{n=0}^{n_{max}} g_{n,s} e^{-\frac{\epsilon_n^{el}}{kT_e}}, \quad (\text{A.54})$$

in which $g_{n,s}$ denotes the degeneration of the electronic modes. Including the characteristic temperature $\Theta_s^{el}(n) = \frac{\epsilon_n^{el}}{k}$ of the specific electronic state n we find:

$$e_{e_s} = \frac{R_s}{Q_s^{el}} \sum_{n=0}^{n_{max}} g_{n,s} \Theta_s^{el}(n) e^{-\frac{\Theta_s^{el}(n)}{T_e}}. \quad (\text{A.55})$$

The characteristic temperatures for the electronic states are specified in Park [1990].

A.5.3 Rotational- and vibrational mode

The decomposition of the internal energy into separate modes, inspired Born and Oppenheimer [1927] to split the Schrödinger wave equation into an *electronic wave equation* and a *rotational-vibrational wave equation*.

In the first step, one solves the *electronic wave equation* with fixed nuclei for all possible configurations of the nuclei. As a result the electronic energy u_n of the electronic state n is a continuous function of the internuclear distance r . Secondly, having evaluated the potential energy function $u_n(r)$, one now solves the *rotational-vibrational wave equation* for the nuclei alone, where the electronic energy appears as a potential energy function $u_n(r)$ for the electronic state n .

The theoretical calculation of the potential energy function $u_n(r)$ for molecules other than molecular hydrogen is a formidable task and therefore, usually $u_n(r)$ is determined empirically on the basis of observed and calculated energy levels. When $u_n(r)$ is determined, the wave equation for the rotation and vibration for a diatomic molecule can be solved.

In the next two subsections, the solution of the rotational-vibrational wave equation equation is presented for two cases: the simple Hooke potential energy function and the more complicated Hulbert-Hirschfelder potential energy function. The latter option can not be solved analytically.

A.5.3.1 Hooke potential energy function

The simplest assumption of the force between the atoms of a diatomic molecule can be expressed to be proportional to the displacement of the intermolecular distance from its equilibrium value r_e . The corresponding potential energy function then reads:

$$u_{n,Hooke}(r) = \frac{1}{2}k_n(r - r_e)^2 \quad . \quad (\text{A.56})$$

The constant k_n will be chosen such that $u_{n,Hooke}(r)$ approaches the 'true' measured potential $u_n(r)$ near $r = r_e$ for the specific electronic state n . This will lead to the following result for the combined rotation-vibration energy levels $\epsilon_{K,v}^{int}$ for an electronic state n [Pauling and Wilson 1985]:

$$\epsilon_{K,v}^{int} = K(K+1) \frac{h^2}{8\pi^2\mu r_e^2} + \left(v + \frac{1}{2}\right) h\nu_e - \frac{K^2(K+1)^2 h^4}{128\pi^6\nu_e^2\mu^3} \quad , \quad (\text{A.57})$$

with h Planck's constant, v the quantum vibration number, K the quantum rotation number and $\nu_e = \frac{1}{2\pi}\sqrt{\frac{k}{\mu}}$ denotes the vibrational frequency of the molecule. The first term is the energy of rotation, assuming that the molecule is a rigid body. The second term is the vibrational energy of the molecule, considered as an harmonic oscillator. The third term accounts

for the stretching of the actual non-rigid molecule due to rotation. Note that in this case rotation and vibration are decoupled:

$$\begin{aligned}\epsilon_K^{rot} &= K(K+1) \frac{\hbar^2}{8\pi^2\mu r_e^2} - \frac{K^2(K+1)^2\hbar^4}{128\pi^6\nu_e^2\mu^3} , \\ \epsilon_v^{vib} &= (v + \frac{1}{2}) \hbar\nu_e .\end{aligned}\quad (\text{A.58})$$

Neglecting the non-rigid effect on rotation and assuming a Boltzmann distribution, the rotation and vibration energy become:

$$\begin{aligned}e_{rot_s} &= R_s T , \\ e_{v_s} &= \frac{\theta_s R_s}{e^{\frac{\theta_s}{T}} - 1} ,\end{aligned}\quad (\text{A.59})$$

in which the characteristic temperature θ_s equals $\frac{\hbar\nu_e}{k}$.

Since the vibration energy can not be higher than the dissociation energy, the energy will be cut off at its dissociation energy value:

$$e_{v_s} = \frac{\theta_s R_s}{e^{\frac{\theta_s}{T}} - 1} - \frac{\theta_d R_s}{e^{\frac{\theta_d}{T}} - 1} .\quad (\text{A.60})$$

A more accurate model will be described next.

A.5.3.2 The Hulbert-Hirschfelder potential energy function

For the Hooke potential energy function all energy levels are equally spaced, whereas the observed vibrational levels show a convergence for increasing values of ν . The five parameter Hulbert and Hirschfelder [1941] potential energy function u_{HH} for diatomic molecules accounts for this effect and gives a better approximation for the vibrational and rotational energy levels. Furthermore, the harmonic oscillator model assumes that at a deviation from the equilibrium atom distance the attractive force and the repulsive force are of the same magnitude. For larger deviations from the equilibrium atom distance the attractive force is smaller than the repulsive force. Above a certain vibrational energy level the attractive force is negligible and dissociation occurs.

Because the potential is deformed by centrifugal forces created by the rotational motions, it is common to represent the potential of a rotating-vibrating diatomic molecule by an effective potential u_{eff} , which is simply the rotationless potential u_{HH} plus a centrifugal term (see Jaffe [1987]):

$$u_{eff}(r, K) = u_{HH}(r) + \frac{K(K+1)\hbar^2}{8\pi^2\mu r^2} .\quad (\text{A.61})$$

In Figure A.3 the potential energy curve of N_2 is shown for several rotation quantum numbers, K . The centrifugal force introduces a shift to larger bond lengths and lowers the dissociation energy with increasing rotation quantum number K . If the rotation quantum number

is increased to $K = K_{max}$ the minimum and the maximum join and beyond this level the effective potential becomes completely repulsive.

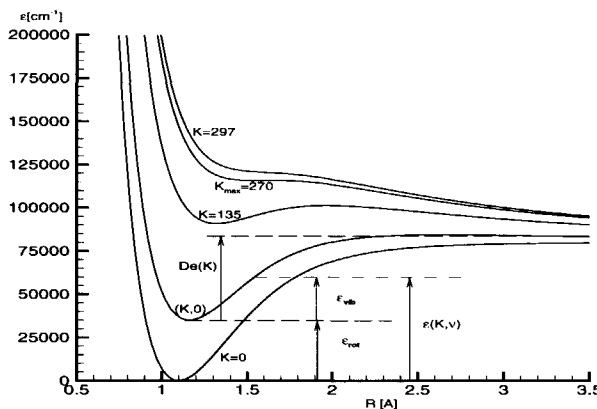


Figure A.3: Effective electronic energy potential of N_2 for different quantum rotational numbers K .

The vibrational quantum numbers for the effective potential are approximated by the so-called Dunham expansion [Herzberg 1950]:

$$\epsilon_{dun}^{vib}(v) = \omega_e \left(\frac{1}{2} + v \right) - \omega_e x_e \left(\frac{1}{2} + v \right)^2 . \quad (A.62)$$

Since the spectroscopic constants ω_e , $\omega_e x_e$ and α_e are given for rotational level $K=0$, the constants for higher K can be expressed as a function of higher derivatives at the minimum at the effective potential from the classical expressions [Steele et al. 1962]. Determining analytically the minimum of the effective potential, the wave numbers for the combined rotation-vibration wave numbers can be found:

$$\epsilon_{K,v}^{int} = u_{eff(r,K)} h c + \omega_e(K) \left(\frac{1}{2} + v \right) - \omega_e x_e(K) \left(\frac{1}{2} + v \right)^2 . \quad (A.63)$$

The maximum vibration quantum number $v_{max,K}$ will be defined at $\epsilon_{K,v}$ which is equal to the local maximum of the effective potential at rotational level K . Summing over all the electronic excited states denoted by n , the partition function for the combined electronic, vibration and rotation can be written as [Jaffe 1987]:

$$Q^{int} = \sum_{n=0}^{n_{max}} \sum_{K=0}^{K_{max}(n)} \sum_{v=0}^{v_{max}(n,K)} \left\{ g_n \sigma (2K+1) e^{-\frac{\epsilon_{n,K,v}}{kT}} \right\}, \quad (A.64)$$

where g_n is the degeneracy of electronic level n , σ the symmetry factor which equals $\frac{1}{2}$ for homo-nuclear and 1 for heteronuclear molecules. The degeneracy of the rotation is $2K + 1$. The energy can now be evaluated:

$$\frac{e_s^{int}}{R_s} = \frac{1}{Q^{int}} \sum_{n=0}^{n_{max}} \sum_{K=0}^{K_{max}(n)} \sum_{v=0}^{v_{max}(n,K)} \left\{ \frac{g_n}{k} \sigma (2K+1) \epsilon_{n,K,v} e^{-\frac{\epsilon_{n,K,v}}{kT}} \right\} . \quad (\text{A.65})$$

The problem with the Hulbert-Hirschfelder potential is to define the internal partitioning of the rotational and the vibrational energy. The energy of a molecule in the v^{th} vibrational level and K^{th} rotational level ($E_{v,K}$) is well defined, but not the partitioning into its rotational and vibrational components. One can consider either that the rotational levels are perturbed by vibration or that the vibrational energy levels are perturbed by rotation. The choice will have a very small effect on the energy and the specific heat (see Jaffe [1987]). The latter one is chosen, so that the rotational energy for a molecule in the K^{th} rotational level, is defined by the difference between the minimum on the rotating $u_K(r)$ and the value without rotation $u_{K=0}(r)$, see Figure A.3. Now the vibrational energy is uniquely defined as the energy above the minimum on the effective potential energy curve for a rotating molecule. The dissociation energy, $D_e(n, K)$, of the rotating molecule is defined as the energy difference between the minimum and the centrifugal barrier.

The internal partition function can be calculated for thermal nonequilibrium from the expression:

$$\begin{aligned} Q^{int} &= Q^{el} \times Q^{rot} \times Q^{vib} \\ &= \left[\sum_{n=0}^{n_{max}} g_n e^{-\frac{\Theta_s^{el}(n)}{kT_e}} \right] \left[\sum_{K=0}^{K_{max}(n)} \sigma (2K+1) e^{-\frac{\epsilon_{rot}(n,K)}{kT_{rot}}} \right] \left[\sum_{v=0}^{v_{max}(n,K)} e^{-\frac{\epsilon_{vib}(n,K,v)}{kT_v}} \right] . \end{aligned} \quad (\text{A.66})$$

In thermal nonequilibrium it is assumed that each of the different energies modes is a function of a corresponding temperature (T_e , T_{rot} and T_v). The energies become:

$$\begin{aligned} \frac{e_{e_s}}{R_s} &= \frac{1}{Q^{el}} \sum_{n=0}^{n_{max}} \frac{g_n}{k} \Theta_s^{el}(n) e^{-\frac{\Theta_s^{el}(n)}{kT_e}} , \\ \frac{e_{rot_s}}{R_s} &= \frac{1}{Q^{rot}} \sum_{K=0}^{K_{max}(n)} \epsilon^{rot}(n, K) \sigma (2K+1) e^{-\frac{\epsilon^{rot}(n,K)}{kT_{rot}}} , \\ \frac{e_{v_s}}{R_s} &= \frac{1}{Q^{vib}} \sum_{v=0}^{v_{max}(n,K)} \epsilon^{vib}(n, K, v) e^{-\frac{\epsilon^{vib}(n,K,v)}{kT_v}} . \end{aligned} \quad (\text{A.67})$$

The energies e_{e_s} , e_{rot_s} and e_{v_s} are a function of their own temperature.

Specific heat values c_p are determined by differentiation of the internal energy according to:

$$c_p^{int} = \frac{E_s^{int}(T + dT) - E_s^{int}(T - dT)}{2dT} . \quad (\text{A.68})$$

In order to be compatible with the CHEMKIN data base [Kee et al. 1987], the c_p values are fitted with a $(n - 1)$ th degree polynomial, where n is usually taken to be 5:

$$\frac{c_{p_s}}{R_s} = \sum_{k=1}^n (A_k^s T^{k-1}). \quad (\text{A.69})$$

These fitted c_p data are used in the numerical solver.

Thermal nonequilibrium computations require also the electronic, rotational and vibrational c_p as a function of its own temperature. Therefore it has been decided to fit the electronic and rotational enthalpy of an polyatomic molecule in the same manner as the total enthalpy of the species. The electronic c_p of an atomic and the vibrational c_p of a polyatomic molecule can be computed through the following relations:

$$\begin{aligned} c_{p,e_s}(T_e) &= c_{p_s}(T_e) - \frac{5}{2}R_s, && \text{for atomic species} \\ c_{p,v_s}(T_{v_s}) &= c_{p_s}(T_{v_s}) - c_{p,e_s}(T_{v_s}) - c_{p,rot_s}(T_{v_s}) - \frac{5}{2}R_s. && \text{for diatomic species} \end{aligned} \quad (\text{A.70})$$

Now it is easy to integrate the c_p values to obtain the enthalpies and entropies of the species.

$$\frac{h_s}{R_s T} = \frac{1}{R_s T} \int_{T_{ref}}^T c_{p_s} dT + h_{0_s} = \sum_{k=1}^n \left(A_k^s \frac{T^{k-1}}{k} \right) + \frac{A_{n+1}^s}{T}, \quad (\text{A.71})$$

$$\frac{s_s}{R_s} = \int_{T_{ref}}^T \frac{c_{p_s}}{R_s T} dT + s_{T_{ref,s}} = A_1^s \ln T + \sum_{k=2}^n \left(A_k^s \frac{T^{k-1}}{k-1} \right) + A_{n+2}^s. \quad (\text{A.72})$$

in which h_{0_s} is the formation enthalpy per unit of mass. The formation enthalpy h_{0_s} is defined at the reference-temperature $T_{ref} = 298.15$ K; s_s is the entropy at 1 bar and $s_{T_{ref,s}}$ the absolute entropy at 1 bar and $T = T_{ref}$.

A.5.4 Comparison of different models for specific heats

The resulting c_p values for several constituents as a function of temperature are plotted in Figures A.4 till A.7. In these figures, the c_p 's calculated from Hooke's energy potential function in which only 2 excited states are taken into account and the Hulbert-Hirschfelder model, as described above, are compared with the data from literature. It is clear that for temperatures higher than 5000 K, Hooke's model is not valid anymore. The computed c_p 's agree reasonably well with the ones from Jaffe, Gurvich and Capitelli. The c_p 's from Browne and Balakrishnan deviate at higher temperatures from the others.

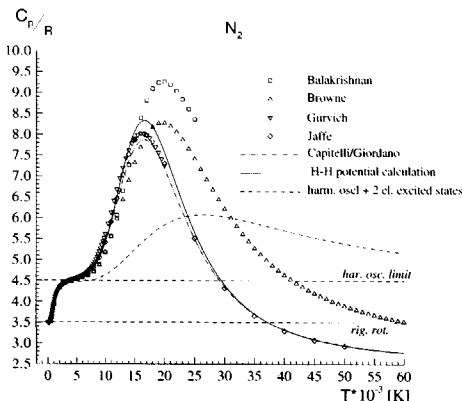


Figure A.4: Specific heat values for N₂.

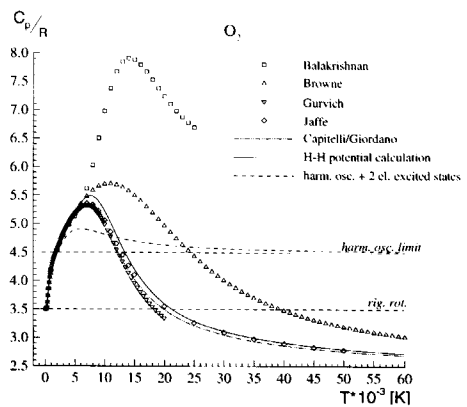


Figure A.5: Specific heat values for O₂.

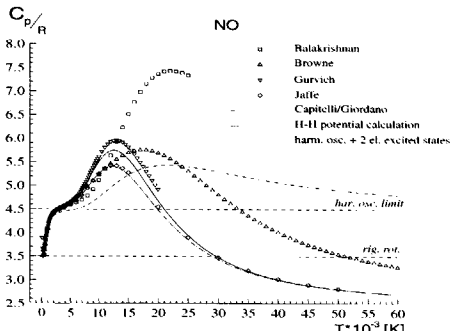


Figure A.6: Specific heat values for NO.

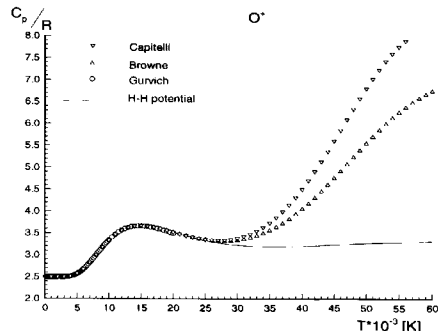


Figure A.7: Specific heat values for O⁺.

A.6 Transport properties

A.6.1 Viscosity

The viscosity of each species s is found using the Blottner viscosity model, which is a curve fit of experimental data as a function of temperature, see Blottner et al. [1971].

$$\mu_s = 0.1 \exp [(A_s \ln T + B_s) \ln T + C_s], \quad (\text{A.73})$$

The constants A_s , B_s and C_s are presented in table A.4. The global viscosity of the gas mixture can be calculated from the species viscosities using Wilke's rule [Wilke 1950]. The complete model is appropriate for temperatures up to 10.000 K.

$$\mu = \sum_s \frac{\chi_s \mu_s}{\sum_r \chi_r \phi_{sr}}, \quad (\text{A.74})$$

where χ_s is molar concentration and ϕ_{sr} is

$$\phi_{sr} = \frac{1}{\sqrt{8}} \left(1 + \frac{M_s}{M_r} \right)^{-\frac{1}{2}} \left[1 + \left(\frac{\mu_s}{\mu_r} \right)^{\frac{1}{2}} \left(\frac{M_r}{M_s} \right)^{\frac{1}{4}} \right]^2. \quad (\text{A.75})$$

Species	A_s	B_s	C_s
N2	0.0268142	0.3177838	-11.3155513
N	0.0115572	0.6031679	-12.4327495
O2	0.0449290	-0.0826158	-9.2019475
O	0.0203144	0.4294404	-11.6031403
NO	0.0436378	-0.0335511	-9.5767430
N2+	0.0268142	0.3177838	-11.3155513
N+	0.0115572	0.4294404	-12.4327495
O2+	0.0449290	-0.0826158	-9.2019475
O+	0.0203144	0.4294404	-11.6031403
NO+	0.0436378	-0.0335511	-9.5767430
E-	0.0436378	-0.0335511	-9.5767430

Table A.4: Blottner's coefficients Blottner et al. [1971]

A.6.2 Diffusion

It is assumed that the diffusion velocity is determined only by the gradient of mass fraction. Pressure diffusion and temperature diffusion are neglected, because in gas dynamic problems their contributions are small compared to the diffusion due to mass fraction gradients.

Because of the mass fraction gradients, there is a mass motion of species s which is defined as the diffusion velocity \hat{u}_s of species s . The corresponding mass flux is approximated by Fick's law as:

$$\rho_s \hat{u}_s = -\rho D \vec{\nabla} c_s . \quad (\text{A.76})$$

The diffusion coefficient D is given by:

$$D = \frac{Le}{\sum_s \rho_s c_{p_s}} k_{tr_s} . \quad (\text{A.77})$$

The Lewis number Le is the ratio for energy transfer between diffusion and heat conduction. k_{tr_s} is the translational conductivity and c_{p_s} is the specific heat at constant pressure of species s . Le , is taken between 1.0 and 1.4 for neutral species and doubled for the corresponding charged species.

A.6.3 Conductivities

For a chemically reacting viscous flow, there is energy transport due to thermal conduction \vec{q}_T , due to diffusion \vec{q}_d and due to radiation \vec{q}_r . In this work we neglect \vec{q}_r . Therefore the total energy flux \vec{q} is given by:

$$\begin{aligned} \vec{q} &= \vec{q}_T + \vec{q}_d \\ &= \left[k_{tr} \vec{\nabla} T + c_m k_{v_m} \vec{\nabla} T_{v_m} + c_e k_e \vec{\nabla} T_e \right] + \left[\rho \sum_s h_s D \vec{\nabla} c_s \right]. \end{aligned} \quad (\text{A.78})$$

The energy flux due to diffusion \vec{q}_d , occurs when the species s diffuses through the gas and carry their enthalpy h_s .

The conductivities k_{tr} , k_{v_m} and k_e are calculated from species viscosities using the Eucken formula [Vincenti and Kruger 1965]:

$$\begin{aligned} k_{tr_s} &= \mu_s \left(\frac{5}{2} c_{v_{tr_s}} + c_{v_{rot_s}} \right) , \\ k_{v_m} &= \mu_m c_{v_m} , \\ k_e &= \mu_s \left(\frac{5}{2} c_{v_{e_s}} \right) . \end{aligned} \quad (\text{A.79})$$

For the global translational and vibrational conductivity of the mixture Wilke's rule is ap-

plied.

$$k_{tr} = \sum_s \frac{k_{tr_s} \chi_s}{\sum_r \chi_r \phi_{sr}} ,$$
$$k_v = \sum_s \frac{k_{v_s} \chi_s}{\sum_r \chi_r \phi_{sr}} , \quad (A.80)$$

where ϕ_{sr} is defined in equation (A.75).

B

Partial catalytic wall condition

For simple reactions, without thermodynamically unstable intermediate products, the catalyst increases both reaction velocities (forward and backward) in such a manner that the ratio k_f/k_b does not change. The effect of the catalyst is to increase the reaction velocities for an assigned temperature or to decrease the temperature at which the reaction achieves a given rate. In the specific case of heterogeneous catalysis there is a phase boundary separating the catalyst from the reactants. This is the case in hypersonic flows where dissociated gas impinging on a solid surface can act as catalyst for recombination processes. The heterogeneous catalysis process can be described in 5 elementary steps:

1. diffusion of reactants to the surface;
2. adsorption of reactants to the surface;
3. chemical reactions at the surface;
4. desorption of products from the surface;
5. diffusion of products from the surface.

Each of these steps has a different velocity and the slower one is determining the process rate. Step 1 and 5 are usually fast, except when the catalyst is very efficient. In this case the limit for the catalytic reaction rate is the quantity of reactants that goes to the wall and the surface reaction rates become independent from the kinetics properties of the surface. It is called "diffusion controlled" catalysis. The surface used in thermal protection systems (TPS) are usually bad catalysts, which means that the assumption on step 1 and 5 is applicable.

The quantity which characterize the catalytic efficiency of a solid catalyst is the recombination coefficient:

$$\gamma = \frac{\text{flux of atoms recombining at surface}}{\text{flux of atoms impinging on the surface}} = \frac{Z_{a,rec}}{Z_a} . \quad (\text{B.1})$$

γ represents the recombination probability for an atom impinging on the surface. For a finite catalytic wall the catalytic coefficient γ varies between 0 and 1 corresponding in the limit to

a non-catalytic and fully-catalytic wall. Once γ is known the chemical wall source terms can be calculated. The catalytic efficiency of a surface can be modeled or fitted with experiments. The modeling approach is based on the study of elementary processes (adsorption, reaction desorption) involved in the phenomenon. A series of models exists in the literature. [Barbato and Bruno 1996; Jumper et al. 1993; Deutschmann et al. 1994]

In this work the fitted recombination coefficients of Stewart et al. [1991] are used in which Reaction Cured Glass (RCG) material is chosen since they were used for the shuttle. The values below 1000 K were calculated using kinetic theory by Kim [1988]. Above 1000K the values were taken from measured stagnation point heat transfer rates taken from blunt nose cones in arc-jet hypersonic flows. The values as a function of temperature are given below:

$$\gamma_N = \begin{cases} 1.1 \cdot 10^{-3} T_{wall} & T_{wall} \leq 1302K \\ 100e^{\frac{-14871}{T_{wall}}} & 1302 \leq T_{wall} \leq 1625 \\ 6.2 \cdot 10^{-6} e^{\frac{12100}{T_{wall}}} & T_{wall} \geq 1625K \end{cases}, \quad (B.2)$$

$$\gamma_O = \begin{cases} 1.4 \cdot 10^{-3} e^{\frac{-560}{T_{wall}}} & T_{wall} \leq 880K \\ 1.75e^{\frac{-6833}{T_{wall}}} & 880 \leq T_{wall} \leq 1603K \\ 39 \cdot 10^{-9} e^{\frac{21410}{T_{wall}}} & T_{wall} \geq 1603K \end{cases}.$$

For the RCG material around 1700 K the maximum values of γ are reached such that the most catalytic effects are encountered.

The link between the modeling of heterogeneous catalysis and CFD passes through specific boundary conditions. The no slip condition at the wall means that the fluid particles must have zero velocity at the wall. Even when the flow velocity is zero, the mass flux of a chemical species can be different from zero because of diffusive effect. The diffusive flux J_s of a species s , assuming Fick's law for binary diffusion reads:

$$\vec{J}_s = \rho_s \hat{u}_s = -\rho D_s \vec{\nabla} c_s, \quad (B.3)$$

where we see the diffusion velocity \hat{u}_s of species s , the density ρ_s and the diffusion coefficient D_s . To write the boundary condition for a catalytic wall we start from equation (B.3) written for the y direction:

$$(\rho_s v_s)_w = - \left(\rho D_s \frac{\partial c_s}{\partial y} \right)_w, \quad (B.4)$$

where the subscript w indicates that those quantities are computed at the wall.

We note that for the mass species conservation law at steady state, the diffusive flux of one species to/from the wall is equal to the consumption/production rate of the same species there:

$$(\dot{w}_s)_w = -(\rho_s v_s)_w . \quad (\text{B.5})$$

Substituting equation (B.5) into equation (B.4) yields the wall catalytic boundary condition for each species s [Anderson 1989]:

$$(\dot{w}_s)_w = \left(\rho D_s \frac{\partial c_s}{\partial y} \right)_w \quad \text{catalytic wall} . \quad (\text{B.6})$$

From equation (B.6), we obtain directly the boundary condition for a non-catalytic wall; in such a case there is no species production at the wall, $\dot{w}_s = 0$ for each s , and therefore:

$$\left(\frac{\partial c_s}{\partial y} \right)_w = 0 \quad \text{non-catalytic wall} , \quad (\text{B.7})$$

because ρ and D_s are obviously non-zero. So, for a non-catalytic wall the wall mass fraction gradient must be zero for each species s .

Now the source term \dot{w}_s for the species s is linked with the catalytic properties of the surface. To simplify the following exposition we consider a gas mixture of atoms a and molecules a_2 . A classical expression for the atom source term for a catalytic wall was proposed by Goulard [1958]:

$$\dot{w}_a = K_{w,a} (\rho_w c_{wa})^m , \quad (\text{B.8})$$

where $K_{w,a}$ is the *catalytic reaction rate constant* or *catalyticity*, that is a surface characteristic, and m is the reaction order. This expression represents also a definition for the catalytic reaction rate. In fact, the catalyticity is defined as the constant factor by which the gas phase density (n_a) must be multiplied to obtain the surface rate of conversion of atoms into molecules per unit area and unit time [Scott 1987]¹:

$$Z_{a,rec} = K_{w,a} n_a . \quad (\text{B.9})$$

Now, multiplying equation (B.9) for the atom mass m_a and observing that, for the conservation law, the flux of recombined atoms must be equal to the net flux of atoms going into the surface, equation (B.5), we have:

¹Typically, in the literature, m is assumed to equal unity. If this is so, by defining a K_w depending on surface properties and T_w only, equation (B.8) implies that the recombination reaction is *first order* in gas concentration.

$$\dot{w}_a = K_{w,a} n_a m_a , \quad (B.10)$$

which, using $n_a m_a = \rho_w c_{wa}$, becomes the equation (B.8) for a first order process.

At this point we have seen two quantities that characterize surface recombination: the recombination coefficient γ and the catalyticity K_w . To express the relation between them we can start from the definition of the recombination coefficient equation (B.1). Using equation (B.9), the flux of particle striking (impinging) yields:

$$Z_a = \frac{n k T}{\sqrt{2 \pi m_a k T}} . \quad (B.11)$$

(k is the Boltzmann constant, m_a the particle mass, n the particles number density) we have:

$$K_{w,a} = \gamma \sqrt{\frac{k T_w}{2 \pi m_a}} . \quad (B.12)$$

C

Description of F4 and HEG wind tunnel

C.1 Description of hot-shot tunnel F4

The only major hot-shot wind tunnel operational is the F4 at ONERA, France. Figure C.1 represents a schematic view of the facility.

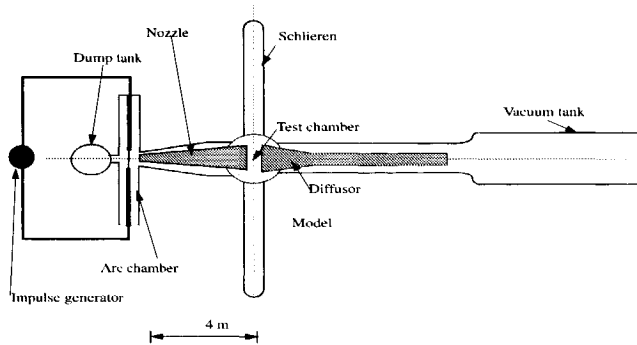


Figure C.1: Schematic view of the F4 arc jet wind tunnel in Le Fauga.

In the F4, the cold test gas is confined at 10 to 100 bar in the finite reservoir, which is a cylindrical arc chamber. The test gas is heated by passing a strong current through it. To obtain the desired total conditions the impulse generator provides the current and can deliver about 150 MW during a few milliseconds. When the gas, which is heated in a non-uniform manner, has reached the prescribed total conditions, the electric supply is shut down and after a few milliseconds the nozzle throat is opened by firing a pyrotechnic plug from the nozzle throat. The blow down mode starts and is interrupted by firing a pyrotechnic valve located in the arc chamber. The remaining gas in the arc chamber is then quickly evacuated into a dump tank. The maximum run duration is about 100 ms. During the run total pressure

and temperature decrease due to mass and heat losses. Total conditions can be reached up to 500 bar total pressure and total enthalpies up to 20 MJ/kg without significant wind tunnel structure damage. A more detailed description is given by Francois et al. [1994].

C.2 Description of free piston driven shock tunnel HEG

A schematic view of the High Enthalpy facility in Göttingen is shown in Figure C.2. The piston driven shock tunnel consists of three main sections: the driver section, consisting of an air buffer and a compression tube, the shock tube and the nozzle/test section/dump tank.

The high pressure air buffer is used to accelerate the heavy piston into the compression tube. The compression tube is filled with the so-called driver gas, usually Helium or a Helium/Argon mixture to increase the ratio of speed of sound from driver to driven gas by lowering the molecular weight and therefore increase the required high incident Mach numbers. The piston compresses and heats the driver gas about 4000 K. When the desired pressure is reached, the primary diaphragm ruptures. This causes a strong shock wave propagating into the shock tube and reflects at the end of the shock tube, leaving a high temperature and pressure behind. In this region the reservoir in front of the nozzle is formed. When the desired pressure is reached there, the secondary diaphragm ruptures and the gas is expanded into the nozzle. The reservoir conditions can be maintained more or less constant for about 2-3 ms. The total pressure can reach 1000 bar and the total enthalpy up to 25 MJ/kg. A more detailed description is given by Eitelberg [1993].

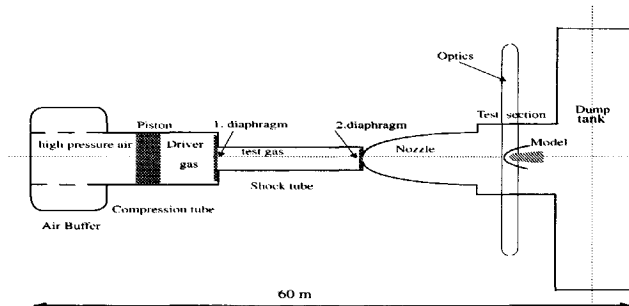


Figure C.2: Schematic view of the piston driven shock tunnel in Göttingen.

List of Symbols

A	Jacobian matrix $\frac{\partial E}{\partial w}$
$A_k^{c,s}$	curve fit constant for the determination of $c_{p,c,s}$
$A_k^{rot,s}$	curve fit constant for the determination of $c_{p,rot,s}$
A_k^s	curve fit constant for the determination of $c_{p,s}$
a	speed of sound, m/s
B	Jacobian matrix $\frac{\partial F}{\partial w}$
C	Jacobian matrix $\frac{\partial G}{\partial w}$
c	speed of light, $c = 2.99792 \cdot 10^{10}$ cm/s
c_{f_j}	constant in the Arrhenius equation of reaction j
$c_{p_{es}}$	specific heat with constant pressure of species s for the electronic enthalpy, J/kg-K
$c_{p_{rot,s}}$	specific heat with constant pressure of species s for the rotation enthalpy, J/kg-K
c_p_s	specific heat with constant pressure of species s , J/kg-K
$c_{p_v,s}$	specific heat with constant pressure of species s for the vibration enthalpy, J/kg-K
c_s	massfraction of species s
\tilde{c}_s	curve fit constant for the determination of σ_{es}
$c_{v,s}$	specific heat with constant volume of species s , J/kg-K
D_e	dissociation energy of molecule, cm ⁻¹
E	total energy per unit of mass, J/kg
e	electronic charge of a proton, $e = 1.6021892 \cdot 10^{-19}$ C
e^-	symbol for the electron
e_e	electrical energy per unit of mass, J/kg
e_{cs}	electrical energy per unit of mass of species s , J/kg
$e_{rot,s}$	rotation energy per unit of mass of species s , J/kg
e_s	energy per unit of mass of species s , J/kg
e_{trs}	translational energy per unit of mass of species s , J/kg
e_{vs}	vibrational energy per unit of mass of species s , J/kg

e_v	vibrational energy per unit of mass, J/kg
e_v	combined vibrational and electronic energy per unit of mass, J/kg
e_{0_s}	formation energy per unit of mass of species s , J/kg
$\vec{E}, \vec{F}, \vec{G}$	flux vector in direction x, y, z
g_i	degeneracy of quantum state i
H	Jacobian matrix of the thermo-chemical source terms $\frac{\partial \Omega}{\partial w}$
H	total enthalpy per unit of mass, J/kg
h	constant of Planck, $h = 6.626176 \cdot 10^{-34}$ Js
h_s	enthalpy per unit of mass of species s , J/kg
h_{e_s}	electronic enthalpy per unit of mass of species s , J/kg
h_{rot_s}	rotation enthalpy per unit of mass of species s , J/kg
h_{tr_s}	translational enthalpy per unit of mass of species s , J/kg
h_{v_s}	vibrational enthalpy per unit of mass of species s , J/kg
h_{0_s}	formation enthalpy per unit of mass of species s , J/kg
j	electronic quantum number
k_T	translational rotational conductivity, J/(m Ks)
k_{v_m}	vibrational conductivity of species m , J/(m Ks)
K	rotation quantum number
\hat{I}_s	ionization energy of species s , J/kmol
K_{eq_j}	equilibrium constant of reaction j in C.G.S units
k	constant of Boltzmann, $k = 1.380633 \cdot 10^{-23}$ J/K
k_{b_j}	backward reaction coefficient in C.G.S units
k_{f_j}	forward reaction coefficient in C.G.S units
M	Mach number
M_s	molar mass of species s , kg/kmol
m_e	mass of the electron, kg
N	constant of Avogadro, $N = 6.022045 \cdot 10^{26}$, 1/kmol
N_{sp}	total number of species used in the calculation
N_s	number density of species s , 1/m ³
\dot{n}_{e_s}	molar production of species s by electron impact ionization reaction, kmol/m ³ -s
$n_{f,r}$	exponent of the temperature in the Arrhenius equation of reaction r
P_{m-r}	probability in the vibration-vibration coupling
p	pressure, Pa
p_e	electron pressure, Pa
p_s	partial pressure of species s , Pa
p_t	total pressure, Pa
\vec{Q}	state vector of conservative variables $(\rho, \rho u, \rho v, \rho w, \rho e_{v_s}, \rho e_e, \rho e)$
Q	total partition function

Q_s^{el}	electronic partition function of species s
Q_s^{int}	internal partition function
Q_s^v	vibration partition function of species s
Q_{T-V}	translation - vibration coupling source term, J/m ³ -s
Q_{V-V}	vibration - vibration coupling source term, J/m ³ -s
Q_{V-E}	vibration - electron coupling source term, J/m ³ -s
Q_{T-E}	translation - electron coupling source term, J/m ³ -s
Q^{tr}	translation partition function
\mathcal{R}	universal gas constant, $\mathcal{R} = 8314.4 \text{ J/kmol}\cdot\text{K}$
Re_L	Reynolds number based on reference length L
Re_x	Reynolds number based on distance x
R_s	gas constant of species s , $R_s = \frac{\mathcal{R}}{M_s}$, J/kg·K
r_{eq}	distance between the atomic nuclei of a two atomic molecule in the potential minimum, m
s_s^0	entropy per unit of mass with 1 bar of species s , J/kg·K
T	translational-rotational temperature of the “heavy species”, K
T_e	electron translational, electronic excitation temperature, K
T_F	temperature, used in the Treanor-Marrone coupling, K
$T_{reac_b,j}$	reaction temperature of backward reaction j , K
$T_{reac_f,j}$	reaction temperature of forward reaction j , K
T_{ref}	reference temperature at which the $h_{0,s}$ is determined, $T_{ref} = 298.15 \text{ K}$
$T_{rot,s}$	rotational temperature of species s , K
T_v	vibrational temperature, K
$T_{v,s}$	vibrational temperature of species s , K
t	time, s
U	constant in the Treanor-Marrone coupling
u^k	speed in the k th direction, m/s
u_i	potential energy curve of the i^e excited state of a molecule, cm ⁻¹
u, v, w	speed in the x, y and z direction, m/s
V	volume, m ³
v	vibrational quantum number
w	primitive variables ($\rho, u, v, w, T, T_{v_s}, T_e$)
x, y, z	coordinates of a cartesian system, m

Greek letters

γ	ratio of the specific heats, $\gamma = c_p/c_v$
χ_s	concentration of species s , kmol/m ³
δ	small number
δ^*	displacement thickness of the boundary layer, m
ϵ_i	energy of quantum state i , J or cm ⁻¹ = $\frac{1}{\hbar c} = 1.9862 \cdot 10^{-23} J$

$\Theta_{i,s}$	characteristic temperature of the i^e excited state of species s , K
$\theta_{d,s}$	characteristic dissociation temperature of species s , K
θ_s	characteristic vibration temperature of species s , K
μ	dynamic viscosity of the mixture, $\frac{kg}{ms}$
μ_s	dynamic viscosity of species s , $\frac{kg}{ms}$
μ_{sr}	reduced mass of species s and r , kg/kmol
$\nu'_{s,j}$	stoichiometric coefficient for reactant s in reaction j
$\nu_{s,j}$	stoichiometric coefficient for product s in reaction j
ν_e	collision frequency of a molecule, 1/s
ν_{es}	effective collision frequency between species s and electrons, 1/s
ρ	density, kg/m ³
ρ_s	density of species s , kg/m ³
σ	symmetry factor in the degeneracies of the rotation quantum states.
σ_{es}	collision cross section of species s and electrons, m ²
σ_{sr}	collision cross section of species s and r in vibration - vibration coupling, m ²
σ_{xy}	shear stress: the first subscript x indicates the axis to which the face is perpendicular the second subscript y indicates the direction to which the shearing stress is parallel, [Pa]
τ_m	translational and vibrational (T-V) energy relaxation time for diatomic species m , s
τ_{es}	electronic and translational (E-V) energy relaxation time for diatomic species m , s
$\vec{\Omega}$	vector consisting of the chemical and relaxation source terms
ω_s	mass-production of species s by chemical reaction, kg/m ³ -s
ξ, η, ζ	coordinates of a local system

Subscripts

b	backward rate quantity
e	electronic mode; electrons
f	forward rate quantity
m	diatomic species m
s	species s

References

- Abgrall, R., J. Desideri, R. Glowinski, and M. Mallet (1991). *Workshop on Hypersonic Flows for Rentry Problems*. Springer-Verlag.
- Adams, J., W. Martindale, A. Mayne, and E. Marchand (1977, May). Real gas scale effects on shuttle orbiter laminar boundary layer parameters. *J. Spacecraft 14*(5).
- Akey, N. D. and A. Cross (1970). Radio blackout alleviation and plasma diagnostic results from a 25,000 foot per second blunt-body reentry. Technical Report TN D-5615, NASA.
- Anderson, J. (1989). *Hypersonic and High Temperature Gas Dynamics*. Mc Graw Hill.
- Balakrishnan, A. (1986, June). Correlations for specific heats of air species to 50.000 K. In AIAA. AIAA paper 86-1277.
- Barbato, M. and C. Bruno (1996). "Heterogeneous Catalysis: Theory, Models and Applications". In M. Capitelli (Ed.), *Molecular Physics and Hypersonic Flows*, NATO-ASI, pp. 139–160. Kluwer Publishers.
- Bertin, J. J. (1994). *Hypersonic Aerothermodynamics*. AIAA Publication Series.
- Blottner, F. G., M. Johnson, and M. Ellis (1971). Chemically reacting viscous flow program for multi-component gas mixture. Technical Report SC-RR-70-754, SANDIA.
- Bonnet, J., B. Chanetz, and D. Henry (1996, 2-6 May). Optical diagnostics for hypersonic flows. In *ICMAR International Conference on Methods of Aerophysical Research*, Novosibirsk, Russia.
- Born, M. and R. Oppenheimer (1927). Zur Quantentheorie der Moleküle. *Annalen der Physik 84*, 458–484.
- Boudreau, A. and J. Adams (1988, 18-20 May). Characterization of hypersonic wind tunnel flow fields. In *AIAA 15th Aerodynamic Testing Conference*, San Diego. AIAA paper 88-2006.
- Browne, W. G. (1962). Thermodynamic properties of some atoms and atomic ions. Technical Report Eng. Phys. Tech. Memo. #2 and #8, General Electric Co.
- Candler, G. (1988, June). *The Computation of Weakly Ionized Hypersonic Flows in Thermo-Chemical Nonequilibrium*. Ph. D. thesis, Stanford University.

- Capitelli, M., G. Colonna, C. Gorse, and D. Giordano (1994, December). Survey of methods of calculating high temperature thermodynamic properties of air species. Technical Report STR-236, ESA.
- Chanetz, B. (1995, February). Study of axisymmetric shock wave/boundary layer interaction in hypersonic laminar flow. Technical Report RT 42/4362, ONERA.
- Chanetz, B., M. Coet, d. Nicout, T. . Pot, and P. Broussard (1992, 4-7 May). Nouveaux moyens d'essais hypersonique developpes a l'ONERA: les souffleries R5 et F4. In *AGARD 70th FDP Meeting on Theoretical and Experimental Methods in Hypersonic Flows*, Turin, Italy. AGARD-CP-514.
- Chanetz, B., J. Delery, D. Nicoud, and C. Quelin (1990, June). La soufflerie hypersonique a faible nombre de Reynolds R5Ch. Technical Report RT 11/4362 AN, ONERA.
- Dadone, A. and B. Grossmann (1991). A rotated upwind scheme for the Euler equations. AIAA paper 91-0635.
- Deutschmann, O., U. Riedel, and J. Warnatz (1994, June 23). Modeling of nitrogen and oxygen recombination on partial catalytic surface. *ASME J. of Heat Transfer*.
- Devezzeau, D. and J. Tribot (1996, March). Synthesis of contributions to the hyperboloid-flare in F4 test case. In *ESA Manned Space Transportation Program, Proceedings of the Aerothermodynamics Workshop ESTEC*, Number YPA/2254/JM.
- Dunn, M. G. and S. W. Kang (1973). Theoretical and experimental studies of reentry plasma. Technical Report NASA CR 2232, NASA.
- Durand, G. (1992). Hyperboloid flare combination: a hypersonic test case for the qualification of compressible Navier-Stokes codes including high temperature effects. Technical Report DLA/ED/3A no 032.09.92, CNES.
- Edenfield, E. (1968,). Contoured nozzle design and evaluation for hotshot wind tunnels. In *AIAA paper 68-369*.
- Eitelberg, G. (1993, November). Calibration of the HEG and its use for verification of real gas in high enthalpy flows. In *AIAA 5th International Aerospace Planes and Hypersonic Technologies Conference*, Munich, Germany. AIAA paper 93-5170.
- Francois, G., A. Masson, and J. Ledy (1994). ONERA-F4 high enthalpy wind tunnel. In *82th Meeting of the Supersonic Tunnel Association (STA)*, Ohio, USA.
- Gnoffo, P., R. Gupta, and J. Shinn (1989). Conservation equations and physical models for hypersonic air flows in thermal and chemical nonequilibrium. Technical Report TP 2867, NASA.
- Gnoffo, P. A. (1989). Code calibration program in support of the aeroassist flight experiment. In *AIAA 24th Thermophysics Conference*. AIAA paper 89-1673.
- Godunov, S. (1959). A difference scheme for numerical computation of discontinuous solution of hydronamic equations. *Math. Sbornik* 47, 271-306. Translated US Joint Publ. Res. Service 7226 (1969).

- Goulard, R. (1958, November). On catalytic recombination rates in hypersonic stagnation heat transfer. *Jet Propulsion* 28(11), 737-745.
- Grasso, F. and M. Marini (1997, 12-14 November). Synthesis of T2-97 hollow cylinder flare problem. In *First Europe-US High Speed Flow Field Database Workshop Part II*, Naples, Italy.
- Griffith, B., J. Maus, and J. Best (1983). Explanation of the hypersonic longitudinal stability problem. In *Shuttle Performance: lessons learned*, NASA Langley Reserch Center. NASA-CP-2283.
- Gupta, R. N., N. Roop, Yos, and R. Thompson (1989). A review of reaction rates, thermodynamic and transport properties for 11 species air model. Technical Report NASA-TM-101528, NASA.
- Gurvich, L. V., I. V. Veyts, and C. B. Alcock (1989). *Thermodynamic Properties of Individual Substances*, Volume 1, part 2. New York: Hemisphere Publishing Corporation.
- Hakkinen, R., I. Greber, and L. Trilling (1959, 18 February). The interaction of an oblique shock wave with a laminar boundary layer. Technical Report NASA Memorandum 2-18-59W, Massachusetts Institute of Technology.
- Herzberg, G. (1950). *Spectra of Diatomic Molecules*, Volume 1, Molecular Spectra and Molecular Structure. New York: Van Nostrand Company, Inc.
- Hirsch, C. (1988). *Numerical Computation of Internal and External Flows*. John Wiley and Sons.
- Holden, M. (1978, January). A study of flow separation in regions of shock wave boundary layer interaction in hypersonic flow. In *AIAA 32nd Aerospace Sciences, Meeting & Exhibit*, Reno, NV. AIAA paper 78-1169.
- Hulbert, H. and J. Hirschfelder (1941). Potential energy functions for diatomic molecules. *Journal of Chemical Physics* 9, 61-69.
- Jaffe, R. (1987, June). The calculation of high-temperature equilibrium and nonequilibrium specific heat data for N_2 , O_2 and NO . In *AIAA 22nd Thermophysics Conference*, Honolulu, Hawaii. AIAA paper 87-1633.
- Jameson, A., W. Schmidt, and E. Turkel (1981). Numerical simulation of the Euler equations by finite volume methods using Runge-Kutta time stepping schemes. AIAA paper 81-1259.
- Jones, R. and J. Hunt (1969). Use of tetrafluoromethane to simulate real gas effects. Technical Report NASA TR -312, NASA.
- Jumper, E., M. Newman, D. Steward, and D. Kitchen (1993, January 11-14). Recombination of nitrogen on silica-based thermal-protection-tile-like surfaces. In *AIAA 31st Aerospace Sciences Meeting & Exhibit*, Reno, NV. AIAA paper 93-0477.
- Keating, G. (1996). *COSPAR International Reference Atmosphere (CIRA). Pt. 3. Trace constituent reference models*. Oxford, Pergamon.

- Kee, R. J., F. M. Rupley, and J. Miller (1987, April). The Chemkin Thermodynamic Data Base. Technical Report SAND87-8215, SANDIA.
- Kim, Y. (1988, September). Study of the recombination of nitrogen and oxygen on surface of materials used in space vehicles. Technical Report NCA2-158, Stanford University.
- Krek, R. M., S. Ueda, D. Kastell, and G. Eitelberg (1995, December). Electre experiments in the HEG facility. Technical Report DLR IB 223-95 A 65, DLR-Braunschweig.
- Kroll, N. and R. Radespiel (1993, December). An improved flux vector split scheme for viscous flows. Technical Report DLR-FB 93-53, DLR-Braunschweig.
- Landau, L. and E. Teller (1936). Zur theorie der schalldispersion. *Physicalisches Zeitschrift Sowiet Union* 10, 35–43.
- Lee, J. H. (1985a). Basic governing equations for the flight regimes of aeroassisted orbital transfer vehicles. In *Progress in Astronautics and Aeronautics*, Volume 96.
- Lee, J. H. (1985b). Electron impact vibrational excitation rates in the flow field of aeroassisted orbital transfer vehicles. In *AIAA 20th Thermophysics Conference*, Williamsburg, Virginia. AIAA paper 85-1035.
- Liou, M. and C. Steffen (1993). A new flux splitting scheme. *Journal of Computational Physics* 107(1), 23–39.
- Lochte-Holtgreven, W. (1968). *Plasma Diagnostics*. North-Holland Publishing company.
- MacCormack, R. (1969). The effect of viscosity in hypervelocity impact cratering. AIAA paper 69-354.
- Markelov, G., L. Walpot, and M. Ivanov (2001, June). Numerical simulation of laminar hypersonic separation using continuum and kinetic approaches. In *AIAA 35th Thermophysics Conference*, Anaheim, CA. AIAA paper 2001-2901.
- Marrone, P. V. and C. E. Treanor (1963, September). Chemical relaxation with preferential dissociation from excited vibrational levels. *The Physics of Fluids* 6(9), 1215–1221.
- Masson and Allemane (1995, February). Electre model test in F4 wind tunnel. Technical Report TR-PV 3/8908 GY, ONERA.
- Masurel, J., G. Jobard, and X. Bouis (1996, July). Heat flux study and pressure measurements on ARD and Soyuz vehicles in perfect gas conditions in the S4MA wind tunnel. Technical Report PV 4/8015 GY 400 G, ONERA.
- Mazoue, F., L. Walpot, M. Netterfield, and L. Marraffa (1996, June). Development and validation of nonequilibrium condensing flow solvers. In *AIAA 12th Applied Aerodynamics Conference*, Colorado Springs, USA. AIAA paper 96-1893.
- (1976). *US Standard Atmosphere, National Oceanic and Atmospheric Administration, Publication NOAA-S/T76-1562*. New York: American Institute of Physics.
- Millikan, R. C. and D. R. White (1963, 15 December). Systematics of vibrational relaxation. *Journal of Chemical Physics* 39(12), 3209–3213.

- Molina, R., G. Simeonides, and L. Walpot (1996, June 20-23). Pre-flight aerothermodynamic analysis of the atmospheric reentry demonstrator. In *14th AIAA Applied Aerodynamics Conference*. AIAA paper 96-2468.
- Moretti, G. and M. Abbet (1966). A time-dependent computational method for blunt-body flows. *AIAA Journal* 4(12), 2136–2141.
- Muylaert, J. and L. Walpot (1993, October). Numerical simulations of hyperboloid-flare in high enthalpy wind tunnels and in flight conditions. In *2nd IMACS Conference on Computational Physics, St Louis, USA*.
- Muylaert, J., L. Walpot, and G. Durand (1993, 6-9 July). Computational analysis on generic forms in European hypersonic facilities: standard model Electre and hyperboloid-flare. In *19th International Symposium on Shock Waves (ISSW19)*, Marseille.
- Muylaert, J., L. Walpot, J. Häuser, P. Sagnier, D. Devezau, O. Papernyk, and D. Lourme (1992, 6-9 July). Standard model testing in the European high enthalpy facility F4 and extrapolation to flight. In *AIAA 17th Aerospace Ground testing Conference*, Nashville, TN. AIAA 92-3905.
- Muylaert, J., L. Walpot, N. Hironde, G. Tumino, G. Simeonides, G. Koppenwallner, and J. Davis (1995, 23-28 July). Computational analysis of experiments in T5 and HHK for the study of the flap-induced separation on an axisymmetric configuration. In *20th International Symposium on Shock Waves (ISSW20)*, Caltech, Pasadena.
- Muylaert, J., L. Walpot, and M. Spel (1996, June 20-23). Non-equilibrium computational analysis of blunt-cone experiments performed in the LENS and HEG facilities. In *14th AIAA Applied Aerodynamics Conference*. AIAA paper 96-2436.
- Muylaert, J., L. Walpot, M. Spel, P. Sagnier, K. Hannemann, and H. Olivier (1998, June 14-18). Review of European code validation studies in high enthalpy flow. In *AIAA Advanced Measurement and Ground Testing Technology Conference*. AIAA paper 98-2769.
- Muylaert, J., L. Walpot, R. Steijl, and M. Spel (1997). Blunt cone near wake analysis in F4 and Lens. In *21th International Symposium on Shock Waves (ISSW21)*. paper 6555, Queensland, Australia.
- Osher, S. (1982). Shock modeling in aeronautics. *Numerical methods for Fluid Dynamics*, 179–218.
- Osher, S. and S. Chakravarthy (1984). Efficient implementation of essentially non-oscillatory shock capturing schemes. *SIAM Journal of Numerical Analysis* 21, 955.
- Papirnyk and Bohl (1992, March). Utilization of a standard model in the hypersonic wind tunnels within the Hermes programme. Technical Report RT 48/6122 AY, ONERA.
- Park, C. (1987, June). Assessment of two-temperature kinetic model for ionizing air. In *AIAA 22nd Thermophysics Conference*, Honolulu, Hawaii. AIAA paper 87-1574.

- Park, C. (1990). *Nonequilibrium Hypersonic Aerothermodynamics*. Wiley Interscience.
- Park, C. (1993, July-Sept). Review of chemical kinetic problems of future NASA missions, I: Earth entries. *Journal of Thermophysics and Heat Transfer* 7(3), 385–398.
- Park, C. and S.-H. Lee (1993, July). Validation of multi-temperature nozzle flow code NOZNT. In *AIAA 28nd Thermophysics Conference*, Orlando, Fl. AIAA paper 93-2862.
- Park, C. and S. Yoon (1989). Calculation of real gas effects on blunt body trim angles. AIAA paper 89-0685.
- Pauling, L. and E. Wilson (1985). *Introduction to Quantum Mechanics*. Dover Publication.
- Petschek, H. and S. Byron (1957). Approach to equilibrium ionization behind strong shock waves in argon. *Annals of Physics* 1, 270–315.
- Rhudy, R. and G. Merz (1965, September). Heat transfer and pressure distribution on a scale model SV-5D at Mach 10. Technical report, AEDC. AEDC-TR-194.
- Roe, P. (1983). Approximate Riemann solvers, parameters vectors and difference schemes. In *Journal of Computational Physics*, Volume 43, pp. 357–372.
- Sagnier, P. (1992, March). Usefulness of Electre flight experiment within the Hermes Programme. Technical Report RT 38/6121 SY (H-NT-0-2047-ONER), ONERA.
- Sagnier, P. (1995, March). Summary of computations on the Electre standard model in the frame of the test campaigns in ONERA wind tunnels F4, R3CH, S4MA. Technical Report RT 6/8908 GY, ONERA.
- Schexnayder, C. J., J. S. Evans, and P. Huber (1970). Comparison of theoretical and experimental electron density for RAM C flights. Technical Report SP-252, NASA.
- Schwane, R. and D. Hänel (1987). Computation of viscous supersonic flow around blunt bodies. In *7th GAMM Conference on Numerical Math. in Fluid Mechanics*, Louvain la Neuve, Be. AIAA paper 87-1105CP.
- Schwane, R. and J. Muylaert (1992, June). Design of the validation experiment: Hyperboloid-flare. Technical Report Document: YPA/1256/RS, ESA-ESTEC.
- Scott, C. (1987, December 7-11). The effects of thermochemistry, non-equilibrium and surface catalysis in the design of hypersonic vehicles. *First Joint Europe-US Short Course on Hypersonics*.
- Screen, E. and H. Nickel (1965, February). Hypersonic heat transfer test results from a 9.688% model SV-5D vehicle for program 680a in the Martin hypersonic tunnel second series. Technical report. ER-13686.
- Seibert, G., J. van Kuren, and J. Heath (1992). Optical measurements techniques for hypervelocity flows. In *AIAA Professional Studies Series Notes*.
- Shu, C. and S. Osher (1988). Efficient implementation of essentially non-oscillatory shock capturing schemes. *Journal of Computational Physics* 77, 439–471.

- Simeonides, G. (1995, August). Simple formulations for convective heat transfer prediction over generic aerodynamic configurations and scaling of radiation-equilibrium. Technical Report EWP-1860, ESA/ESTEC.
- Simeonides, G., L. Walpot, M. Netterfield, G. Tumino, and J. Muylaert (1996, June). Evaluation of engineering heat transfer prediction methods in high enthalpy flow conditions. In *AIAA 31th Thermophysics Conference*, New Orleans, USA. AIAA paper 96-1860.
- Simeonides, G., L. Walpot, M. Netterfield, G. Tumino, and J. Muylaert (1998, January-February). Evaluation of engineering heat transfer prediction methods in high enthalpy flow conditions. *AIAA Journal of Spacecraft and Rockets* 35.
- Steele, D., E. Lippincott, and J. Vanderslice (1962). Comparative study of empirical inter-nuclear potential functions. *Reviews of modern Physics* 34(2), 239–251.
- Steger, J. and R. Warming (1981). Flux vector splitting of the inviscid gas-dynamic equations with applications to finite difference methods. In *Journal of Computational Physics*, Volume 40, 263-93.
- Steijl, R., L. Walpot, and P. Bakker (1997, November). Hypersonic facility F4: test case T10-97. In *First Europe-US High Speed flow field Database Workshop*.
- Stewart, D., Y. Chen, and W. Henline (1991, June 24-26). Effect of nonequilibrium flow chemistry and surface catalysis on surface heating to afe. Honolulu, Hawai. AIAA paper 91-1373.
- Sutton, G. and A. Sherman (1965). *Engineering Magnetohydrodynamics*. Mc Graw Hill.
- Taylor, R., M. Camac, and M. Feinberg (1967). Measurements of vibration-vibration coupling in gas mixtures. In *Proceedings of the 11th International Symposium on combustion , Pittsburgh, PA*, pp. 49–65.
- Treanor, C. E. and P. V. Marrone (1962, September). Effect of dissociation on the rate of vibrational relaxation. *The Physics of Fluids* 5(9), 1022–1026.
- Van Albada, G. D., B. van Leer, and W. Roberts (1982). A comparative study of computational methods in cosmic gas dynamics. *Astron. Astrophys.* 108:76-84.
- Van Leer, B. (1983, April). Computational methods for ideal compressible flow. In *Lecture notes 1983-04, Von Karman Institute, Belgium*.
- Verant, J.-L. (1994, May). Numerical enthalpy rebuilding for perfect gas and nonequilibrium flows – application to high enthalpy wind tunnels. Technical Report RT 69/ 6121/SY, ONERA.
- Verant, J.-L. and L. Walpot (2001, October). Analysis of finite rate catalysis on heating levels on the nose area of X-38 vehicle step 2 studies. Technical Report RT 104/6121/Y/DEFA, ONERA.
- Vincenti, W. G. and C. H. Kruger (1965). *Introduction to Physical Gas Dynamics*. Robert E. Krieger Publishing Company.

- Wada, Y. and M.-S. Liou (1994, January 10-13). A flux splitting scheme with high-resolution and robustness for discontinuities. In *AIAA 32nd Aerospace Sciences Meeting & Exhibit*, Reno, NV. AIAA paper 94-0083.
- Walpot, L. (1991, August). Quasi one-dimensional inviscid nozzle flow in vibrational and chemical nonequilibrium, diploma thesis. Technical Report EWP-1664.
- Walpot, L. (1997, November). Blunt cone in LENS: test case T12-97. In *First Europe-US High Speed flow field Database Workshop*.
- Walpot, L. (2000, September). Grid convergence studies on laminar shock wave boundary layer interaction. In *European Congress on Computational Methods in Applied Sciences and Engineering*, Barcelona, Spain.
- Walpot, L., P. Adam, and J. Muylaert (1993, January). Numerical simulation of Electre and hyperboloid flare in high enthalpy facility F4 and extrapolation to flight. Technical Report Document: YPA/1704/LW, ESA-ESTEC.
- Walpot, L. and P. Bakker (1997). Development and validation of a three-dimensional thermo-chemical nonequilibrium Navier-Stokes solver. Technical Report Memorandum-815, T.U. Delft.
- Walpot, L., W. Bannink, and P. Bakker (1996). Review of local inclination methods in hypersonics and applications. Technical Report Memorandum-737, T.U. Delft.
- Walpot, L. and G. Eitelberg (1994, November). Synthesis of the shock-shock interaction on a wedge cylinder configuration. In *EHVDB Workshop ESTEC*, Noordwijk, The Netherlands.
- Walpot, L. and W. Kordulla (1996, October). Synthesis of flow simulation for test case 2.b, Electre model in the hypersonic impulse facility HEG. In *Workshop ESTEC in The Netherlands*, Göttingen. DLR-IB 223-96 A 57.
- Walpot, L. and J. Muylaert (1994, November). Standard model electre in European hypersonic facility F4. In *EHVDB Workshop ESTEC*, Noordwijk, The Netherlands.
- Walpot, L., J. Muylaert, and P. Bakker (1995). High enthalpy nozzle flow sensitivity study and its influence on stagnation heat fluxes. In *20th International Symposium on Shock Waves (ISSW20)*. Caltech, California, USA.
- Walpot, L., R. Steijl, P. Bakker, and L. Marraffa (1997). Development and validation of a two-dimensional nonequilibrium condensing flow solver. In *21th International Symposium on Shock Waves (ISSW21)*. paper 6552, Queensland, Australia.
- Walpot, L. and R. Schwane (1994, June). Validation of high resolution schemes in flows with viscous and inviscid interaction and nonequilibrium. In *AIAA 12th Applied Aerodynamics Conference*, Colorado Springs, USA. AIAA paper 94-1904.
- Walpot, L., G. Simeonides, J. Muylaert, and P. Bakker (1996, October). High enthalpy nozzle flow sensitivity study and its influence on stagnation heat fluxes. *Shock-Waves, Springer Verlag* 6(4).

- Wegener, P. (1997). *The Peenemünde wind tunnels*. Yale University Press.
- Weilmuenster, K., A. Gnoffo, and A. Greere (1993, 6-9 July). Navier-Stokes simulations of the shuttle orbiter aerodynamic characteristics with emphasis on pitch trim and body flap. In *AIAA 28th Thermophysics Conference*, Orlando, FL.
- Wilke, C. (1950, April). A viscosity equation for gas mixtures. In *Journal of Chemical Physics*, Volume 18, pp. 517-519.
- W.L. Jones, J. and A. Cross (1972). Electrostatic probe measurements of plasma parameters for two reentry flight experiments, at 25,000 feet per second. Technical Report TN D-6617, NASA.
- Yos, J. (1963). Transport properties of nitrogen, hydrogen, oxygen, and air to 30,000 K. Technical Report Technical Memorandum RAD/TM/63-7, AVCO.

Development and Application of a Hypersonic Flow Solver

Summary

Numerical simulations are of crucial importance to bridge the gap between wind tunnel experiments and free flight conditions, because it is possible to simulate in a wind tunnel only certain aspects of the hypersonic flow regime around an earth re-entering vehicle. In addition numerical simulations provide a better understanding of the facility performance and they support the interpretation of experimentally measured data. A reliable extrapolation to free flight conditions of a space vehicle can be achieved only by a well validated CFD tool and well understood experimental data. Therefore a hypersonic flow solver has been developed. This thesis concerns the selection, implementation, verification and validation of the hypersonic flow solver. The test cases considered range from academic test problems of modest complexity to full scale applications of industrial interest.

The governing equations describing nonequilibrium chemically reacting air mixtures are summarized and put in a mathematical framework amenable to a finite volume discretization. The AUSM scheme is selected from among other flux difference schemes as a compromise between accuracy and efficiency. The validity of the choice of this flux difference splitting scheme is corroborated through the application to three test cases ranging from subsonic to hypersonic flows in simple geometries. The linearized equations are solved fully implicit using a line Gauss-Seidel method.

The verification and validation of the code in hypersonic flows is conducted. All the test cases are chosen to eliminate uncertainties arising from the modeling of turbulence. This assumption is demonstrated to be valid for all cases considered herein. The three test cases considered include a flow with no chemical and thermal phenomena, a flow which increasingly important thermal excitation and a flow with dominant vibrational excitation, dissociation and ionization. It is shown that the code is capable to produce grid-converged solutions which are within the respective experimental test accuracy.

The sensitivity of the code with respect to the various physical models which describe high temperature gas flows is addressed. In order to determine which physical model best represents the phenomena actually observed in experiments, two state-of-the-art European hypersonic wind tunnels, F4 and HEG, are studied. Quasi one-dimensional and axisymmetric

Navier-Stokes nozzle flow computations are shown to provide an efficient means for the performance of parametric sensitivity studies. Examination of various thermo-chemical nonequilibrium models shows that the most important differences are found between reaction rate models. At present, in moderate high pressure, high enthalpy wind tunnels (in contrast to low pressure, high enthalpy materials testing facilities) the variables static pressure, temperature and Mach number are identified as the most sensitive to thermo-chemical behavior. Conversely, density, velocity and Pitot pressure are found to be rather insensitive to thermo-chemical effects. High density real gas effects are shown to be irrelevant at the current levels of operating pressure in high enthalpy facilities. The sensitivity study performed reveals that current measurement techniques have not reached the adequate maturity to draw more definitive conclusions. Reduction of flow contamination and non-intrusive flow field measurements are expected to provide further insight into this matter.

The extrapolation to flight is addressed for two re-entry vehicles, namely the ARD capsule and the X-38 CRV demonstrator. The "real gas" effects are successfully simulated for the ARD, in terms of predicting the shift in trim angle in flight compared to the cold wind tunnel tests. For the X-38 demonstrator, when extrapolating to flight, the Mach number, viscous and "real gas" effects on the pitching moment are demonstrated. Although this vehicle has not flown yet, the trend on the pitching moment increment is also confirmed by comparing Shuttle flight data with "cold" hypersonic wind tunnel data. It is shown for the X-38 that CF4 wind tunnel tests are useful for trends simulating "real gas" effects, but fail to predict the complete pitching moment increment compared to flight due to the different behavior in expansion regions.

Also we have shown the importance of the assumption of surface catalysis of the material. A maximum difference of 60% in heat flux at the stagnation point has been obtained between fully catalytic and non-catalytic wall properties. Since heat fluxes are essential in setting the trajectory constraints, more effort has to be put into the characterization of catalytic and radiative properties of the materials.

Because the tool has been carefully validated it becomes a valuable tool for design of wind tunnel/flight models and generation of aerothermodynamic characteristics for re-entry vehicles.

Ontwikkeling en toepassing van een hypersone flow solver

Samenvatting

Numerieke simulaties zijn van cruciaal belang om het verschil te verklaren tussen windtunnelresultaten en resultaten verkregen door metingen tijdens de “echte” vlucht. Het is gebleken dat het nauwelijks mogelijk is om de stroming rond het voertuig tijdens de vlucht na te bootsen in hypersone windtunnels. Om deze stroming toch te kunnen bestuderen is het nodig om een goed gevalideerde numerieke code te hebben die, met behulp van windtunnelmetingen, een betrouwbare extrapolatie kan bieden naar de vluchtcondities. Bovendien kunnen numerieke simulaties bijdragen tot een verbeterd inzicht en interpretatie van wat er gebeurt in experimentele testfaciliteiten. Om deze redenen is een nieuwe hypersone code ontwikkeld. Dit proefschrift omvat het selecteren van numerieke en fysische modellen, het implementeren, het verifiëren en valideren van deze nieuw ontwikkelde code. De beschouwde testgevallen variëren van academische testproblemen tot toepassingen van re-entry voertuigen op ware grote met industriële belangen.

De stromingsvergelijkingen van thermisch en chemisch reagerende gasmengsels die niet in evenwicht zijn, zijn in een wiskundige vorm opgeschreven zodat ze gebruikt kunnen worden voor een eindige volume methode. Het AUSM schema is geselecteerd ten koste van andere “flux difference” schema’s als een compromis tussen nauwkeurigheid en efficiëntie. Deze keuze wordt bevestigd door de toepassing op drie testgevallen variërend van subsone tot hypersone stromingen op academische geometriën. De gelineariseerde vergelijkingen zijn opgelost met een volledig impliciet schema gebruikmakend van de Gauss-Seidel methode.

De verificatie en validatie van de code is uitgevoerd door de code toe te passen op drie hypersone stromingsproblemen. De drie testgevallen zijn zodanig gekozen dat de onzekerheden van de turbulentiemodelleringen uitgesloten worden. Het eerste testgeval behelst een stroming waarin geen thermo-chemische processen aanwezig zijn, het tweede een stroming waarin de thermische excitatie belangrijker wordt en het derde een stroming waarin vibratie excitatie, dissociatie en ionisatie domineren. Er is aangetoond dat de code in staat is om grid geconvergeerde oplossingen te produceren die binnen de meetnauwkeurigheid van de experimenten vallen.

De gevoeligheid van de code, met betrekking tot de verschillende fysische modellen waarin

de hoge temperatuureffecten worden beschreven, wordt besproken. Om te bepalen welke fysische modellen de waargenomen fenomenen in windtunnels het beste beschrijven, worden twee Europese hypersone windtunnels bestudeerd: F4(ONERA) and HEG(DLR). Quasi één-dimensionale Euler stromingen met grenslaagcorrecties en axiaalsymmetrisch viskeuze stromingen door een kanaal zijn gesimuleerd om een efficiënt middel te verkrijgen voor parametrische sensitiviteitsanalyse. Deze analyse toegepast op verschillende thermo-chemische stromingen heeft aangetoond dat de grootste verschillen worden veroorzaakt door het gebruik van verschillende chemische reactiemodellen. Experimenten in hoge druk- en hoge enthalpiewindtunnels hebben aangetoond dat druk, temperatuur en het getal van Mach een grote gevoeligheid hebben ten aanzien van thermo-chemisch gedrag in de stroming. De dichtheid, de snelheid en de Pitot-druk daarentegen, zijn hiervoor ongevoelig. Het modelleren van reële gassen is niet belangrijk gebleken in het gebied waarin de huidige windtunnels opereren. Ook is gebleken dat verdere ontwikkeling van de meettechnieken nodig is om verdere conclusies te kunnen trekken.

De extrapolatie naar de vluchtcondities is gemaakt voor twee verschillende re-entry voertuigen, namelijk de ARD capsule en het X-38 CRV testvoertuig. Hoge temperatuureffecten zijn succesvol gesimuleerd voor de ARD ten aanzien van de voorspellen van de verschuiving van de trimhoek in de vlucht ten opzichte van experimentele windtunnelmetingen met koud gas.

Ten aanzien van het X-38 testvoertuig zijn effecten van het Mach getal, de viscositeit en de hoge temperatuur op de "pitch" momenten beschreven. Deze effecten zijn ook waargenomen voor de Space Shuttle. Er is aangetoond voor de X-38 dat de CF4 windtunnel het "pitch-up" moment tengevolge van hoge temperatuureffecten in vrije vlucht niet volledig kan simuleren omdat CF4 zich in expansiezones niet overeenkomstig gedraagt.

Voor het voorspellen van het warmtetransport door de wand is de katalyciteit van het materiaal belangrijk. Een verschil van maximaal 60% in het stagnatiepunt is gevonden tussen een volledig katalytische wand en een niet-katalytische wand. Omdat het warmtetransport cruciaal is voor het materiaal, zal meer aandacht moeten geschonken worden aan de katalyciteit en stralingseigenschappen van verschillende materialen.

De ontwikkelde code is zorgvuldig gevalideerd en kan daarom een waardevolle bijdrage leveren aan het ontwerpen van nieuwe voertuigen voor het genereren van de aerothermodynamische karakteristieken of het ontwerpen van windtunneltesten.

Acknowledgments

The research presented in this thesis has been possible due to the technical and/or moral support of numerous people.

First of all I would like to thank my promotor Prof.dr.ir. P.G. Bakker and Marc Gerritsma for their enthusiastic guidance, support and advice in this work. Also I would like to express my gratitude to ir. W.J. Bannink for his contributions.

I would like to thank the TOS-MPA team of ESTEC under the leadership of Jean Muylaert and before Prof.dr. J. Häuser for the opportunity to work on an European level and introducing me to the exciting topics of hypersonic flow research.

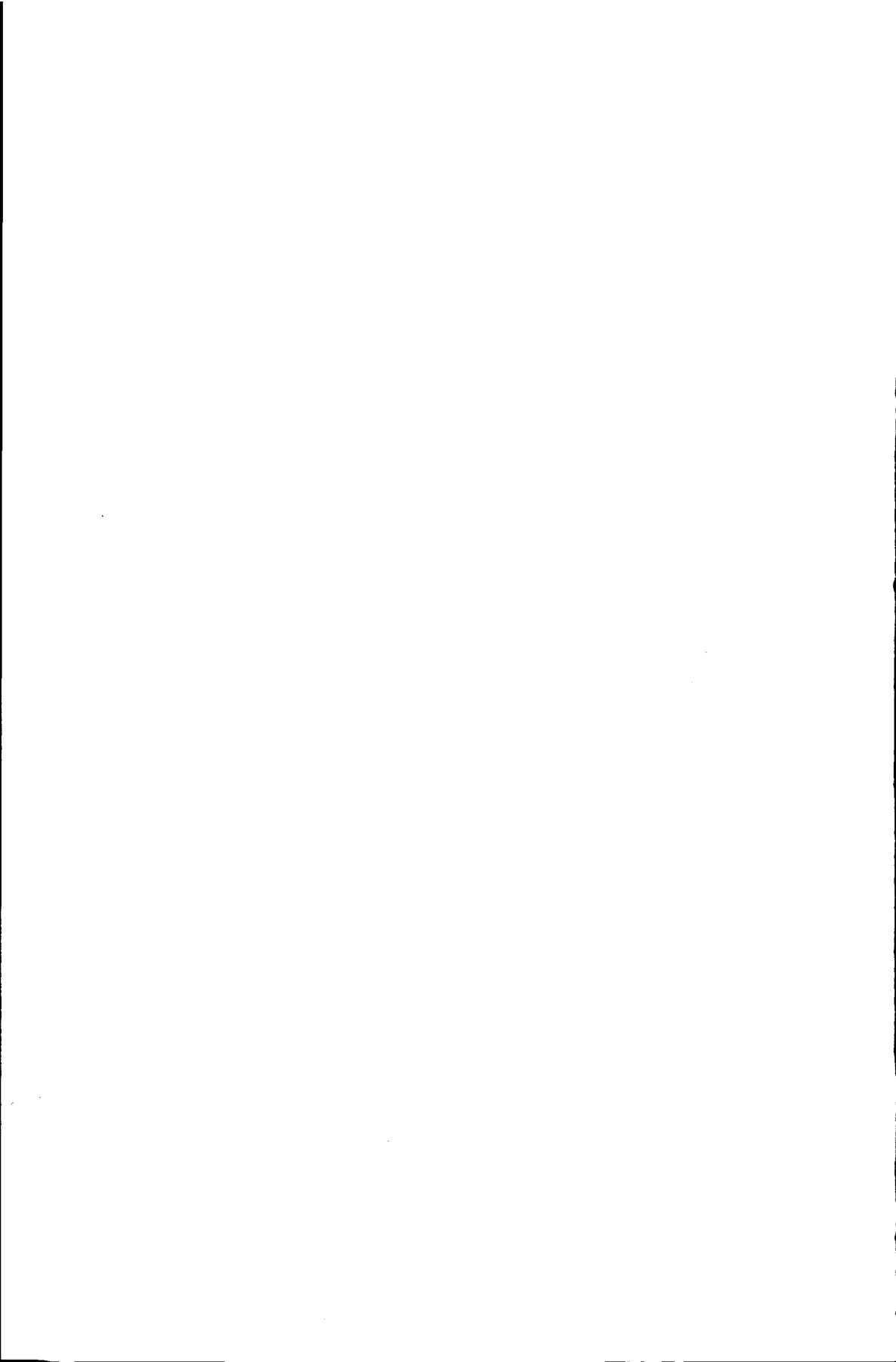
I am also gratefully indebted to Rafael Molina of the ARD and X38-CRV project for his enlightenment in many discussions and the solid support. I would like to express my gratitude to the X-38 and ARD team in which I worked several years and for the friendly relationship and professional communicationship developed over the years: Jose Longo, Jean-Pierre Tribot, Mike Steinkopf, Eckart Graf and Marco Caporicci.

I owe Martin Spel in many ways and in particular for his never defecting support. Also it was always a source of renewed amazement to receive the precious advice of Maurizio Barbato, George Simeonides and Henry Wong.

I would like to thank the HEG (DLR) team, the F4 (ONERA) team and the CIRA team for the fruitful discussions we had, especially Wilhelm Kordulla, Klaus Hanneman, George Eitelberg, Dominique Devezeau, Philippe Sagnier, Jean-Luc Verant and Marco Marini.

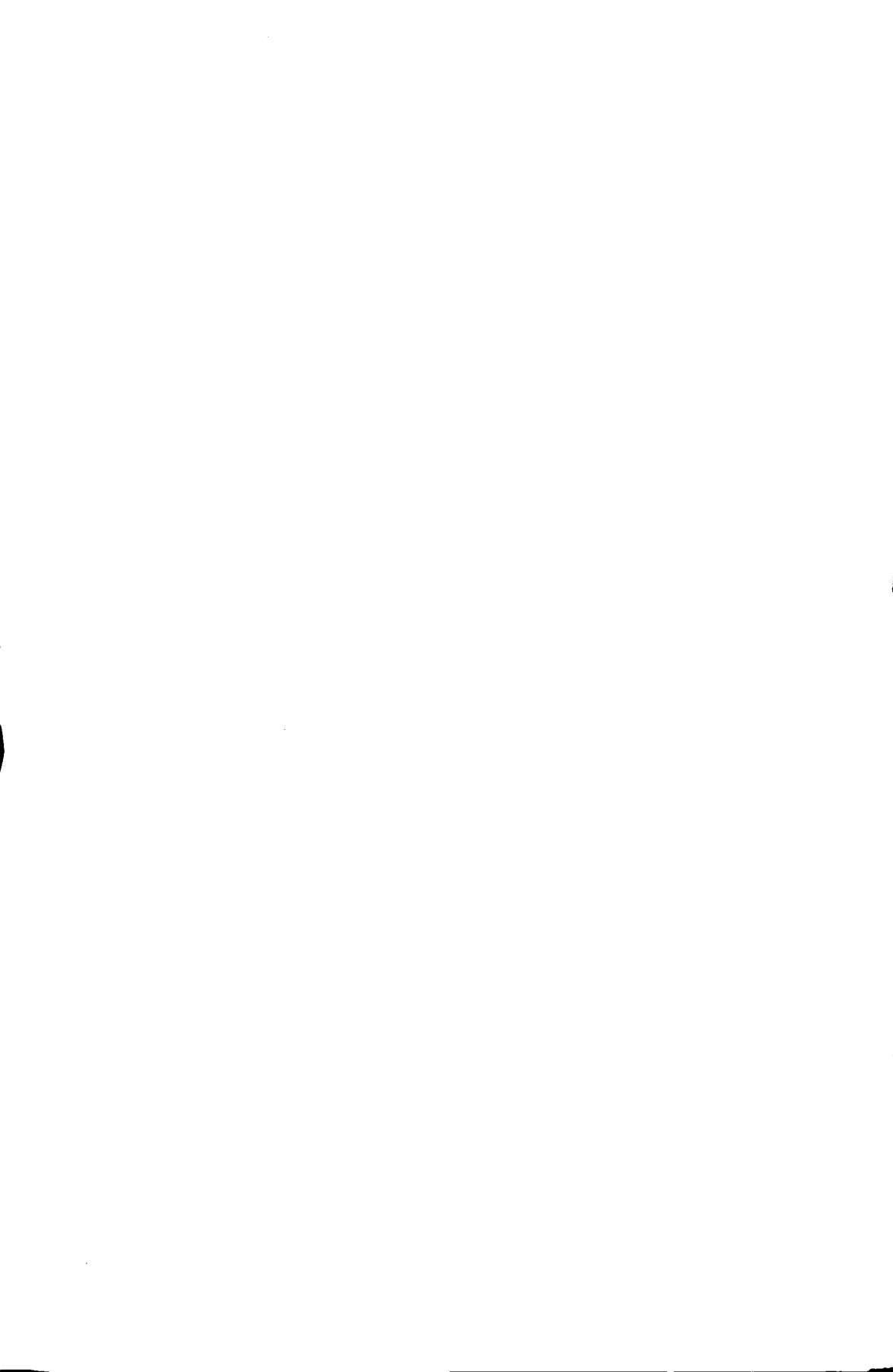
I would like to thank my co-workers at Atos Origin Engineering Services B.V. and its director Paul Pearson for the support of this thesis.

Finally, I would like to thank my mother for her support. Also thanks to Christel for her patience and understanding for the long evenings and weekends taken to complete this thesis.



Sponsored by Atos Origin Engineering Services B.V.





TR 3861 - S

Stellingen behorende bij het proefschrift

Ontwikkeling van een numerieke code toegepast op hypersone stromingen

L. Walpot

- De experimentele data van hypersone windtunnels en vluchttesten zijn voldoende om globale parameters te valideren met CFD, maar zijn niet nauwkeurig genoeg om de onderliggende modellen te valideren. (zie hoofdstuk 4)
- Ondanks de grote verschillen in de literatuur in chemische reactiesnelheden en warmtecoëfficiënten bij hoge temperaturen geven de resultaten toch een goed kwalitatief en kwantitatief beeld van de stroming nodig voor analyse van de in deze thesis beschouwde "re-entry" voertuigen. (zie hoofdstuk 5)
- Validatie van een hypersone code kan, gezien de complexiteit van de verschillende fenomenen, alleen aangetoond worden door een grote diversiteit van problemen te vergelijken met experimentele gegevens.
- Een goede stelling voldoet aan vijf voorwaarden: je kunt de vijand zien, je leeft ongezien, je kunt vuren, je bent beschermd en je kunt de stelling verlaten.
- Regels en wetten worden uitgehouden op het moment dat ze worden toegepast.
- Netwerken rendeert veel meer dan technische kennis voor een goede carrière naar het top management.
- Achter grote mannen staan sterke vrouwen; achter grote vrouwen staan onbeduidende mannen.
- In deze wereld zijn pessimisten de gelukkigste mensen want ze worden zelden in hun verwachtingen teleurgesteld.
- Kwaliteitszorg is de illusie verkopen dat de klant erop vooruit gaat.





